Max-Planck-Institut
für Meteorologie

MAX-PLANCK-GESELLSCHAFT

International Max Planck Research School
on Earth System Modelling

# The influence of misrepresenting the nocturnal boundary layer on daytime convection in large-eddy simulation

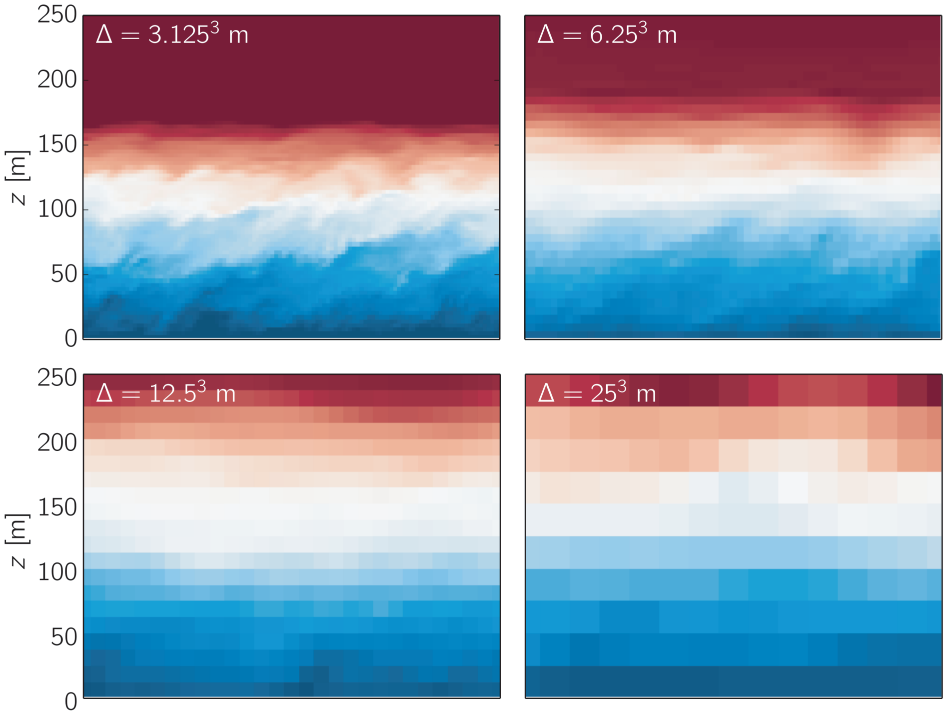

Bartholomeus Jacobus Henricus van Stratum

Hamburg 2017

Berichte zur Erdsystemforschung
*Reports on Earth System Science*

187
2017

## Hinweis

Die Berichte zur Erdsystemforschung werden vom Max-Planck-Institut für Meteorologie in Hamburg in unregelmäßiger Abfolge herausgegeben.

Sie enthalten wissenschaftliche und technische Beiträge, inklusive Dissertationen.

Die Beiträge geben nicht notwendigerweise die Auffassung des Instituts wieder.

Die "Berichte zur Erdsystemforschung" führen die vorherigen Reihen "Reports" und "Examensarbeiten" weiter.

## Notice

The Reports on Earth System Science are published by the Max Planck Institute for Meteorology in Hamburg. They appear in irregular intervals.

They contain scientific and technical contributions, including Ph. D. theses.

The Reports do not necessarily reflect the opinion of the Institute.

The "Reports on Earth System Science" continue the former "Reports" and "Examensarbeiten" of the Max Planck Institute.

## Anschrift / Address

Max-Planck-Institut für Meteorologie
Bundesstrasse 53
20146 Hamburg
Deutschland

Tel./Phone: +49 (0)40 4 11 73 - 0
Fax: +49 (0)40 4 11 73 - 298

name.surname@mpimet.mpg.de
www.mpimet.mpg.de

## Layout

Bettina Diallo and Norbert P. Noreiks
Communication

## Copyright

Photos below: ©MPI-M
Photos on the back from left to right:
Christian Klepp, Jochem Marotzke,
Christian Klepp, Clotilde Dubois,
Christian Klepp, Katsumasa Tanaka

# The influence of misrepresenting the nocturnal boundary layer on daytime convection in large-eddy simulation

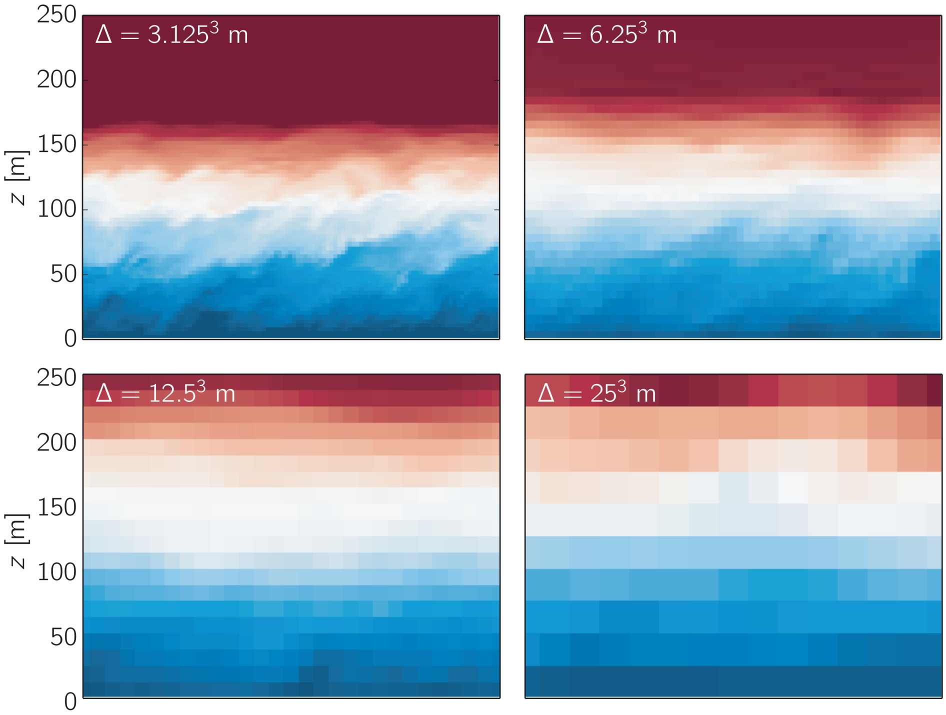

Dissertation with the aim of achieving a doctoral degree
at the Faculty of Mathematics, Informatics and Natural Sciences
Department of Earth Sciences of Universität Hamburg
submitted by

## Bartholomeus Jacobus Henricus van Stratum

Hamburg 2017

Bartholomeus Jacobus Henricus van Stratum

Max-Planck-Institut für Meteorologie
Bundesstrasse 53
20146 Hamburg

Tag der Disputation: 15.7.2016

Folgende Gutachter empfehlen die Annahme der Dissertation:

Prof. Dr. Felix Ament
Prof. Dr. Bjorn Stevens

Berichte zur Erdsystemforschung / Max-Planck-Institut für Meteorologie 187
*Reports on Earth System Science / Max Planck Institute for Meteorology* 2017

ISSN 1614-1199

## Abstract

Large-eddy simulation (LES) has been used extensively to study turbulence related atmospheric processes, traditionally focussed on (highly) idealized studies, with the domain size and resolution optimized for the process of interest. More recently the use of LES has moved towards more realistic experiments, for example by performing realistic weather hindcasts on domains as large as Germany (~ 1000 km). In contrast to more idealized LES experiments, such a setup requires both a sufficiently fine computational mesh to resolve the smallest turbulent scales – like shear driven turbulence in the stable boundary layer (SBL) – and a sufficiently large domain to capture the largest turbulent scales – like deep convective systems. As we are decades away from being able to perform such experiments, some simplifications are required. Often a resolution is used which is sufficient to resolve the daytime boundary layer, but insufficient to resolve turbulence at night, which (in theory) makes part of the LES experiments invalid. This thesis addresses a number of questions about the use of such an LES setup: How poorly is the atmosphere (SBL) represented when using a resolution insufficient to resolve turbulence? And does a poorly resolved SBL have the potential to influence the following day of convection?

# Zusammenfassung

Zur Untersuchung turbulenter, atmosphärischer Prozesse werden oftmals Grobstruktursimulationen (LES) genutzt, deren Schwerpunkt traditionell auf (stark) idealisierten Studien liegt, in denen das Modellgebiet und die Modellauflösung entsprechend des untersuchten Prozesses optimiert werden. In jüngster Zeit verschiebt sich dieser Schwerpunkt in Richtung realistischer Experimente, wie z.B. bei der Berechnung einer nachträglichen Wettervorhersage in einem Modellgebiet der Größe Deutschlands (∼1000 km). Im Gegensatz zu stark idealisierten LES-Experimenten benötigt eine solche realistische Simulation sowohl ein ausreichend feine Modellauflösung, um die kleinsten turbulenten Skalen – wie z.B. durch Scherung verursachte Turbulenz in einer stabilen Grenzschicht – aufzulösen, als auch ein ausreichend großes Modellgebiet, um die größten turbulenten Skalen – wie z.B. hochreichende, konvektive Systeme – zu erfassen. Da wir noch Jahrzehnte davon entfernt sind solch umfangreiche Modellsimulationen durchzuführen zu können, sind einige Vereinfachungen unerlässlich. Oftmals wird deswegen eine Modellauflösung verwendet, die die Prozesse der Tagesgrenzschicht gut darstellen kann, die jedoch für die Auflösung der nächtlichen Grenzschicht nicht ausreicht, was die Aussagekraft von Teilen der Simulationen (theoretisch) stark begrenzt. Diese Arbeit befasst sich mit einer Reihe von Fragen über die Aussagekraft solcher LES-Experimente: Wie schlecht wird die stabile, nächtliche Grenzschicht dargestellt, wenn die Modellauflösung nur eine unzureichende Darstellung der Turbulenz zulässt? Kann eine unzureichend aufgelöste, nächtliche Grenzschicht die Konvektion am folgenden Tag beeinflussen?

# Contents

# Chapter I

# Introduction

## 1.1 Motivation: there are (nearly) always smaller scales

Atmospheric processes cover a vast range of scales, from large planetary waves of $\mathcal{O}(10^{7}\ \mathrm{m})$ down to, for example, small microphysical processes of $\mathcal{O}(10^{-6}\ \mathrm{m})$ (Wallace and Hobbs, 2006). In numerical simulations/experiments of the atmosphere, it is currently not feasible to explicitly represent all these processes acting on such a wide range of scales, turning every experiment into a compromise between domain size, resolution, realism, and computational costs. The resolution introduces a division between processes with a length scale $\mathscr{L}$ larger than the grid spacing $\Delta$ – which can explicitly be resolved on the model grid – and processes with $\mathscr{L} < \Delta$, which (unless the process is being neglected) requires a sub-grid parameterization (e.g. Wyngaard, 2004).

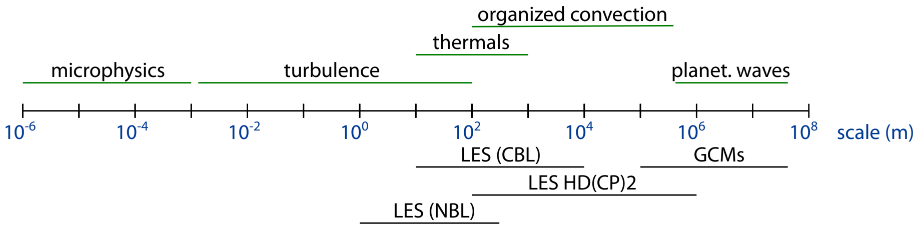

*Figure 1.1: Overview of the scale of some atmospheric processes, and the type of models used to study them.*

In the current generation general circulation models (GCMs) and, for example, limited area models used for numerical weather prediction (NWP), convection is one of those sub-grid processes which requires a parameterization. Although both the complexity and skill of these parameterizations has increased greatly, uncertainties related to (moist) convection and precipitation are still present in the current state-of-the-art GCMs (e.g. Stevens and Bony, 2013), making convection one of the major uncertainties in such models and causing biases in – amongst others – the frequency, onset or spatial distribution of precipitation (Jakob, 2010). A logical solution to remove the uncertainty associated with a convective parameterization, is to remove the parameterization itself. Several more fundamental methods, in which convection is explicitly resolved ($\Delta < \mathscr{L}$, with $\mathscr{L}$ representing some typical convective length scale), have been proposed and tested. Most notably, at least for model setups covering our entire planet Earth, are the experiments being performed with NICAM (Nonhydrostatic ICosahedral Atmospheric Model), using a horizontal grid spacing of ~1000 m (Miyamoto et al., 2013). Although at such resolutions deep convection is resolved (or permitted, Bryan et al., 2003), some smaller scale phenomena – like turbulence in the sub-cloud layer – still require a parameterization. In order to also resolve these processes, a further decrease in grid spacing to ~100 m is needed. At such a resolution, the largest (dry/shallow convective) eddies associated with the production and transport of turbulence are resolved; hence the name large-eddy simulation (LES), as such a model setup is mostly referred to. However, as shown in Fig. 1.1, there are (nearly) always smaller, relevant processes. One of those processes, which occurs frequently during clear conditions over land, is small scale shear-driven turbulence in the nocturnal stable boundary layer (NBL or SBL). For realistic LES experiments of the diel cycle of convection over land, such processes also need to be considered.

## 1.2 Large-eddy simulation of the atmospheric boundary layer

Since the seminal work of Smagorinsky (1963); Lilly (1966) and Deardorff (1970), LES has become an invaluable tool to study turbulence related (or dominated) atmospheric processes. By explicitly resolving the largest and most energetic eddies – and relying less on parameterizations as models based on the Reynolds averaged Navier-Stokes (RANS) equations – LES has proven to be very useful and reliable to study processes like convection, or aid in the development of e.g. RANS based models and the parameterizations that they depend on.

Traditionally, LES has mostly been used to perform fairly idealized experiments, for example within the Global Energy and Water Cycle Exchanges Project (GEWEX) Atmospheric Boundary Layer Study (GABLS) and Cloud System Study (GCSS) LES intercomparison cases (Bechtold et al., 1996; Stevens et al., 2001; Brown et al., 2002; Siebesma et al., 2003; Stevens et al., 2005; Beare et al., 2006; Ackerman et al., 2009; Vanzanten et al., 2011). For such idealized cases, the domain size and resolution is typically optimized for the kind of conditions being studied, where there are two distinct turbulence regimes: in the unstable convective boundary layer (CBL) and the stable boundary layer (SBL).

### 1.2.1 LES of the convective boundary layer

During the day a convective boundary layer is formed if the atmosphere is heated from below, and warm buoyant air starts rising in thermals. Convective clouds are formed if the air inside a thermal saturates, which – fueled by the release of latent heat – can extent all the way up to the tropopause (deep convection). Convective conditions have been studied extensively since some of the earliest work using LES (e.g. Deardorff, 1972; Sommeria, 1976; Moeng, 1984). The required setup in LES depends on the kind of convective conditions being studied. For dry and shallow convection a grid spacing of $\mathcal{O}$(10 m - 100 m) is typical (e.g. Brown et al., 2002; Siebesma et al., 2003; Vanzanten et al., 2011), which for deep convection is often increased to a few hundred meters (e.g. Hohenegger and Stevens, 2013). The horizontal and vertical extent of the domain has to be sufficiently large to allow the largest convective structures to develop. For dry and shallow convection this can be as small as a few kilometers, while deep convection might require domains which are a few hundred kilometers large (e.g. Hohenegger and Stevens, 2013; Schlemmer and Hohenegger, 2015).

### 1.2.2 LES of the stable boundary layer

When around sunset the net surface radiation becomes negative, the atmosphere is cooled from below and a stable boundary layer develops. In contrast to conditions with convection – where buoyancy produces turbulence – the positive buoyancy stratification in the SBL suppresses turbulence, produced (predominantly) by wind shear. As a result, the typical length scale of the turbulent eddies is much smaller than observed during convective conditions, and therefore requires a much finer computational mesh in LES (Fig. 1.2).

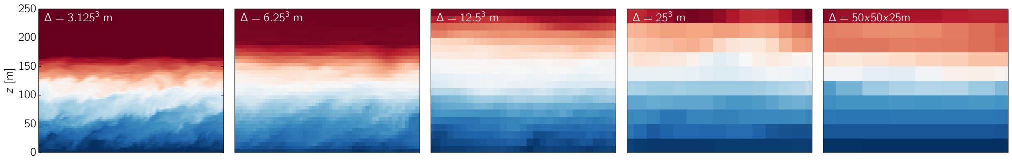

*Figure 1.2: Illustrative example of the small turbulent scales in the SBL. Shown is a vertical cross-section of potential temperature, from the experiments of Chapter 3.*

Since the first experiments by Mason and Derbyshire (1990), most work on LES of the SBL has focused on weakly stable conditions, like for example within the GABLS1 LES intercomparison (Beare et al., 2006). Even for weakly stable conditions, high-resolution experiments – with a grid spacing of $\mathcal{O}$(1 m) – are needed to resolve the small turbulent eddies, as illustrated in Fig. 1.2. Consequently, such experiments are limited to relatively small domains, typically with a horizontal extent of less than one kilometer.

## 1.3 Towards realistic large-eddy simulations

Over the last few years, LES has slowly moved from idealized experimental setups towards more realistic experiments, for example running LES continuously (days to years, forced by mesoscale models) to take a more statistical approach in the validation of convection parameterizations (Neggers et al., 2012) and studies of turbulence (Schalkwijk et al., 2015a), or realistic weather hindcasts on domains of hundreds of kilometers (Schalkwijk et al., 2015b) to a thousand kilometer, as currently being performed within the *High-Definition Clouds and Precipitation for Advancing Climate Prediction* (HD(CP)$^2$) project (e.g. Dipankar et al., 2015, `hdcp2.eu`). These realistic large domain LES experiments, using a resolution of 50 m - 200 m, are useful as a view into the future of (for example) NWP, but can also provide synthetic data for process studies of convection, to aid in the development of parameterizations.

However, in contrast to the idealized experiments where domain size and resolution are optimized for a single process, such realistic experiments encompass a variety of processes – ranging from small scale turbulence at night to large deep-convective systems during the day – thereby requiring both a resolution of $\mathcal{O}$(1 m), and a domain size of a few hundred kilometers.

It is easy to illustrate the infeasibility of such a setup by considering how LES experiments have evolved over the past 45 years. Figure 1.3 shows the increase in the total number of grid points as a function of time, used in a selected number of publications using LES and direct numerical simulations (DNS). In the past, as computer architectures (CPUs) advanced, a doubling of the total amount of grid points once every approximately 2.5 years was possible. In a best case scenario, if we naively assume that this trend will continue in the future, the kind of experiments currently performed within HD(CP)$^2$, at an increased resolution required to resolve the NBL ($\Delta =$ 1-10 m), won't be feasible for another 25 to 45 years. More realistic is a scenario where the performance of individual CPUs won't increase significantly, in which case an increase in the number of grid points can only be achieved by upscaling the number of CPU cores, which would require supercomputers which are orders of magnitude larger than current systems.

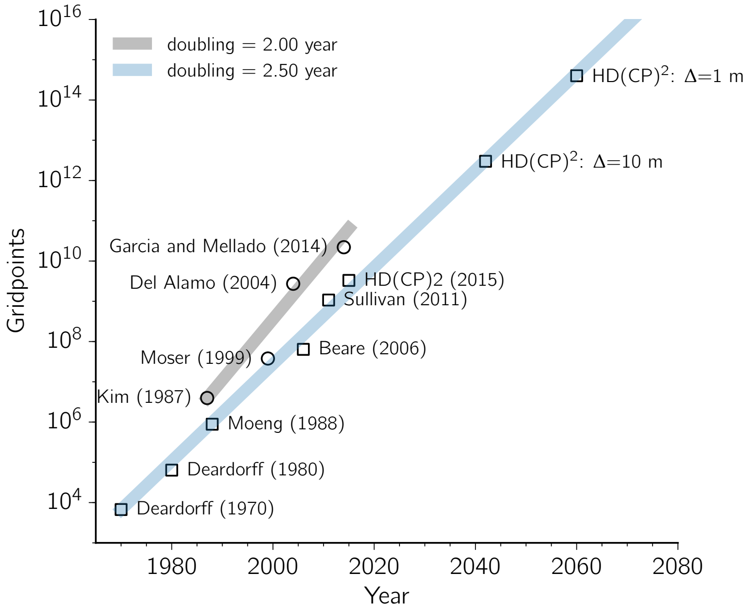

*Figure 1.3: Increase in the total number of grid points for a selection of DNS (circles) and LES (squares) publications.*

As we are decades away from resolving all relevant turbulent scales – both during day and night – in experiments such as currently performed within HD(CP)$^2$, some simplifications are required. In most cases (at least in the previously mentioned examples), the representation of turbulence at night is sacrificed by using a resolution sufficient to resolve the daytime boundary layer, but insufficient to resolve turbulence at night. Although unwanted, such sacrifices are necessary given the impossible computational demands necessary to resolve both (deep) convection and the SBL. This methodology, in which parts of the LES experiments are – strictly speaking – no longer LES, could be justified, but only if the poorly resolved parts of the experiments don't influence the periods of interest.

> *This thesis addresses a number of questions about the use of LES, in a setup where the resolution is sufficient to resolve daytime convection, but insufficient to resolve turbulence at night. How poorly is the nighttime boundary layer represented in LES when using a resolution insufficient to resolve turbulence? And can a poorly resolved / represented nocturnal boundary layer influence the following day of convection?*

## 1.4 Brief overview previous work

Both the question how stable boundary layers in LES behave when they are unresolved (or very poorly resolved), and the impact that might have on the following day of convection, has mostly been untouched in literature. For a variety of LES setups, and mostly for weakly stable conditions, sensitivity studies on resolution have been performed (e.g. Brown et al., 1994; Beare and Macvean, 2004; Beare et al., 2006; Sullivan et al., 2016), but limited to grid spacings of 12.5 m or less. In some of these cases, turbulence was poorly resolved, resulting in unrealistic vertical temperature profiles and an overestimation of the SBL depth. However, the impact on the following day of convection was never addressed.

As daytime convection typically develops from stable conditions in the early morning, details of the SBL are expected to influence the onset, development and characteristics of (moist) convection (Wetzel et al., 1996). Vilà-Guerau de Arellano (2007) studied the development of two consecutive days with convection, in which differences in nocturnal advection and vertical mixing resulted in two very different convective boundary layers: one with dry convection, and one with shallow cumulus. During the early morning transition, the combination of surface heating and entrainment of warm air from aloft has to overcome the nocturnal temperature inversion (Angevine et al., 2001). Any processes delaying this heating of the surface inversion layer, like fog or clouds reducing the incoming shortwave radiation, have the potential to delay the onset of convection (Yin et al., 2015; Anber et al., 2015).

Although all these studies addressed nocturnal or early morning processes which can influence daytime convection, none of them studied whether these processes can be influenced or caused by a poorly represented SBL in LES.

## 1.5 Outline thesis

Large-eddy simulation is a central theme in this thesis – being both the motivation for this work, and one of the tools used for our research – so we start in Chapter 2 with a brief description of the two LES models used in this thesis: the University of California Los Angeles, Large-Eddy Simulation (UCLA-LES) model (e.g. Stevens et al., 2005), and MicroHH (van Heerwaarden et al., 2016).

**The role of resolved turbulence**: The main benefit of using LES over RANS models is that turbulence is explicitly resolved, removing the need for a turbulence parameterization. However, at grid spacings of 100-200 m – as used within e.g. HD(CP)$^2$–

turbulence in the SBL will be mostly unresolved, likely degrading the skill of LES. In Chapter 3 we study how this affects the SBL development, and the following day of convection. Using observations from Hamburg and Cabauw we first study the typical summertime west European nights, in order to design a set of LES experiments which cover the typical conditions of our area of interest. Using three cases which cover a near complete diel cycle of dry convection (day - night - day), a sensitivity study on resolution is performed with UCLA-LES, varying the resolution in steps from $\Delta = 3.125^3$ m – with which we are capable of resolving most turbulence at night – to $\Delta = 100 \times 100 \times 25$ m – which is clearly insufficient to resolve the SBL. These experiments allow us to study the development of a poorly resolved SBL, and whether any biases in the representation of the SBL can influence the following day of convection.

**The role of moisture**: Although moisture was excluded from the study in Chapter 3, it can have a strong impact on the development of the SBL, through the formation of fog or low clouds and their interaction with radiation. If SBL biases arising from a poor representation of turbulent mixing influence the formation of fog or low clouds, this could further amplify the SBL biases. In Chapter 4 we use both observations (Hamburg, Karlsruhe and Cabauw) and a newly developed conceptual model, to study how likely this can happen. Using the observations we first examine the characteristics of the SBL, for example how often saturation occurs, or how close the conditions are to saturation. Next, a newly developed conceptual model is used to study whether overestimating vertical mixing (as observed in the experiments from Chapter 3) can cause a spurious formation of low clouds.

**Towards more strongly stable conditions in LES**: In Chapter 5 we take a small detour from the European conditions, and study the GABLS4 LES intercomparison case over the Antarctic. In contrast to most LES experiments which focus on the weakly stable boundary layer, this case is in the so-called transitionally stable regime, where the turbulent intensity quickly decreases with increasing stability. As similar conditions can also occur over continental Europe, we address the question whether it is possible – within reasonable limits on the computational costs – to obtain a valid LES experiment for such a transitionally stable case.

Finally in Chapter 6, we summarize the main findings of this thesis.

# Chapter II

# Model description

Throughout this thesis two different LES models are used: the University of California Los Angeles, Large-Eddy Simulation (UCLA-LES) code in Chapter 3 (e.g. Stevens et al. 2005), and MicroHH in Chapter 5 (van Heerwaarden et al., 2016). This chapter introduces LES in general, and describes the (for this thesis) relevant parts of UCLA-LES and MicroHH.

*Parts of this chapter are from van Heerwaarden et al. (2016), of which the author of this thesis is the second author.*

## 2.1 General considerations on large-eddy simulation

Turbulence in the atmosphere covers a vast range of scales — for processes in the atmospheric boundary layer (ABL) ranging from the Kolmogorov microscales at which kinetic energy is dissipated ($\mathcal{O}(10^{-2} - 10^{-3}$ m) up to scales as large as the ABL itself where kinetic energy is produced and transported ($\mathcal{O}(10^{3} - 10^{4})$ m). To represent these processes in meteorological models, several approaches can be applied.

In direct numerical simulation — the most fundamental approach — all relevant turbulent processes are directly represented by numerically integrating the Navier-Stokes (NS) equations. The advantage of this approach is that all turbulent scales are explicitly represented, removing the need of a turbulence closure. However, given the requirements on grid spacing and current limits on computational resources, these type of simulations are limited to Reynolds numbers which are much smaller than typically observed in our atmosphere. The exact opposite approach is currently applied in most operational weather forecasting / general circulation models. By using the Reynolds averaged Navier-Stokes (RANS) equations (Reynolds, 1895), the influence of turbulence is modelled and only the evolution of mean quantities is explicitly calculated. While this allows for domains are large as our planet Earth, it requires a representation of processes acting on scales smaller than the averaging domain (subgrid processes), introducing a fair amount of uncertainty.

LES is positioned in between both approaches. Turbulent processes in the ABL can be divided into large scales at which turbulence is produced and transported, and smaller scales at which energy is dissipated to heat. At intermediate scales (inertial sub-range) there is a constant drainage (cascade) of energy from the large producing/transporting scales to the small dissipating scales. The philosophy behind LES is to explicitly represent the large scales (the *large eddies*), and to model the small dissipating scales using a sub-grid or sub-filter scale diffusion model.

## 2.2 Introduction UCLA-LES and MicroHH

UCLA-LES (e.g. Stevens et al. 2005) is a well-proven and comprehensive LES code, with amongst other options for representing radiative transfer (e.g. Pincus and Stevens, 2009), warm/ice microphysics (e.g. Seifert and Beheng, 2006), land-surface processes (Rieck et al., 2014), and/or Lagrangian particles and droplets (Naumann and Seifert, 2015). The model is coded in Fortran 90, using the Message Passing Interface (MPI) for parallelization, and NetCDF for most of its output. The model code is available under the GNU General Public License v3.0 (GNU-GPLv3) at `http://github.com/uclales`.

MicroHH was developed during the last few years, with the aim of creating a cleanly structured, efficient and highly parallel LES and DNS (direct numerical simulation) model (van Heerwaarden et al., 2014; van Heerwaarden and Mellado, 2016). MicroHH is coded in C++ (and CUDA-C), using MPI for parallelization, netCDF for the output of statistics, and MPI-IO for the in- and output of two and three-dimensional fields. As part of this thesis, we explored the use of NVIDIA Graphical Processing Units (GPUs), which is described in more detail in section 2.6.1. A reference paper is currently in preparation (van Heerwaarden et al., 2016). Like UCLA-LES, MicroHH is an open-source code, released under the GPLv3 license at `http://github.com/microhh` and `http://microhh.org`.

Both UCLA-LES an MicroHH share many similarities in the choice of governing equations, numerics, and parameterizations like the surface and sub-grid schemes. Therefore we will describe most parts of the models in general, and where necessary indicate their differences. Both models (and especially UCLA-LES) have many options which were not used for this thesis. For the sake of brevity, the description in this chapter will exclude those components.

## 2.3 Governing equations

LES solves the filtered Navier-Stokes equations, where the filtering operation in both UCLA-LES and MicroHH is implicit. The prognostic variables are the three wind components ($\widetilde{u}_i$), and optionally the potential or liquid water potential temperature ($\widetilde{\theta}$ or $\widetilde{\theta}_\mathrm{l}$), specific humidity ($\widetilde{q}_\mathrm{t}$), and/or inert scalars ($\widetilde{\phi}$). Assuming incompressibility, the governing equations (in the anelastic approximation) in tensor notation read:

$$\begin{aligned}
\frac{\partial \widetilde{u}_i}{\partial t} &= -\frac{1}{\rho_0}\frac{\partial \rho_0 \widetilde{u}_i \widetilde{u}_j}{\partial x_j} - \frac{1}{\rho_0}\frac{\partial \widetilde{p}'}{\partial x_i} + b\delta_{i3} + f_c(\widetilde{u}_j - V_{\mathrm{g}j})\epsilon_{ijk} + \frac{1}{\rho_0}\frac{\partial \rho_0 \tau_{ij}}{\partial x_j}, && (2.1)\\
\frac{\partial \widetilde{\phi}}{\partial t} &= -\frac{1}{\rho_0}\frac{\partial \widetilde{\phi}\widetilde{u}_j}{\partial x_j} + \frac{1}{\rho_0}\frac{\partial (\rho_0 \gamma_{\phi j})}{\partial x_j}, && (2.2)\\
\frac{\partial \rho_0 \widetilde{u}_i}{\partial x_i} &= 0, && (2.3)
\end{aligned}$$

with additionally an equation of state:

$$\theta_\mathrm{v} = \theta\left(1 + \left[\frac{R_\mathrm{v}}{R_\mathrm{d}} - 1\right] q_\mathrm{t} - \frac{R_\mathrm{v}}{R_\mathrm{d}} q_\mathrm{l}\right), \tag{2.4}$$

where $\rho_0$ is the base-state density, $b = g(\widetilde{\theta}_\mathrm{v} - \theta_\mathrm{v0})/\theta_\mathrm{v0}$ the buoyancy with $\theta_\mathrm{v0}$ the base-state virtual potential temperature, $f_\mathrm{c}$ the coriolis parameter, $V_\mathrm{gj}$ the geostrophic wind, $R_\mathrm{d}$ and $R_\mathrm{v}$ the gas constants for dry air and water vapor, and $\tau_{ij} = \widetilde{u_i u_j} - \widetilde{u}_i \widetilde{u}_j$ and $\gamma_{\phi j} = \widetilde{\phi u_j} - \widetilde{\phi}\widetilde{u_j}$ the sub-grid momentum and scalar fluxes, which are further discussed in Section 2.5.1. The Kronecker Delta and Levi-Civita symbol are denoted by $\delta_{i3}$ and $\epsilon_{ijk}$, respectively. The anelastic approximation is based on Ogura and Phillips (1962) in UCLA-LES, and based on Bannon (1996) in MicroHH.

## 2.4 Numerics

### 2.4.1 Grid and spatial discretization

UCLA-LES and the LES part of MicroHH are discretized using finite differences, using (predominantly[1]) second-order accurate spatial operators. The direct numerical simulation part of MicroHH (which won't be further discussed here) is based on fourth-order accurate operators. The variables are placed on a staggered (Arakawa-C) grid, with scalars located at the cell centers, and velocities at the cells edges. (Fig. 2.1, note the differences in the placement of the velocity locations relative to the scalar location

---

[1] Some operations, like for example interpolations within advection schemes, optionally use higher-order methods

in UCLA-LES and MicroHH). Interpolations are approximated as (e.g. for MicroHH, for an interpolation of $S$ to the location of $u$):

$$S_{i-\frac{1}{2},j,k} \approx a_1\ S_{i-2,j,k} + a_2\ S_{i-1,j,k} + a_3\ S_{i,j,k} + a_4\ S_{i+1,j,k}, \tag{2.5}$$

where $a = \left\{0, \frac{1}{2}, \frac{1}{2}, 0\right\}$ for the 2nd order interpolations and $a = \left\{\frac{-1}{16}, \frac{9}{16}, \frac{9}{16}, \frac{-1}{16}\right\}$ for the 4th order interpolations in MicroHH and $a = \left\{\frac{-1}{12}, \frac{7}{12}, \frac{7}{12}, \frac{-1}{12}\right\}$ for the fourth order interpolations in UCLA-LES (Wicker and Skamarock, 2002). Gradients are approximated as (e.g. for the gradient of $u$ in the x-direction at the scalar location in MicroHH):

$$\left.\frac{\partial u}{\partial x}\right|_{i+\frac{1}{2},j,k} \approx \frac{u_{i+1,j,k} - u_{i,j,k}}{\Delta x}. \tag{2.6}$$

The grid spacing in the horizontal ($\Delta x$, $\Delta y$) is always assumed to be constant throughout the domain, in the vertical ($\Delta z$) a variable grid spacing is supported. Both horizontal directions have cyclic boundary conditions.

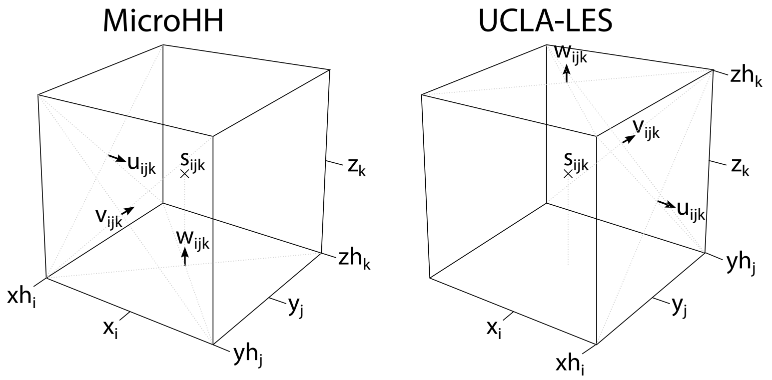

*Figure 2.1: Location of variables on the staggered Arakawa-C grid in MicroHH (left) and UCLA-LES (right), with the full (x, y, z) and half (xh, yh, zh) levels.*

## 2.4.2 Time integration

### 2.4.2.1 UCLA-LES

UCLA-LES uses a third-order Runge Kutta (RK) scheme, where the time integration is performed in three sub-steps:

$$\widetilde{\phi}^{n+1} = \widetilde{\phi}^{n} + a^n \frac{\partial \widetilde{\phi}^{n}}{\partial t} \Delta t + b^n \frac{\partial \widetilde{\phi}^{n-1}}{\partial t} \Delta t, \tag{2.7}$$

for n = {1,2,3}, with $a^n = \left\{\frac{8}{15}, \frac{15}{12}, \frac{3}{4}\right\}$ and $b^n = \left\{0, -\frac{17}{60}, -\frac{15}{12}\right\}$

#### 2.4.2.2 MicroHH

MicroHH supports both third (Williamson, 1980) and fourth order (Carpenter and Kennedy, 1994) low-storage Runge-Kutta schemes. The schemes require only two three dimensional (3D) fields per variable; one for the field itself, and one for its tendency. In contrast, the scheme in UCLA-LES requires the storage of both the tendency at the current and previous RK step, introducing one additional 3D field per variable. Such low storage schemes are beneficial in general, but even more for experiments on GPU's, where the amount of available memory is often limited. In generic form, the time integration can be written as:

$$
\begin{aligned}
\delta\phi^n &= \frac{\partial\widetilde{\phi}^n}{\partial t} + a^n \delta\phi^{n-1}, &\quad (2.8)\\
\widetilde{\phi}^{n+1} &= \widetilde{\phi}^n + b^n \delta\phi^n \Delta t, &\quad (2.9)
\end{aligned}
$$

With the coefficients $a^n = \left\{0, -\frac{5}{9}, -\frac{153}{128}\right\}$ and $b^n = \left\{\frac{1}{3}, \frac{15}{16}, \frac{8}{15}\right\}$ for the third-order scheme, and $a^n = \left\{0, -\frac{567301805773}{1357537059087}, -\frac{2404267990393}{2016746695238} - \frac{3550918686646}{2091501179385}\right\}$ and $b^n = \left\{\frac{1432997174477}{9575080441755}, \frac{5161836677717}{13612068292357}, \frac{1720146321549}{2090206949498}, \frac{3134564353537}{4481467310338}, \frac{2277821191437}{14882151754819}\right\}$ for the fourth-order scheme.

## 2.5 Physical parameterizations

### 2.5.1 Sub-grid diffusion

Both UCLA-LES and MicroHH use a Smagorinsky-Lilly (SL) model (e.g. Smagorinsky, 1963; Lilly, 1966), in which the sub-grid momentum flux $\tau_{ij}$ is modeled as being proportional to the filtered rate of strain, and the sub-grid scalar flux $\gamma_{\phi j}$ as proportional to the scalar gradient:

$$
\tau_{ij} = \widetilde{u_i u_j} - \widetilde{u_i}\widetilde{u_j} = -2K_\mathrm{m}\widetilde{S}_{ij}, \quad (2.10)
$$

$$
\gamma_{\phi j} = \widetilde{\phi u_j} - \widetilde{\phi}\widetilde{u_j} = -K_\mathrm{h}\frac{\partial\widetilde{\phi}}{\partial x_i}, \quad (2.11)
$$

with $\widetilde{S}_{ij}$ the filtered rate of strain:

$$
\widetilde{S}_{ij} = \frac{1}{2}\left(\frac{\partial\widetilde{u}_i}{\partial x_j} + \frac{\partial\widetilde{u}_j}{\partial x_i}\right). \quad (2.12)
$$

$K_\mathrm{m}$ is the eddy viscosity, and $K_\mathrm{h} = K_\mathrm{m}/\mathrm{Pr_t}$ the eddy diffusivity, with $\mathrm{Pr_t}$ the turbulent Prandtl number. Within the SL-model, the eddy viscosity is modeled as:

$$K_\mathrm{m} = \lambda^2 \sqrt{2\widetilde{S}_{ij}\widetilde{S}_{ij}} = (C_\mathrm{s}\Delta)^2 \, S, \tag{2.13}$$

where $C_\mathrm{s}$ is the Smagorinsky constant and $\Delta$ a mixing length scale, typically defined as $\Delta = (\Delta_x \Delta_y \Delta_z)^{1/3}$. For cases which involve buoyancy, the eddy viscosity is corrected as (Lilly, 1962):

$$K_\mathrm{m} = (C_\mathrm{s}\Delta)^2 \, S \sqrt{1 - \frac{\mathrm{Ri}}{\mathrm{Pr_t}}}, \tag{2.14}$$

where $\mathrm{Ri} = N^2/S^2$ is the Richardson number, with $N^2$ the squared Brunt-Väisälä frequency. Near the surface, the length scale $\lambda$ is decreased as (Mason and Thomson, 1992):

$$\frac{1}{\lambda^n} = \frac{1}{\lambda_0^n} + \frac{1}{(\kappa z)^n}, \tag{2.15}$$

where $\lambda_0^n$ is the uncorrected length scale, $\kappa$ the Von Kármán constant, $z$ the distance to the surface, and $n$ a parameter (equal to $n = 2$ in both UCLA-LES and MicroHH).

### 2.5.2 Surface layer parameterization

In most cases, LES requires a parameterization of the surface momentum ($\widetilde{uw}_0$, $\widetilde{vw}_0$) and scalar (e.g. $\widetilde{\phi w}_0$) fluxes, which enter the model as the sub-grid flux at the surface. UCLA-LES and MicroHH have several options to prescribe or calculate them. For all cases we will assume a no-slip lower boundary conditions. Most options require Monin-Obukhov similarity theory (Monin and Obukhov, 1954), in which the surface fluxes, and gradients within the surface layer, are assumed to be related as:

$$\frac{\kappa z_1}{u_*}\frac{\partial U}{\partial z} = -\frac{\kappa z_1 u_*}{\widetilde{uw}_0}\frac{\partial \widetilde{u}}{\partial z} = -\frac{\kappa z_1 u_*}{\widetilde{vw}_0}\frac{\partial \widetilde{v}}{\partial z} = \Phi_\mathrm{m}\left(\frac{z_1}{L}\right), \tag{2.16}$$

$$-\frac{\kappa z_1 u_*}{\widetilde{\phi w}_0}\frac{\partial \widetilde{\phi}}{\partial z} = \Phi_\mathrm{h}\left(\frac{z_1}{L}\right), \tag{2.17}$$

where $u_*$ is the surface friction velocity, $U = \sqrt{u^2 + v^2}$, $\Phi_\mathrm{m}$ and $\Phi_\mathrm{h}$ are empirical stability functions, and $L$ is the Obukhov length:

$$L = -\frac{u_*^3}{\kappa\,\widetilde{bw}_0}, \tag{2.18}$$

with $\widetilde{bw}_0$ the surface buoyancy flux. These relations can be integrated from the roughness length ($z_{0\mathrm{m}}$, $z_{0\mathrm{h}}$) to the first model level to obtain (e.g. ECMWF, 2011):

$$\begin{aligned} u_* &= f_\mathrm{m}(U_1), & (2.19)\\ -\frac{\widetilde{\phi w}}{u_*} &= f_\mathrm{h}(\widetilde{\phi}_1 - \widetilde{\phi}_0), & (2.20) \end{aligned}$$

with

$$\begin{aligned} f_\mathrm{m} &= \frac{\kappa}{\ln\left(\frac{z_1}{z_{0\mathrm{m}}}\right) - \Psi_\mathrm{m}\left(\frac{z_1}{L}\right) + \Psi_\mathrm{m}\left(\frac{z_{0\mathrm{m}}}{L}\right)}, & (2.21)\\ f_\mathrm{h} &= \frac{\kappa}{\ln\left(\frac{z_1}{z_{0\mathrm{h}}}\right) - \Psi_\mathrm{h}\left(\frac{z_1}{L}\right) + \Psi_\mathrm{h}\left(\frac{z_{0\mathrm{h}}}{L}\right)}. & (2.22) \end{aligned}$$

The stability functions differ between MicroHH and UCLA-LES, and are provided at the end of this section. Depending on the surface boundary conditions, three different Richardson numbers can be defined as:

- Prescribed surface momentum and buoyancy flux:

$$\mathrm{Ri} = \frac{z_1}{L} = -\frac{\kappa z_1 \widetilde{bw}_0}{u_*^3}. \tag{2.23}$$

- Prescribed surface buoyancy flux and calculated momentum flux:

$$\mathrm{Ri} = \frac{z_1}{L} f_\mathrm{m}^3 = -\frac{\kappa z_1 \widetilde{bw}_0}{u_1^3}. \tag{2.24}$$

- Prescribed surface buoyancy value and calculated momentum flux:

$$\mathrm{Ri} = \frac{z_1}{L} \frac{f_\mathrm{m}^2}{f_\mathrm{h}} = \frac{\kappa z_1 \,(b_1 - b_0)}{u_1^2}. \tag{2.25}$$

In Eq. 2.24 and 2.25, the left-hand side has to be solved for the value of $L$, either iteratively (UCLA-LES, see ECMWF, 2011, p37), or by the use of a lookup table with pre-calculated values of the left-hand size (MicroHH).

#### 2.5.2.1 Stability functions MicroHH

MicroHH uses the stability functions from Wilson (2001) for unstable conditions, and the functions from Högström (1988) for stable conditions:

$$\Phi_{\mathrm{m,h}} = \begin{cases} \left(1 + c_1 |\zeta|^{2/3}\right)^{1/2} & \text{unstable} \\ 1 + c_2\, \zeta & \text{stable} \end{cases} \tag{2.26}$$

$$\Psi_{\mathrm{m,h}} = \begin{cases} 3 \log\left(\frac{1+\Phi_{\mathrm{m,h}}^{-1}}{2}\right) & \text{unstable} \\ -c_2\, \zeta & \text{stable} \end{cases} \tag{2.27}$$

where for momentum (m) $c_1 = 3.6$, $c_2 = 4.8$ and for heat (h) $c_1 = 7.9$, $c_2 = 7.8$.

#### 2.5.2.2 Stability functions UCLA-LES

UCLA-LES used the Businger-Dyer stability functions (e.g. Paulson, 1970; Businger, 1988) for unstable conditions:

$$\Phi_{\mathrm{m,h}} = (1 - c_3\, \zeta)^{c_4}, \tag{2.28}$$

$$\Psi_{\mathrm{m}} = \frac{\pi}{2} - 2\,\mathrm{atan}(x) + \log\left(\frac{(1+x)^2(1+x^2)}{8}\right), \tag{2.29}$$

$$\Psi_{\mathrm{h}} = 2\log\left(\frac{1+x^2}{2}\right), \tag{2.30}$$

$$x = (1 - c_3\, \zeta)^{1/4}, \tag{2.31}$$

with $c_3$ = 16, $c_4$ = -1/4 for momentum, and $c_3$ = 15, $c_4$ = -1/2 for heat. For stable conditions, the integrated functions from Holtslag and De Bruin (1988) are used:

$$\Psi_{\mathrm{m}} = -b\left(\zeta - \frac{c}{d}\right)\, \exp(-d\zeta) - a\zeta\, \frac{bc}{d}, \tag{2.32}$$

$$\Psi_{\mathrm{h}} = -b\left(\zeta - \frac{c}{d}\right)\, \exp(-d\zeta) - \left(1 + \frac{2}{3}a\zeta\right)^{1.5} - \frac{bc}{d} + 1, \tag{2.33}$$

where $a$=1, $b$=2/3, $c$=5, and $d$=0.35.

## 2.6 Benchmarks and validation MicroHH

As part of this thesis, I helped in the development of MicroHH, mostly focused on the LES component, and the realization of a model version capable of running on graphics processing units (GPUs). This section briefly summarizes some of the outcomes and results of that work, including a validation of MicroHH against two well-known LES intercomparison cases: for convective conditions the BOMEX (non-precipitating shallow convection) case (Siebesma et al., 2003), and for stable conditions the GABLS1 case (Beare et al., 2006).

### 2.6.1 GPU implementation

Within MicroHH we explored the possibility of performing experiments on graphical processing units (GPUs). Although originally intended for – as the name implies – the processing of graphics on computers, the use of GPUs has now been extended to general purpose computing (GPGPU) and scientific research. Compared to central processing units (CPUs), which typically consist of <20 computing cores, GPU's have thousand of cores, which – despite the fact that GPU cores are more elementary and run at lower clock speeds – have shown to provide speedups of a factor 10 - 100 for certain algorithms, compared to CPUs (e.g. Luebke, 2008).

Within computational fluid dynamics (CFD) and atmospheric modeling, the use of GPU's is slowly emerging. Roughly speaking, two paths can be pursued when improving the performance of a conventional CPU code using GPU's: either by offloading certain expensive computations, like a microphysics or radiative transfer routine, to the GPU (e.g. Michalakes and Vachharajani, 2008; Mielikainen et al., 2012), or by porting the entire model (or at least, all components involved in the time integration) to the GPU (e.g. Schalkwijk et al., 2012). Although the latter requires significantly more effort to realize, it eliminates the need for continuous memory copies between CPU-GPU, providing a greater potential for performance.

Like Schalkwijk et al. (2012), we implemented all model components involved in the time integration (excluding in/output and statistics) on the GPU, using NVIDIA's CUDA-C language. The choice between the CPU and GPU version is made at compile time, enabling the respective computational kernels through the use of pre-compiler statements. Both the algorithms and numerical precision (double) are identical in the CPU and GPU versions, resulting in (statistically) identical results between both model versions. Currently MicroHH only supports the use of a single GPU, in the (near) future this will be extended to multiple GPUs. Despite this limitation, the first results of our GPU implementation look promising, as shown in Table 2.1. For a sufficiently large setup, the speedup obtained with the GPU version is ~30× compared to a single CPU core, ~3× compared to a single node on the Thunder supercomputer (16 CPU cores), and approximately 64 CPU cores (4 Thunder nodes) are required to outperform a single GPU.

*Table 2.1: Speedup obtained with a single NVIDIA Quadro K6000 GPU, over the use of "n" Intel Xeon E5-2670 CPU cores (8 cores per CPU, 2 CPUs per compute node). Results are for the BOMEX case (Siebesma et al., 2003).*

| grid points | $n$=1 | $n$=16 | $n$=32 | $n$=64 |
|---:|---:|---:|---:|---:|
| 64×64×64 | 18.49 | 1.93 | 1.14 | 0.95 |
| 128×128×128 | 28.01 | 2.98 | 1.51 | 0.92 |
| 256×256×256 | 27.76 | 3.02 | 1.59 | 0.91 |
| 512×512×384 | 29.88 | 3.03 | 1.56 | 0.86 |

### 2.6.2 Validation BOMEX and GABLS1 cases

In this section we very briefly compare MicroHH to two well-known LES intercomparison cases: the BOMEX case with shallow non-precipitating convection (Siebesma et al., 2003), and the GABLS1 case for stable conditions (Beare et al., 2006). For both cases, the LES results from all the intercomparison participants are available online, allowing for a direct comparison of MicroHH against a variety of other LES models.

#### 2.6.2.1 BOMEX

For the BOMEX case, we follow the exact case setup described in Siebesma et al. (2003). As MicroHH currently doesn't have a monotonic advection scheme, a centered 2nd order accurate scheme was used, with sub-grid diffusion performed with the Smagorinsky-Lilly model (with $C_s$=0.23, $\mathrm{Pr}_t$=1/3).

Like in Siebesma et al. (2003), some statistics are conditionally averaged over grid points defined as a cloud (positive liquid water content) or cloud core (positive liquid water content, and positively buoyant). Fig. 2.2 shows the vertical profiles of the cloud fraction, liquid water potential temperature ($\theta_l$), total specific humidity ($q_t$) and vertical velocity ($w$), averaged between $t$ = 5 - 6 hours. All mean and conditionally sampled statistics are predominantly within one standard deviation (shaded area) of the mean results from Siebesma et al. (2003).

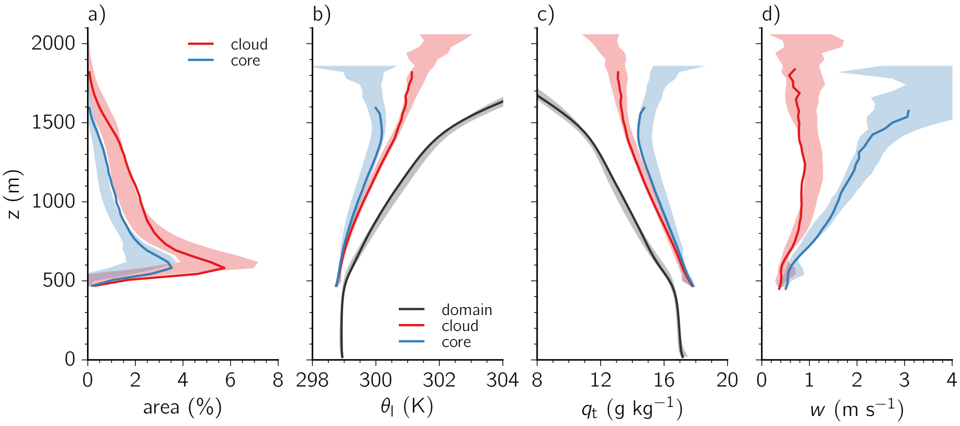

*Figure 2.2: Results for the BOMEX case: a) cloud are, b) liquid water potential temperature, c) total specific humidity and d) vertical velocity. The solid lines show the results from MicroHH, the shaded area the mean ± one standard deviation of the results from Siebesma et al. (2003).*

#### 2.6.2.2 GABLS1

For the GABLS1 case we follow the exact case setup from Beare et al. (2006), using an isotropic grid spacing of $\Delta = 2$ m. At larger grid spacings the model has difficulties in becoming turbulent, which can also be observed in some of the results from Beare et al. (2006). A second order accurate advection scheme with fourth order accurate interpolations was used, with the Smagorinsky-Lilly model for the sub-grid diffusion ($C_s$=0.12, $\mathrm{Pr_t}$=1/3). Fig. 2.3 shows the vertical profiles of potential temperature and the zonal wind component (averaged over the period $t$ = 8 - 9 h), and times series

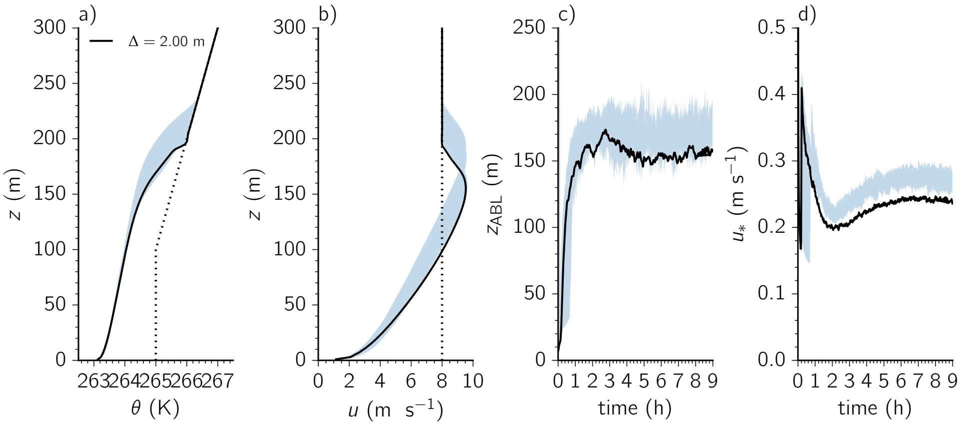

*Figure 2.3: Results for the GABLS1 case: a) potential temperatur, b) zonal wind component, c) SBL depth, d) surface friction velocity. The solid lines show the results from MicroHH, the shaded are the spread in the results from Beare et al. (2006).*

of the boundary layer depth and surface friction velocity. Compared to the range of results from Beare et al. (2006), the surface friction velocity $u_*$ is on the low side, and as a result, a similar trend is visible in the boundary layer depth (e.g. Zilitinkevich and Mironov, 1996, and references therein). Nonetheless, the vertical profiles are within the range of results obtained from other LES codes.

## Chapter III

# The influence of misrepresenting the nocturnal boundary layer on idealized daytime convection in large-eddy simulation

The influence of poorly resolving mixing processes in the nocturnal boundary layer (NBL) on the development of the convective boundary layer the following day is studied using large-eddy simulation (LES). Guided by measurement data from meteorological sites in Cabauw (Netherlands) and Hamburg (Germany), the typical summertime NBL conditions for Western Europe are characterized, and used to design idealized (absence of moisture and large-scale forcings) numerical experiments of the diel cycle. Using the UCLA-LES code with a traditional Smagorinsky-Lilly subgrid model and a simplified land-surface scheme, a sensitivity study to grid spacing is performed. At horizontal grid spacings ranging from 3.125 m in which we are capable of resolving most turbulence in the cases of interest, to grid a spacing of 100 m which is clearly insufficient to resolve the NBL, the ability of LES to represent the NBL, and the influence of NBL biases on the subsequent daytime development of the convective boundary layer are examined. Although the low-resolution experiments produce substantial biases in the NBL, the influence on daytime convection is shown to be small, with biases in the afternoon boundary layer depth and temperature of approximately 100 m and 0.5 K, which partially cancel each other in terms of the mixed-layer top relative humidity.

*This chapter has been published as van Stratum and Stevens (2015)*

## 3.1 Introduction

Moist convection remains one of the major uncertainties in general circulation models (GCMs), causing biases in (amongst others) the frequency, onset or spatial distribution of precipitation (Jakob, 2010). Although the complexity of sub-grid scale parameterizations has greatly increased, uncertainties related to clouds and precipitation (CP) continue to exist in current state-of-the-art GCMs (Stevens and Bony, 2013). To increase the understanding and to ultimately improve the representation (parameterization) of CP processes, a number of initiatives exploiting high-performance computing have been launched, for example the Cascade project (Holloway et al., 2012) or high-resolution experiments with NICAM (Nonhydrostatic ICosahedral Atmospheric Model, Miyamoto et al., 2013). Both initiatives use a (horizontal) grid spacing $\Delta_x$ of 1 km - 2 km. For dry and shallow convection, these grid spacings approach the size of the largest convective eddies and convection becomes partially (but poorly) resolved (Honnert et al., 2011). With convection being neither fully resolved, nor fully parameterized, modeling in this area is challenging. As such, grid spacings in the range from ~500 m to ~3 km are often referred to as the convective grey zone or terra incognita (e.g. Wyngaard, 2004; Zhou et al., 2014).

Recently the German ministry for education and research (BMBF) launched an initiative termed *High Definition Clouds and Precipitation for Advancing Climate Prediction* [HD(CP)$^2$]. This initiative strives to perform large-eddy simulation (LES) hind casts of diurnal cycles of convection using horizontal grid spacings of $\Delta_x \approx 100$ m on spatial scales as large as Germany ($1000^2$ - $1500^2$ km), and then expanding the domain size as more computational resources become available with time. In contrast with models relying on the Reynolds-Averaged Navier-Stokes (RANS) equations like standard GCMs, LES at grid spacings of 100 m explicitly resolves the most energetic eddies related to both dry and shallow convection. Thereby it attempts to leap over the aforementioned modeling issues in the convective grey zone and reduce the uncertainty related to convection. For relatively large domains, these type of experiments can be a useful source of synthetic data to study CP processes in detail.

However, even though grid spacings of 100 m are sufficient to represent convection, it leaves some other processes unresolved. One of these processes, relevant for the diurnal cycle of convection over land, is the stable nocturnal boundary layer (NBL). Even for weak to moderately stable conditions, LES of the NBL requires a grid spacing of $\mathcal{O}(1m)$ (Beare et al., 2006), which greatly increases the computational burden. To illustrate this point, consider that every doubling of resolution (at a constant

Courant number) increases the computational costs with roughly a factor 16. A grid refinement from current limited-area models (e.g. COSMO-DE at $\Delta_x = 2800$ m, Baldauf et al. (2011)) to convection resolving experiments ($\Delta_x = 100$ m) implies a computational increase of $\mathcal{O}(10^5 - 10^6)$, which is ambitious but conceivable in the near future. An additional increase in computational costs of $\mathcal{O}(10^8)$, which would be required for $\Delta_x = 1$ m, is not. If the representation of the NBL ends up being crucial to the development of convective processes during the day this bodes poorly for attempts to use more fundamental approaches, like LES, to understand CP processes. So do we need to resolve the NBL to accurately study daytime convection?

The NBL plays a crucial role in numerical weather prediction (NWP, e.g. near-surface temperatures, fog or air pollution; Fernando and Weil (2010); Holtslag et al. (2013)), but these details might be of secondary importance for studies focused on the daytime convective boundary layer (CBL). From this perspective, some errors in the representation of the NBL may be tolerable, as long as they don't significantly influence the development or characteristics of the CBL. Vilà-Guerau de Arellano (2007) demonstrated with different methods that differences in the early morning characteristics of the NBL and free troposphere can significantly effect daytime convection and the formation of shallow cumulus. Whether such different initial conditions can arise from a poorly represented NBL in low-resolution LES is currently unknown.

As LES modeling of the diurnal cycle of convection requires both a sufficiently sized domain to capture the large convective eddies, and high resolution to resolve the small-scale nocturnal eddies, the NBL and CBL have primarily been addressed individually (e.g. Mason and Derbyshire, 1990; Brown et al., 2002). The implications of under-resolving the NBL was — to some extent — addressed in the first Global Energy and Water Cycle Exchanges Project (GEWEX) Atmospheric Boundary Layer Study (GABLS1) LES intercomparison (Beare et al., 2006). Their results indicate that with decreasing resolution the NBL deepens, but their range of grid spacings was limited to $\Delta_x \leq 12.5$ m, and without addressing the development of convection on the subsequent day. Only recently has the increase in computational resources and development of dynamic subgrid-scale (SGS) models made LES studies covering (near) full diurnal cycles possible (Kleissl et al., 2006; Kumar et al., 2006; Basu et al., 2008b; Kumar et al., 2010).

Despite their promising results, these dynamic schemes require a sufficiently resolved turbulence field to determine the subgrid-scale parameters. Prior to this study we tested two more advanced subgrid models for the GABLS1 case: the scale-dependent Lagrangian dynamic model (Bou-Zeid et al., 2005; Huang et al., 2008) and the stretched-vortex model (Chung and Matheou, 2014). Although both schemes perform well when turbulence is moderately underresolved, they fail at the coarse grid spacings addressed in this study, where turbulent mixing ceases. For this reason, and because we anticipate that simple subgrid-scale closures will remain attractive for convective scale modeling, the remainder of this study focuses on the traditional Smagorinsky-Lilly model.

What happens if we simulate the diurnal cycle of convection using a LES setup with a crude representation of the SGS processes, with (horizontal) grid spacings as coarse as 100 m? How poorly is the NBL represented, and could potential biases in its development influence daytime convection? We address these questions with a number of idealized experiments covering a near complete diel cycle of convection over land.

To develop a foundational understanding of these issues, our study focuses on the dynamical aspects: the ratio of explicitly resolved turbulence versus the fraction modeled by the SGS model at various grid spacings, and its implication for the NBL development and the development of the subsequent day of convection for a dry case (no moisture). Although both moisture and radiation are likely to be relevant to many situations (e.g. Duynkerke, 1999), the issues that we investigate are likely to be common to all cases. With moist convection being rooted in the dry sub-cloud layer (e.g. van Stratum et al., 2014), any issues with representing such a relatively simple dry CBL are inevitably going to be reflected on the development and characteristics of more complex cases with moist convection. To design the experiments, we first obtain the typical summertime NBL characteristics from measurement data representative for Western European conditions. This region was chosen for focus because of its relevance for HD(CP)$^2$ and availability of meteorological measurement sites at Cabauw (The Netherlands) and Hamburg (Germany). Deriving typical boundary forcings like wind speed and surface cooling allows for the design of numerical experiments that cover the observed conditions, without having to deal with what we believe to be secondary details (e.g. case specific, complicated synoptic scale forcings). For each experiment we perform a sensitivity study on resolution, ranging the grid spacing from 3.125 m in which we are capable of resolving most turbulence in the cases of interest, to grid a spacing of 100 m which is clearly insufficient to resolve the NBL. In attempting to focus on the most basic issues that will be common to almost every type of NBL, we have found it nonetheless necessary to include a minimal land-surface model (LSM) as a lower boundary condition. Early experiments using prescribed surface fluxes, or even a prescribed surface temperature (tendency) proved to prevent the ABL from responding to surface biases, and vice-versa. The response introduced by the LSM can potentially enhance biases, but has also proven to decrease the inter-model spread of results (Holtslag et al., 2007). Furthermore, the use of prescribed fluxes can lead to inconsistencies in the surface layer parameterization in the NBL (Basu et al., 2008a).

The remainder of this chapter is organized as follows: Section 3.2 presents an analysis of the measurement data. In Section 3.3 the LES code is briefly introduced, together with a description of the case setup. Our main findings are presented in Section 3.4, first in terms of the general characteristics of the experiments, followed by the results of the sensitivity study on resolution. Finally, the results are summarized in Section 3.5.

## 3.2 Characteristics of the clear summertime NBL

To setup the numerical experiments, we first obtain relevant NBL characteristics from measurements. This allows us to design a number of experiments that cover the characteristics of the desired study area. The analysis is based on 12 years of data (1 January 2001 to 12 December 2012) from two meteorological sites in Western Europe: the Hamburg weather mast operated by the University of Hamburg, Germany, and the Cabauw Experimental Site for Atmospheric Research (CESAR) in Cabauw, the Netherlands. The Hamburg site is located in the easterly outskirts of Hamburg (53.52°N, 10.10°E) and characterized by flat but inhomogeneous surroundings comprising a mix of industrial buildings and community gardens, with rural terrain towards the east (Brümmer et al., 2012). The Cabauw site (51.97°N, 4.93°E) is surrounded by flat terrain and open pasture in all directions, with some low buildings at 400-600 m distance towards the north and east (Van Ulden and Wieringa, 1996). See Appendix A.5 for additional details about the sites.

Because of the present study's focus on daytime convection, we limit the analysis to clear nights during the May to August period (see Appendix A.1 for details and a validation of the sampling procedure). We focus the analysis on two key features that govern the characteristics of the NBL: wind (shear production of turbulence) and surface cooling (buoyancy suppression as the atmosphere becomes stably stratified).

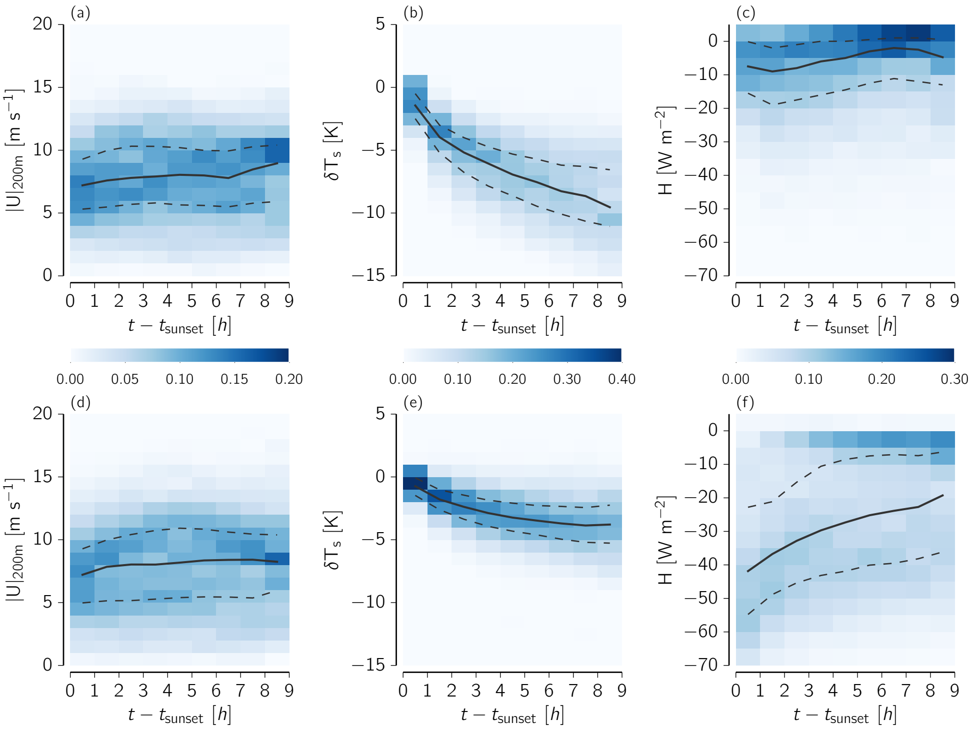

*Figure 3.1: 2D Histograms (a-c: Hamburg, d-f: Cabauw) for the absolute wind speed at 200 m height ($|U|_{200\text{m}}$, left column), change in surface temperature since sunset ($\delta T_s$, middle column) and surface sensible heat flux (H, right column). For each variable, both stations share the color bar. All samples are binned in hourly intervals, and the resulting histograms are normalized per bin (i.e. the total probability per hourly bin equals 1). The dashed lines indicate the 25th and 75th percentile, the solid line the median.*

Wind speeds are obtained from tower measurements at 200 m height (direct measurement for Cabauw, interpolated between 175 m - 250 m for Hamburg), and will be used as a proxy for the geostrophic wind. For surface cooling two measures are used: the surface (skin) temperature obtained from IR-radiometers, and near-surface turbulent heat fluxes obtained from sonic anemometers (5 m height at Cabauw, 10 m height at Hamburg). For all variables we examine the time development since sunset. Although the NBL development (negative surface flux) usually begins before sunset, this provides a simple robust and objective way to temporally align the data.

The statistics from both stations show typical characteristics of the NBL, with a strong decrease in surface temperature and negative surface fluxes. The results are summarized in Fig. 3.1. For each variable its time development is summarized by means of 2D-histograms, with the probability binned over one hour intervals since sunset (t = 0 h), and each individual hourly bin normalized to unity. For surface cooling, the temperature at sunset is subtracted from the samples to obtain the net cooling over the night. In all panels the dashed and solid lines indicate the 25th (P1), 50th (P2) and 75th (P3) percentiles. The 200 m wind speed (Fig. 3.1a,d) is relatively similar for both stations — average wind speeds are ~7.5 m s$^{-1}$, where ~75% of the samples have a wind speed higher than 5 m s$^{-1}$. Both station experience a light increase in wind speed during the night, which most likely represents the formation of a low-level jet, and is most evident at Cabauw. In contrast with the relatively similar wind speeds, the surface cooling rate (Fig. 3.1 b,e) and sensible heat flux (Fig. 3.1c,f) differ more between the two stations. The total surface cooling at 9 hours after sunset is approximately 9 K in Hamburg, which is 5 K more than in Cabauw, while the sensible heat flux in Cabauw is significantly more negative. A possible explanation for these differences might lie in the difference in near surface wind speed (not shown), which is lower in Hamburg, likely due to its more sheltered location. However, these interpretations should be tempered by the realization that the fluxes are measured at different heights (decreasing heat flux with height), and that there are known difficulties in flux measurements in the NBL (surface energy balance closure, e.g. de Roode et al. (2010)).

Based on these findings, the numerical experiments will aim at covering the typical conditions (P1-P3 as a guideline) with wind speeds in the range of 5 m s$^{-1}$ - 10 m s$^{-1}$ and surface heat fluxes of approximately -30 W m$^{-2}$ to -40 W m$^{-2}$. Further details of the experimental set up are provided in section 3.3.2.

## 3.3 Setup

### 3.3.1 Large-eddy simulation code

The University of California, Los Angeles large-eddy simulation (UCLA-LES v4.0) code was used for the numerical experiments in this study, which is described in Chapter 2. Based on a validation (not shown) for the GABLS1 LES intercomparison (Beare et al., 2006), a few minor adjustments were made: the addition of a fourth-order centered advection scheme for scalars (Wicker and Skamarock, 2002), and the Smagorinsky constant ($C_s$) was reduced from 0.23, its default value in UCLA-LES, to 0.17. In addition to these adjustments, we added a minimal land-surface model (LSM) that allows for a response of the surface temperature and turbulent fluxes to biases in the atmosphere, and vice versa. The LSM is based on the ECMWF (2011) documentation, and described in Appendix A.3. Although radiative cooling of the NBL can be significant (especially near the surface and NBL top), its influence on the mean thermodynamic structure is typically small (Garratt and Brost, 1981). Therefore, we follow previous work on idealized NBL experiments (e.g. Beare et al., 2006; Basu et al., 2008b; Kosovic and Curry, 2000), exclude the influence of radiation on the atmosphere, and use a simplified representation for radiation which only drives the LSM. The incoming longwave radiation is set constant in time, and its outgoing component is based on the surface temperature and Stefan-Boltzmann's law. The incoming shortwave radiation is prescribed, using a fixed surface albedo to calculate the outgoing radiation. See Appendix A.3 for details.

### 3.3.2 Case description

The findings of section 3.2 informed the design of the numerical experiments, which we here describe. All cases cover a near complete diel cycle (21 hours), running from the late afternoon, throughout the night, into the second day with dry convection. The model is initiated with a 500 m deep well-mixed layer of potential temperature $\theta = 290$ K, with a constant temperature stratification of 6 K km$^{-1}$ above. The diurnal variability is introduced by the parameterized radiation and LSM (Appendix A.3). In the late afternoon (start of the experiment), solar heating drives convection and growth of the CBL. When the net surface radiation ($Q_{\mathrm{net}}$) becomes negative, surface cooling and the development of the NBL is initiated. In time the NBL deepens as the cool surface air is mixed upwards by turbulent eddies, whose intensity is partially regulated by wind shear. Based on the findings of section 3.2, we initially consider two experiments in which only the geostrophic wind is varied from 5 m s$^{-1}$ to 10 m s$^{-1}$ (Table 3.1). As shown in Section 3.2, the lower threshold of 5 m s$^{-1}$ ensures that we cover approximately 75% of the typical Western European conditions. In addition to wind shear, the surface cooling rate determines the turbulent intensity as it drives the formation of the stable layer, which suppresses (vertical) turbulent motions. Although the inclusion of the LSM obstructs us from directly controlling the surface cooling, we can manipulate the cooling rate through the surface characteristics in the following way: By decreasing the thermal diffusivity of the skin layer ($\Lambda_{\mathrm{sk}}$, eq. A.3) the interaction between the surface and soil is decreased, increasing the atmospheric cooling rate at night (experiment $U_{8L}$). After sunrise the surface is heated again, a shallow CBL forms in the stable layer, until convection grows into the residual layer of the previous day of convection. Note that in the absence of large scale forcings (advection, subsidence) and radiation, there is no process stabilizing the residual layer after the onset of the NBL.

*Table 3.1: Overview of the three different (physical) LES experiments, varying the geostrophic wind ($U_g$) and diffusivity of the skin layer ($\Lambda_{sk}$, Eq. A.3). The domain is oriented such that the geostrophic wind is in the x-direction, the v-component is set to zero.*

| Exp | $U_g$ [ms$^{-1}$] | $\Lambda_{sk}$ [Wm$^{-2}$K$^{-1}$] |
|---|---|---|
| $U_{10}$ | 10 | 10 |
| $U_5$ | 5 | " |
| $U_{8L}$ | 8 | 1 |

Combined, the variation in geostrophic wind and surface cooling rate results in three physical experiments, summarized in Table 3.1. For each physical experiment sensitivity studies on resolution are performed. All cases fix the domain size to $L_x$ = $L_y$ = 3200 m, $L_z$ = 2000 m, in which the grid spacing is varied from $\Delta_{xy}$ = $\Delta_z$ = 3.125 m to $\Delta_{xy}$ = 100 m, $\Delta_z$ = 25 m (Table 3.2). Throughout the text, the combination of physical experiment - resolution experiment is referred to as e.g. $U_{10} - \Delta_3$ for the 10 $m\ s^{-1}$ case with a grid spacing of 3.125 m. Except for the variation in grid spacing, the resolution experiments share the exact same setup — no tuning of (for example) parameters in the SGS model is performed. However, to verify the validity of the $U_5$ and $U_{8L}$ experiments, two additional runs were performed for a part of the NBL period with a decreased Smagorinsky constant (case name appended with Cs). All horizontal velocities are initiated with their geostrophic value, constant with height. Temperature perturbations are applied to the initial mixed-layer to break the horizontal slab symmetry. Although sufficiently turbulent LES is stochastic (e.g. Sullivan and Patton, 2011), the averaging time and domain size provide sufficient sampling so that the statistics are robust, and not influenced by differences among realizations. At the top of the domain, a 200 m deep damping layer (with a time scale linearly increasing from $\tau$ = 0 s at 1800 m to $\tau$ = 300 s at 2000 m) is added to prevent the reflection of gravity waves. The surface pressure is set to $10^5$ Pa, and the base state potential temperature to 296 K.

## 3.4 Results

### 3.4.1 General characteristics of the experiments

We first present the general characteristics of the different experiments from the three high-resolution reference cases ($U_{10}-\Delta_3$, $U_5-\Delta_3$, $U_{8L}-\Delta_3$, Table 3.2). In addition, the

*Table 3.2: Resolution experiment. All experiments fix the horizontal domain size to 3200 m, the vertical size to 2000 m*

| Exp | $N_{xy}$ [-] | $N_z$ [-] | $\Delta_{xy}$ [m] | $\Delta_z$ [m] | $C_s$ |
|---|---|---|---|---|---|
| $\Delta_3$ (reference) | 1024 | 640 | 3.125 | 3.125 | 0.17 |
| $\Delta_3 - \mathrm{Cs}$ | " | " | " | " | 0.10 |
| $\Delta_6$ | 512 | 320 | 6.25 | 6.25 | 0.17 |
| $\Delta_{12}$ | 256 | 160 | 12.5 | 12.5 | " |
| $\Delta_{25}$ | 128 | 80 | 25 | 25 | " |
| $\Delta_{50}$ | 64 | " | 50 | " | " |
| $\Delta_{100}$ | 32 | " | 100 | " | " |

validity of the reference cases will be addressed. Figures 3.2 and 3.3 show the temporal evolution of four key atmospheric and surface properties: the ABL depth ($z_{\mathrm{ABL}}$) in Fig. 3.2, and the 10 m and 200 m wind speed ($|U|$), surface sensible heat flux ($H$) and the surface temperature ($T_s$) in Fig. 3.3.

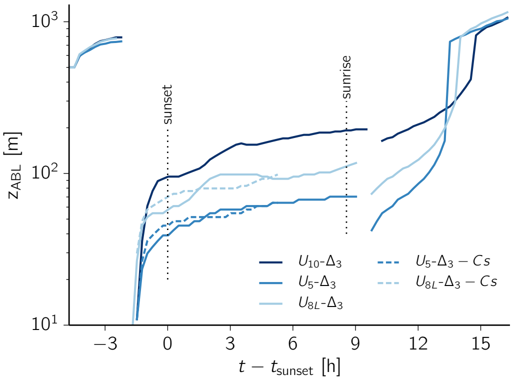

*Figure 3.2: Temporal evolution of the ABL depth ($z_{\mathrm{ABL}}$) in the three reference cases ($U_{10}$-$\Delta_3$, $U_5$-$\Delta_3$, $U_{8L}$-$\Delta_3$) and the two sensitivity experiments on the Smagorinsky constant ($U_5$-$\Delta_3$-$Cs$, $U_{8L}$-$\Delta_3$-$Cs$) As explained in the text, different ABL-depth definitions for convective and stable conditions are used, resulting in two discontinuities before and after sunset.*

The 200 m wind speed, surface temperature and surface heat flux in Fig. 3.3 allows for a comparison with the measurement data presented in Fig. 3.1. Note that we do not attempt to validate the model in detail, which would require specific measurements that we do not have access to, but rather compare the experiments with measurement statistics to ensure that our idealized study addresses a relevant part of the parameter space. Two different definitions of the ABL depth are used. For con-

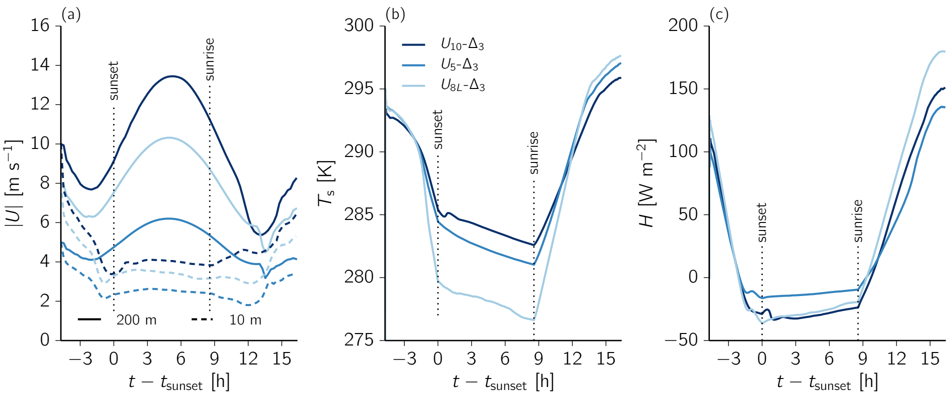

*Figure 3.3: Temporal evolution of the absolute wind speed* $|U| = \sqrt{u^2 + v^2}$ *at 10 m and 200 m height (a), surface sensible heat flux H (b) and surface (skin) temperature* $T_s$ *(c) in the* $U_{10}$*-*$\Delta_3$*,* $U_5$*-*$\Delta_3$*,* $U_{8L}$*-*$\Delta_3$ *experiments.*

vective conditions ($H > 0$), the ABL depth is defined as the height of the minimum turbulent heat flux. For stable conditions ($H < 0$), the ABL depth is defined as the first height at which the ABL temperature is within 0.25 K of the last temperature profile when $H$ was last larger than zero. In other words, this is the layer depth which is influenced by surface cooling. The definition for stable conditions differs from typical definitions based on the momentum flux or a critical Richardson number (e.g. Beare et al., 2006; Richardson et al., 2013), as both methods have proven to be imprecise for our experiments because of decaying turbulence in the residual layer.

Although the surface temperature (Fig. 3.3b) decreases over the first few hours before sunset, the surface sensible heat flux (Fig. 3.3c) remains positive resulting in convection and growth of the mixed-layer up to approximately 800 m height. From case $U_5 - \Delta_3$ to $U_{10} - \Delta_3$ the mixed-layer slightly deepens; because of small differences in $H$ and potentially by shear driven growth of the mixed-layer (Pino et al., 2003). Approximately one hour before sunset $T_s$ begins to decrease rapidly and $Q_{\mathrm{net}}$ becomes negative, marking the onset of the NBL. A shallow internal boundary layer develops as the thermally driven mixing shuts down, and the NBL deepens in time as cool air from the surface is mixed upwards, where the mixing depth is determined by the intensity of the turbulent eddies. The NBL in the $U_{10}$ case grows to approximately 200 m depth at sunrise. For weaker winds, or less conductive surfaces with stronger surface cooling, the NBL is about half as deep. As observed in the measurement data (Fig. 3.1a,d), the wind speed aloft increases over the NBL period and becomes super-geostrophic (low-level jet). Night time 200 m wind speeds are in between 4 m s$^{-1}$ - 14 m s$^{-1}$, in line with the analysis for Cabauw/Hamburg. After the rapid decrease in surface temperature shortly before sunset, the cooling rates moderate and remain approximately constant during the night. All cases have their total surface cooling in between 2.9 K and 3.4 K, less than observed in the measurement data. However, the resulting surface sensible heat flux ($H$) is in between -10 W m$^{-2}$ and -40 W m$^{-2}$, which agrees, in both magnitude and tendency, with the findings in Fig. 3.1c and f. Despite the simplicity with which the land-surface processes are represented and the idealizations in the set up, the LES cases cover the typical conditions presented in Fig. 3.1, with realistic features in both the CBL and NBL.

To address the validity of the reference ($\Delta_3$) cases during the NBL period, we show in Fig. 3.4 the fraction resolved/total heat flux as a function of the normalized ABL depth (at $t$ = 10 h or $t - t_{\mathrm{sunset}} \approx 5.5$ h).

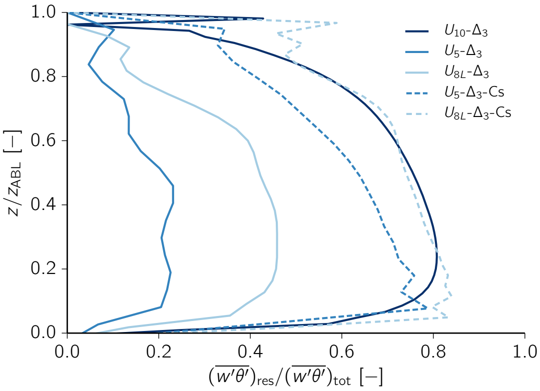

*Figure 3.4: Fraction of resolved/total heat flux in the NBL (t=10 h) for all $\Delta_3$ cases. For the 5 m s$^{-1}$ and 8 m s$^{-1}$ cases the sensitivity on the Smagorinsky constant ($C_s$) is shown.*

With a 3 m grid spacing, about 75% of the turbulent heat flux is resolved in the $U_{10}$ case. This ensures that the NBL development is primarily driven by resolved turbulence, and that the contribution of the SGS model is limited. Despite the high resolution, this requirement is more difficult to fulfill for the $U_5$ and $U_{8\mathrm{L}}$ cases which resolve approximately 20% and 40%, respectively. More care must be applied in adopting the $\Delta_3$ as a reference case in this situation. However, based on the $U_{10}$ sensitivities it is possible to sensibly interpret the effect of sub-optimal resolutions in these cases, even when the reference case is not fully resolved. However, to test such interferences, Fig. 3.4 shows two additional experiments (case name appended with Cs) for the NBL period in which the Smagorinsky constant was reduced from $C_s$ = 0.17 to 0.10. This produces a better resolved turbulent field, less influenced by uncertainties related to the SGS closure. Compared to their counterparts with the reduced Smagorinsky con-

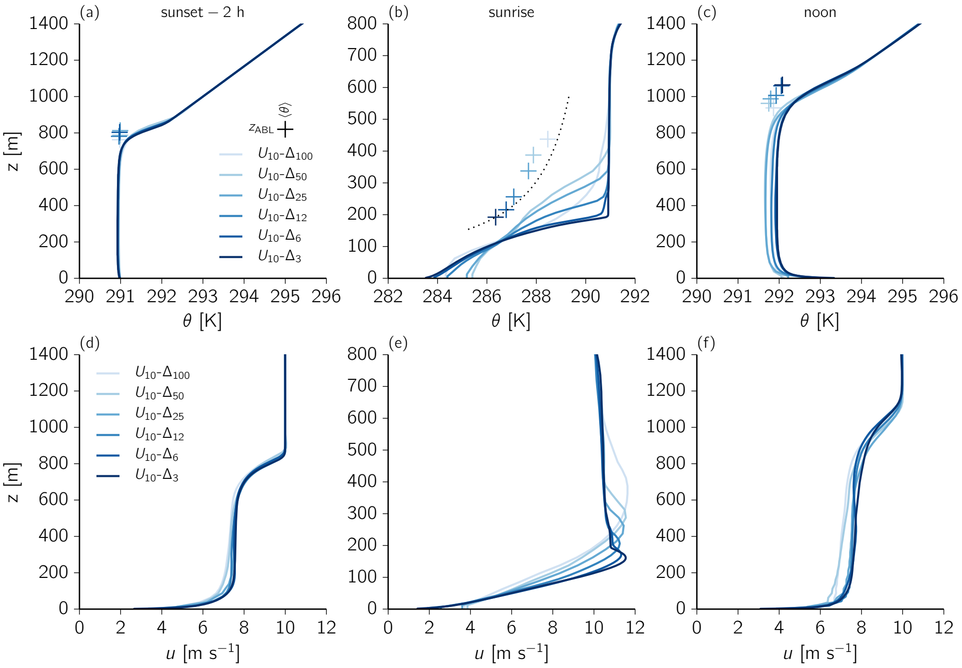

*Figure 3.5: Vertical profiles at sunset minus two hours (2.75 h), sunrise (13.25 h) and noon (21 h) for case $U_{10}$. Top: Potential temperature ($\theta$), bottom: Zonal wind component ($u$). The markers in the top panels indicate the ABL from a bulk perspective, i.e. the height of the ABL ($z_{\mathrm{ABL}}$), and average temperature over that layer ($\langle\theta\rangle$).*

stant, the average NBL depth of the $U_5$ and $U_{8\mathrm{L}}$ cases is off by less than 7% (Fig. 3.2), which indicates that the poor resolution of the reference case is not unduly influencing our experimental setup.

### 3.4.2 Case $U_{10}$: sensitivity on resolution

To study the influence of resolution in this section we present the results from a sequence of simulations in which the resolution is degraded systematically. The resolution is coarsened by factors of two from $\Delta_{xy} = \Delta_z = 3.125$ m to $\Delta_{xy} = 100$ m, $\Delta_z = 25$ m (Table 3.2) to study (a) how well the NBL is represented at relatively coarse resolutions, and (b) whether biases in the NBL influence the development of convection on the second day. We start with a more detailed analysis of the $U_{10}$ case as it most clearly illustrates the temporal evolution of the cases and their dependence on resolution. Next, the other cases are addressed by studying the ABL biases for both CBL periods and the NBL in the next subsection.

Our analysis focuses on the vertical profiles of potential temperature ($\theta$) and zonal wind ($u$) at three distinct periods: two hours before sunset as the surface sensible heat flux becomes negative, sunrise as the NBL has fully developed, and end of the experiment (noon). The results are shown in Fig. 3.5. The markers in the top panels indicate the ABL structure from a bulk perspective, i.e. the height of the ABL ($z_{\mathrm{ABL}}$), and average temperature over that layer ($\langle\theta\rangle$).

**Late afternoon decay:**

Over the first hours of convection (Fig 3.5a,d), the results are relatively insensitive to the large difference in grid spacing. Maximum biases in $z_{\mathrm{ABL}}$ and $\langle\theta\rangle$ are less than 0.1 K and 30 m respectively, in line with the findings (first-order moments) of Sullivan and Patton (2011). The velocity profiles are more sensitive, with a small underestimation of the lower-ABL velocity in the low-resolution experiments. This is caused by a small overestimation of the surface friction velocity, and/or the reduced amount of resolved turbulence, causing more difficulties in maintaining the well-mixed profile. Nonetheless, the resulting biases are small, which is beneficial for our study as it shows that the CBL development itself is insensitive to the range of grid spacings, allowing all cases to enter the NBL phase with similar conditions.

**NBL period**:

During the NBL period (Fig 3.5b,e) the mean profiles show a greater sensitivity to grid spacing as the more poorly resolved simulations mix through a deeper layer. With increasing grid spacing less turbulence is resolved (percentage resolved/total flux), decreasing from ~70% - 80% in case $\Delta_3$ to ~10% in case $\Delta_{25}$ ($t = 10$ h or $t - t_{\mathrm{sunset}} \approx 5.5$ h, at $z = 0.5 z_{\mathrm{ABL}}$), the yet coarser resolution experiments ($\Delta_{50}$, $\Delta_{100}$) are nearly laminar. Even though this produces invalid LES (no turbulent mixing; “no-eddy simulation”), there is still diffusive transport by the SGS model. The strain rate—predominantly determined by the vertical shear component of $\widetilde{S}_{ij}$ (Eq. 2.12) —is fairly constant (Fig. 3.5e). Therefore, with similar strain rate and increasing grid spacing, sub-grid diffusion increases which causes the deepening of the NBL. Amongst other possibilities, the use of a shear-improved Smagorinsky scheme (Lévêque et al., 2007) or a more appropriate choice of the sub-grid length scale $C_{\mathrm{s}}\Delta$, might improve this undesirable behavior of the SGS model and help it transition to a more standard RANS closure in the absence of a resolved turbulent flow.

The difference in NBL structure is not only caused by the dynamics and/or the SGS model, as in such a case (identical surface heat fluxes) the biases would solely consist of a different redistribution of the cooled air with height. Indicated within Fig. 3.5b (dotted line) is the theoretical NBL structure (bulk temperature/height) that would arise if the total NBL cooling of the $\Delta_3$ case was simply distributed over a different NBL depth. For example: compared to the residual layer temperature of 291 K, the $\Delta_3$-case has cooled 5 K ($\langle\theta\rangle \approx 286$ K) over a 200 m deep layer. Mixing the same cooling over a layer of 400 m depth would theoretically result in 2.5 degrees NBL cooling, or $\langle\theta\rangle \approx 288.5$ K. Compared to the reference case, all lower resolution experiments are relatively cold (i.e., situated left of the dotted line), which is the result of the interactive LSM. Shown in Fig. 3.6 is the bias in the surface sensible heat flux compared to the reference case ($\delta H = H_x - H_{\Delta 3}$, with $H_x$ the different $U_{10}$ cases). Approximately one hour before sunset, the lower resolution cases start producing more negative surface fluxes. This is the result of an increased temperature difference between the surface and lowest model level, which is partially compensated by an increase in aerodynamic resistance (Eq. A.2).

**Second day of convection**:

Despite the large biases that are introduced during the NBL period, the different resolution experiments tend to re-align during the second day of convection (Fig. 3.5c,f). As a result of the additional surface cooling at night (Fig. 3.6), the ABL depth and temperature at the end of the experiments (noon) is lower for the lower resolution cases, with maximum biases in the mixed-layer depth of ~100 m, and averaged mixed-layer temperature of ~0.35 K. Note that the temperature bias is amplified by the difference in mixed-layer growth, influencing the entrainment of relatively warm free tropospheric air as the mixed-layer deepens. The LSM partially compensates these biases as the surface sensible heat flux increases with decreasing resolution (Fig. 3.6).

A back of the envelope calculation helps to put these results in perspective: For example, the nighttime bias $\delta H$ for case $\Delta_{50}$ is around -12 $\mathrm{W\,m^{-1}}$ over a period of approximately 12 hours (Fig. 3.6). With $\delta H$ integrated in time, and distributed over the average afternoon mixed-layer depth of 1000 m, this results in a temperature bias of -0.44 K. A similar calculation for the daytime bias ($\delta H \approx 7\ \mathrm{W\,m^{-2}}$ over approximately 5 hours) reveals a temperature compensation of 0.1 K, indicating that about 25% of the nighttime bias is compensated. As the difference in $H$ remains positive for the low-resolution cases at the end of the experiment, the biases in ABL depth and temperature would further decrease if the experiments were further integrated in

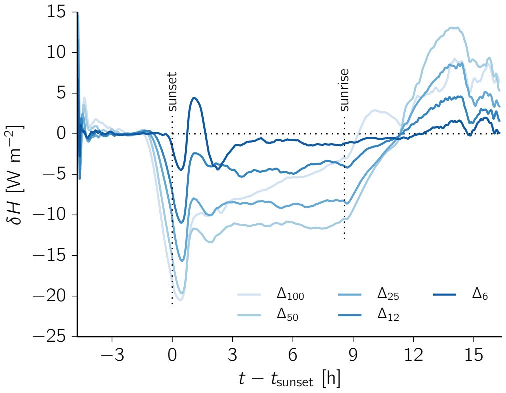

*Figure 3.6: Bias in the surface sensible heat flux for case $U_{10}$, compared to the $U_{10}$-$\Delta_3$ case ($\delta H = H_{\Delta_X} - H_{\Delta_3}$).*

time. The partial bias cancellation is not serendipitous, but the result of energy conservation within our experiments where the additional heat entering the soil at night is again released during the day. In section 3.4.4 the implication of these biases on convection is discussed in more detail.

Summarized, the experiments are insensitive to the large range of grid spacings during the first day of convection. During the NBL phase the structure of the NBL is influenced by both the ratio of resolved/modeled mixing, and differences in the surface sensible heat flux as the LSM responds to ABL biases, and vice-versa. Despite the large NBL biases, all cases tend to re-align during the second day of convection.

### 3.4.3 Statistics of the $U_5$, $U_{8L}$ and $U_{10}$ cases

For all cases, the biases in ABL depth ($\delta z_{\mathrm{ABL}}$) and ABL averaged potential temperature ($\delta\langle\theta\rangle$) are here presented in condensed form (Fig. 3.7). We focus on the same three periods as in the previous section: (i) two hours before sunset, (ii) sunrise and (iii) noon during the second day of convection. The biases are calculated compared to the reference ($\Delta_3$) experiments, and all statistics are averaged over the sixty minute period before the indicated time.

The results are shown in Fig. 3.7. All three physical experiments exhibit similar behavior. Two hours before sunset ($t = i$) the ABL depth is (on average) slightly underestimated in the lower resolution experiments, although there is no clear trend as a function of resolution. For all cases, the absolute biases in bulk potential temperature are $\ll$0.1 K. During the NBL period the lower resolution experiments create deeper NBLs. The maximum bias at sunrise ($t = ii$) in $z_{\mathrm{ABL}}$ increases with higher wind

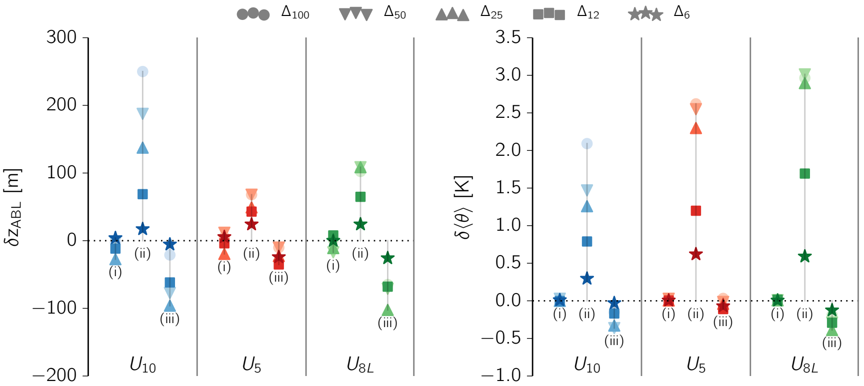

*Figure 3.7: Biases in ABL depth ($\delta z_{\mathrm{ABL}}$) and ABL averaged temperature ($\delta\langle\theta\rangle$) at sunset minus two hours (i, 2.75 h), sunrise (ii, 13.25 h) and noon (iii, 21 h). All statistics are averaged over one hour (t=1.75-2.75 h, t=12.25-13.25 h, t=20-21 h).*

speeds from ~80 m in the $U_5$ case to ~250 m for case $U_{10}$. The relative biases are, however, approximately constant, with the $\Delta_{100}$ cases overestimating the NBL depth by 100% - 120% compared to the $\Delta_3$ setup. The bulk potential temperature is overestimated in all sensitivity experiments. Although the lower resolution experiments experience more negative surface heat fluxes (Fig. 3.6 for case $U_{10}$), the NBL-averaged temperature decreases less as the surface cooling is distributed over a deeper layer. The absolute biases at sunrise ($t = ii$) range from 2 K in case $U_{10}$ to 3 K in case $U_{8\mathrm{L}}$. At noon during the second day of convection ($t = iii$) the biases in ABL-depth are opposite in sign of the biases during the NBL period. The $U_{8\mathrm{L}}$ and $U_{10}$ cases have the largest underestimation of approximately 100 m. The relatively large bias in $\langle\theta\rangle$ decreases as the mixed-layer grows to less than 0.5 K.

Summarized, the misrepresentation of the NBL results in biases in ABL depth and temperature on the order of 100 m and 0.5 K. In the following section, the implications of such biases on cloud formation will be briefly discussed.

### 3.4.4 Implications for cloud formation

Up to this point, the biases during the second day of convection have been addressed individually for the ABL depth and temperature. More relevant for moist convection is their contribution to a quantity related to clouds: the mixed-layer top relative humidity ($RH_{z_{\mathrm{ABL}}}$). Even though our experiments exclude moisture, we can quantify the temperature contribution to relative humidity biases. These arise both from the effect of mixed-layer temperature biases directly, but also because of an over or under-estimation of the mixed-layer depth, influencing the absolute temperature at the mixed-layer top. This thus excludes the influence of ABL dynamics (and biases) on moisture, and only acts to place the biases in mixed-layer temperature and depth in context of $RH_{z_{\mathrm{ABL}}}$.

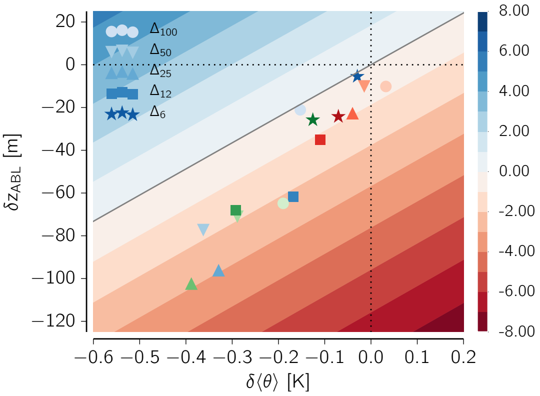

*Figure 3.8: Influence of biases in ABL depth ($\delta z_{\mathrm{ABL}}$) and temperature $\delta\langle\theta\rangle$ on the mixed-layer top relative humidity (%). Given a bias in $z_{\mathrm{ABL}}$ and $\langle\theta\rangle$, the shaded contours indicate the difference in $RH_{z_{\mathrm{ABL}}}$ compared to a 1000 m deep ABL with $\langle\theta\rangle$ = 290 K and $RH_{z_{\mathrm{ABL}}}$ = 100%. The colors of the individual experiments are the same as in Fig. 3.7.*

Fig. 3.8 shows the results of this analysis. The error in $RH_{z_{\mathrm{ABL}}}$ (shaded contours) is here calculated as the combined influence of $\delta z_{\mathrm{ABL}}$ and $\delta\langle\theta\rangle$ on $RH_{z_{\mathrm{ABL}}}$, compared to the reference cases ($\Delta_3$). For the reference case a reference moisture mixing ratio ($r_{\mathrm{ref}}$) is calculated, such that $RH_{z_{\mathrm{ABL}}}$ is equal to 100%, i.e. $z_{\mathrm{ABL}}$ equals the lifting condensation level. Assuming that $r_{\mathrm{ref}}$ is constant amongst the lower-resolution experiments, the bias in mixed-layer potential temperature (directly influencing $T_{z_{\mathrm{ABL}}}$) and depth (influencing $T_{z_{\mathrm{ABL}}}$ through its dependence on the mixed-layer top pressure) is translated to a bias in $RH_{z_{\mathrm{ABL}}}$.

For all cases except one, the biases in $z_{\mathrm{ABL}}$ and $\delta\langle\theta\rangle$ are of similar sign: an underestimation of $z_{\mathrm{ABL}}$ is coupled to an underestimation of $\langle\theta\rangle$. As the reference cases ($\delta z_{\mathrm{ABL}} = \delta\langle\theta\rangle = 0$) are assumed to have a mixed-layer top relative humidity of 100%, their mixed-layer depth corresponds to the height of the lifting condensation level ($z_{\mathrm{LCL}}$). Therefore, for a constant relative humidity, $\delta z_{\mathrm{ABL}}$ corresponds to the change in $z_{\mathrm{LCL}}$ as a function of $\delta\langle\theta\rangle$. This allows the comparison of both the change in $RH_{z_{\mathrm{ABL}}}$ and $z_{\mathrm{LCL}} - z_{\mathrm{ABL}}$ from Fig. 3.8.

As shown, the biases in mixed-layer depth and temperature partially compensate. The maximum temperature biases of -0.4 K would result in an increase in relative humidity of 2-3% or change in $z_{\mathrm{LCL}}$ of -50 m, which is compensated by the negative bias in mixed-layer depth. The resulting change in $RH_{z_{\mathrm{ABL}}}$ is in the range of 0% to -3%, and the difference $z_{\mathrm{LCL}} - z_{\mathrm{ABL}}$ is on the order of 0 m to -50 m. For comparison: these differences are on the order of the inter-model spread (cloud base relative humidity, and cloud base height) of different LES codes for experiments of the daytime ABL only (ARM LES intercomparison, Brown et al., 2002).

## 3.5 Summary and conclusions

In the present study we analyzed the influence of misrepresenting the NBL in low-resolution LES on the subsequent day of dry convection. Here, low-resolution was defined as a grid spacing sufficient to explicitly represent daytime convection, but much coarser than needed to resolve small scale turbulence in the NBL. With the high requirements on grid spacing for the NBL period, such a setup might be necessary or beneficial for studies that primarily address daytime convection, or early initiatives to explore the use of LES for NWP purposes. We answered the question: how accurately must the NBL be represented in order to obtain a faithful representation of daytime convection?

Using statistics obtained from measurement data representative for summertime Western European conditions, we designed idealized LES experiments covering near complete diel cycles of convection over land. Reproducing the typically observed conditions ensured that we covered realistic conditions in terms of wind (shear, producing turbulence) and surface cooling (buoyancy suppression of turbulence). With a sensitivity study on resolution, ranging the (horizontal) grid spacing from 3.125 m to 100 m in factors of two, we addressed the role of the fraction of resolved turbulence on the development of the NBL, and implication of NBL biases on the consecutive day of dry convection. The roles of moisture and radiation were excluded from the experiments; if a relatively simple dry case is poorly represented, then more complex cases involving moist convection will surely be influenced.

From the results of our numerical experiments we can draw a number of conclusions. As expected, the rate of resolved turbulence in the NBL quickly decreases with increasing grid spacing. At grid spacings as coarse as 100 m, no NBL turbulence is resolved and the NBL development is predominantly driven by the SGS model. Under these conditions, the NBL is poorly represented with relative biases in the NBL depth of 100% - 120%, and absolute biases in the bulk NBL temperature of 2 K - 3 K. These biases are the result of both the SGS model, causing excessive vertical mixing at low resolutions, and feedbacks between the LSM and the atmosphere. The latter allows for a more realistic response of surface processes to (biases in) the atmosphere, relaxing the strict coupling that would be introduced with the use of a prescribed surface temperature or flux. Despite the large biases in the NBL, the influence on the consecutive day of convection is limited: maximum biases in the afternoon mixed-layer depth and temperature are approximately 100 m and 0.5 K, respectively. As these biases are positively correlated — an underestimation of the NBL depth corresponds to an underestimation of the ABL temperature — the biases compete and partially compensate their individual influence on the mixed-layer top relative humidity, resulting in maximum differences of 0% to -3%. This insensitivity of the relative humidity is important for correctly timing the onset of moist convection, as a precursor for deeper moist convection and precipitation. The authors remind the reader that our simulations excluded moisture and therefore only provides a first order estimate, neglecting the influence of potential biases in the moisture mixing ratio.

For applications focussed on daytime convection, in which biases during the NBL period are tolerable, these findings are promising. The use of relatively coarse resolutions greatly decreases the required computational resources, opening the opportunity for employing LES to study the diurnal cycle of convection at meso-alpha scales (20 km - 2000 km). However, our study only addressed the dynamical aspects in the absence of moisture and radiation. Whether moisture (fog) and radiation can, in particular cases, further amplify the NBL biases and/or daytime convection is studied in the next chapter. Also, our study predominantly focussed on the mean thermodynamic structure of the ABL. A more detailed analysis of the influence of grid spacing on (shallow) convection, similar to Sullivan and Patton (2011) and extending the work of Bryan et al. (2003), would be interesting.

# Chapter IV

# Observational and conceptual modeling analysis on the impact of model biases on nocturnal low clouds

The impact of model biases in the nocturnal boundary layer (NBL) on the formation of fog or low clouds is studied using both observations and a newly developed conceptual model. The observations (from Hamburg, Cabauw and Karlsruhe) allow for a characterization of the typical northwest European nighttime conditions, which indicate that (1) nights in between convective days are fairly moist with high relative humidities near the surface, (2) from these sites, only Cabauw frequently experiences saturated conditions near the surface, and (3) the dew point depression higher up (200 m height) is often less than 2 K. The possibility whether this low dew point depression, combined with model biases, might result in a spurious formation of low clouds is further explored using a newly developed conceptual model, where the results provide clear evidence that this is unlikely to happen.

## 4.1 Introduction

Large-eddy simulation – traditionally used to study highly idealized conditions – is slowly moving towards more realistic experiments, for example running LES continuously (days to years) to validate or develop convective parameterization schemes (Neggers et al., 2012) or study long-term statistics of turbulent flows (Schalkwijk et al., 2015a). In addition, LES has recently been used to perform weather hindcasts on domains as large as hundreds of kilometers (Schalkwijk et al., 2015b) to roughly a thousand kilometer, as currently being performed with the LES-capable version of ICON (*Icosahedral non-hydrostatic general circulation model*, Dipankar et al., 2015) within the *High-Definition Clouds and Precipitation for Advancing Climate Prediction* (HD[CP]$^2$) project.

With the traditional LES experiments (e.g. Deardorff, 1970; Moeng, 1984; Bechtold et al., 1996; Stevens et al., 2001; Brown et al., 2002; Siebesma et al., 2003; Stevens et al., 2005; Beare et al., 2006; Ackerman et al., 2009; Vanzanten et al., 2011), the domain size and resolution is typically optimized for the process being studied. This results in a variety of LES setups, with grid spacings ranging from meters (or less) for studies of stable boundary layers (e.g. Beare et al., 2006), to grid spacings of hundreds of meters for studies of deep convection (e.g. Hohenegger and Stevens, 2013; Schlemmer and Hohenegger, 2015), and domain sizes ranging from hundreds of meters to hundreds of kilometers. In contrast to these idealized cases, the more realistic LES experiments (which aim at covering full diel cycles, and all the processes it encompasses) don't have this possibility, and should – at least in theory – have a grid spacing of $\mathcal{O}(1\ \mathrm{m})$ to capture the small nocturnal eddies, within a domain of $\mathcal{O}(100\ \mathrm{km})$ to allow for the development of the largest (deep convective) structures. As such a LES setup is clearly not feasible, often sacrifices are made, using a resolution which is sufficient to resolve daytime convection, but insufficient to resolve the much smaller nocturnal eddies.

In chapter 3 (van Stratum and Stevens, 2015) we demonstrated that in such a low-resolution LES setup (low-resolution with respect to the grid spacing required to resolve the small nocturnal eddies), the nocturnal boundary layer (NBL) is poorly represented, but that the nighttime biases have little impact on the following day of convection. However, our work only focussed on the fundamental principle behind LES: turbulent mixing. Any biases arising from incorrectly representing turbulent mixing (we will refer to this as a *primary bias*, as it should be the main skill of LES) have the potential to influence or offset other important processes (*secondary biases*), like radiation (e.g. Garratt and Brost, 1981; Duynkerke, 1999; Edwards, 2009) or thermodynamic processes. Especially the interaction between these two processes – the impact that liquid water (mist/fog or low clouds) can have on the incoming longwave radiation – has the potential to further modify the NBL development. In addition, if persistent nocturnal clouds or fog layers are formed that don't occur in reality, a reduction in the early morning incoming shortwave radiation can reduce the surface heating which drives the development of the convective boundary layer, potentially influencing the onset or intensity of convection. (Yin et al., 2015; Anber et al., 2015).

In this chapter we assess how likely the primary nocturnal model biases (the kind of biases reported in Chapter 3) can cause secondary biases in the formation of mist/fog or low clouds. Although we refer to biases in low-resolution LES, this work could also be relevant for models based on the Reynolds-averaged Navier-Stokes (RANS) equations, as many boundary layer parameterizations exhibit too much vertical mixing at night (e.g. Cuxart et al., 2006; Mauritsen et al., 2007; Holtslag et al., 2013). The result of overestimating vertical mixing, in both low-resolution LES and RANS models, typically causes a positive temperature bias near the surface, and a negative temperature bias near or above the NBL top (Fig. 4.1) – potentially causing an absence of fog occurring in reality, or a spurious formation of low clouds near/above the NBL top.

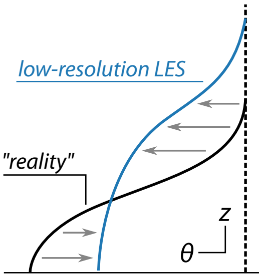

*Figure 4.1: Typical NBL bias in low-resolution LES*

We study how likely this is to happen using both observational data and a simple conceptual model. For the observations, data from Cabauw (Netherlands), Hamburg (Germany), and Karlsruhe (Germany) are used. All three sites have a relatively long data record (∼10-15 years), and with the available tower observations, we can study the NBL development both in space (height) and time. Like in the previous chapter, we are mostly concerned with the question whether nocturnal biases can influence the following day of convection. Therefore, the analysis is limited to the May through August period, and nights in between convective days. From the statistics of the observations, several questions can be answered, like how often the NBL saturates, where (near the surface or higher up), or how close the NBL gets to saturation. The latter can be important given the negative temperature biases near or above the NBL top (Fig. 4.1). These questions (and their answers) form the basis for the second part of this chapter.

In the second part we address whether the primary model biases can cause a spurious formation of low clouds. When introducing moisture, the parameter space of an LES setup increases greatly compared to a dry setup (as in Chapter 3), which complicates the design of a representative experiment, or set of experiments. For this reason we developed a conceptual model which – given the total nocturnal cooling (time integral of the surface heat flux over the nocturnal period) and the depth over which the cooled air is mixed – reproduces the vertical structure of the NBL. Several authors have constructed similar conceptual models, for both convective (see e.g. Stevens, 2006, for an overview) and stable (Stull, 1983a,b) conditions. We build on the work of Stull (1983a,b), but derive a modified vertical NBL structure from the LES experiments of Chapter 3, which is more representative for the cases that we are considering. Using the conceptual model we can study how the primary nocturnal biases (Fig. 4.1) influence the relative humidity for a wide range of conditions, using only a fraction of the computational resources that would be required to run the same experiments in LES. In addition, the simplified nature of the model allows us to develop a more fundamental understanding of how primary model biases influence the relative humidity in the NBL.

We start the part on the observations in Section 4.2 with a description of the measurement sites, and describe in Section 4.2.1 the methods used for the selection and analysis of the relevant nights. In Section 4.2.2 and 4.2.3 the general characteristics and extremes of the nocturnal conditions are described. The second part of this chapter starts in Section 4.3.1 with the derivation and validation of the conceptual model, followed by the numerical experiments in Section 4.3.2. Finally, the entire chapter is discussed in Section 4.4.

## 4.2 Moisture characteristics of European summertime nights

To quantify the (relative) moistness of summertime nights, and the spatial differences across northwest Europe, we analyze data from three measurement sites. The sites at Cabauw (Netherlands), Hamburg (Germany) and Karlsruhe (Germany) were selected because of the availability of tower measurements and the relatively long observational records that are available for these sites: for this study 2001-2014 for Cabauw and Karlsruhe, and 2004-2012 for Hamburg. Although all three locations are in the same Köppen-Geiger climate classification, the characteristics of the sites are quite diverse.

Hamburg is located in the northern part of Germany, ~75 km - 100 km from both the Baltic and North sea. The weather mast (280 m high), operated by the University of Hamburg, is located in the southeastern outskirts of the city ($53.52^o$N, $10.10^o$E), surrounded by the city, industrial areas and community gardens, with more rural terrain towards the east (Brümmer et al., 2012). As shown in Figure 4.2, the measurement site is typically downwind of the city. The Cabauw Experimental Site for Atmospheric Research (CESAR) is located in the western part of the Netherlands ($51.97^o$N, $4.93^o$E), at ~40 km distance from the North sea. The measurement site is located in

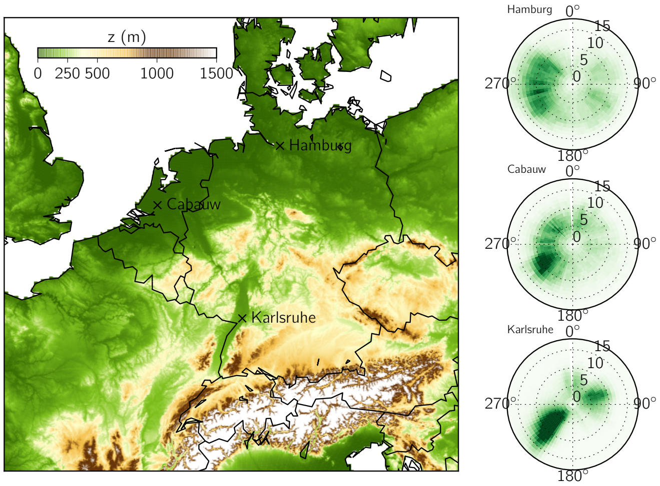

*Figure 4.2: Map showing the location of the measurement sites, with indication of the May through August wind direction.*

a low (0.7 m above sea level) and flat polder, with the tower (200 m high) surrounded by relatively homogeneous open pasture and small drainage ditches (Van Ulden and Wieringa, 1996). Karlsruhe is on the southwestern border between Germany and France. The measurement site ($49.10^o$N, $8.43^o$E), operated by the Institute for Meteorology and Climate research – Karlsruhe Institute of Technology (KIT), is located in the relatively flat Rhine valley, but with stronger orography (Odenwald, Pfälzerwald and Schwarzwald) in the near vicinity. As shown in Fig. 4.2, this has a strong impact on the wind direction (Kalthoff and Vogel, 1992). The measurement tower (200 m high) is located in a pine forest, with the observations below 20 m collected at a small meadow directly north of the tower. See Appendix A.5 for additional details about the sites.

Given the location of the sites, certain relevant characteristics – like the soil moisture content – are expected to differ. However, as we don't have soil moisture observations from all sites, differences among the sites, and the impact of soil moisture on the observed conditions, could not further be studied.

### 4.2.1 Data selection and analysis method

Because of the current study's interest in daytime convection, the analysis focusses on the summer (May through August) period. Compared to Chapter 3, where we only analyzed data from clear (cloudless) nights, the sampling criteria is relaxed to nights in between relatively clear (and with that most likely convective) days. This way, nights at which fog or low clouds occur are included in the analysis. The total and sampled number of nights are shown in Table 4.1, the sampling criteria and procedure is described in Appendix A.2. Unless stated otherwise, from this point on *"nights"* will refer to the sampled set of nighttime conditions.

For all nights the temporal evolution of the NBL is studied over the period at which the lower atmosphere is stably stratified, based on the virtual potential temperature gradient between 2 m and 10 m. The first time in the evening at which this criteria is met is referred to as $t_{\mathrm{N0}}$, the last time in the morning as $t_{\mathrm{N1}}$, and the time in between is normalized as $\widehat{t} = (t - t_{\mathrm{N0}})/(t_{\mathrm{N1}} - t_{\mathrm{N0}})$. This ensures that the initial vertical profiles like the potential temperature and specific humidity are close to the (well-mixed) convective conditions, and the temporal evolution over the period $\widehat{t} = \{0 - 1\}$ describes the deviation from the convective conditions. For Cabauw and Hamburg $t_{\mathrm{N0}}$ is on average 2.1 hours before sunset, for Karlsruhe 2.8 hours before sunset. The average night length ($t_{\mathrm{N1}} - t_{\mathrm{N0}}$) is 11.7 hours for Hamburg, 12.4 hours for Cabauw, and 13.3 hours for Karlsruhe.

The analysis focusses on moisture related variables like the relative humidity (RH), dew point depression ($T - T_{\mathrm{d}}$) and specific humidity ($q$). The selected variables are studied using two dimensional histograms, with the normalized time $\widehat{t}$ on the $x$-axis, and the probability on the $y$-axis, with the frequency within each time bin normalized to unity.

### 4.2.2 General characteristics

We start by analyzing the temporal evolution of relative humidity (Fig. 4.3) and specific humidity (Fig. 4.4), to obtain an overview of the typical conditions and differences across northwest Europe.

#### 4.2.2.1 Initial conditions ($\widehat{t} = 0$)

Near the surface (2 m) the mean (median) initial relative humidity decreases going further inland, from ~65% in Cabauw to ~52% in Hamburg and ~47% in Karlsruhe, thus showing differences as large as 20% over a distance of 400 km. The variation between Cabauw and Kalrsruhe is mostly caused by a difference in temperature: the initial specific humidity is approximately the same for both sites, but the temperature differs as much as 6 K (Table 4.1). Most likely because of its close proximity to the city and the associated decrease of soil moisture, the specific humidity is lower in Hamburg.

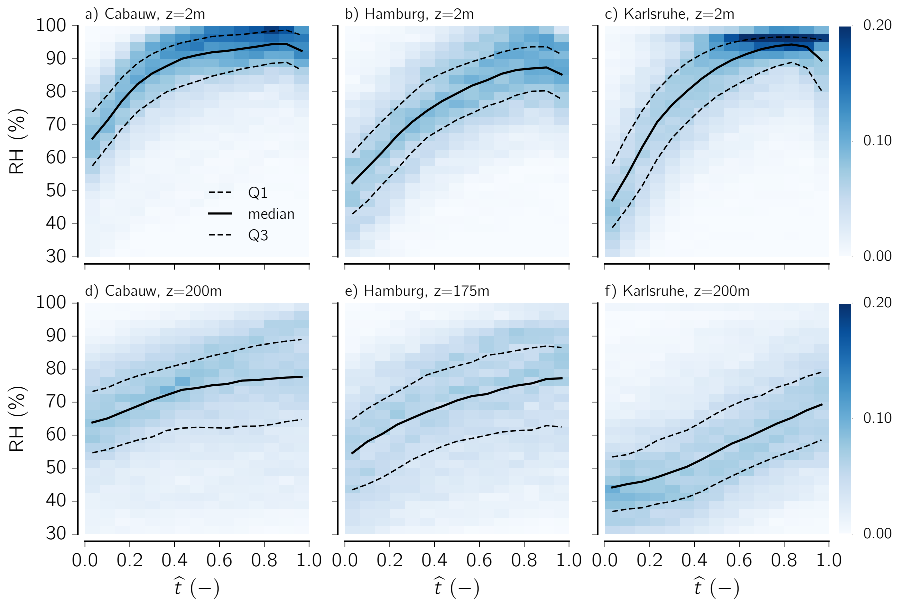

*Figure 4.3: 2D histograms of the relative humidity at 2 m height (top) and ~200 m height (bottom). The solid line indicates the median value, the dashes lines the interquartile range.*

*Table 4.1: Statistics of the measurement sites. Median temperature (T) and specific humidity (q) at $\hat{t} = 0$, z = 2 m. N = total and sampled number of nights which are considered in the statistics, f fraction of sampled nights*

| | $T\|_{t_{N0}}$ (K) | $q\|_{t_{N0}}$ (g kg$^{-1}$) | $N_{tot}$ (-) | $N_{samp}$ (-) | $f$ (%) |
|---|---|---|---|---|---|
| Cabauw | 290.1 | 8.3 | 1722 | 867 | 50.3 |
| Hamburg | 291.6 | 7.5 | 1099 | 530 | 48.2 |
| Karlsruhe | 296.3 | 8.4 | 1709 | 958 | 56.1 |

#### 4.2.2.2 Temporal evolution NBL

During the night, all sites show the strongest increase in RH near the surface, where Hamburg is (relatively) most dry (Fig. 4.3). Despite the large initial difference between Cabauw and Karlsruhe, the latter shows a stronger increase in RH during the night, resulting in similar early morning median relative humidities of 94-95% for both sites. As shown in Fig. 4.4, the specific humidity tendencies during the night are small, with typically net differences between $t_{N0}$ and $t_{N1}$ of less than 1 g kg$^{-1}$. The near surface drying tendency for Cabauw is in line with the results from de Roode et al. (2010).

To quantify the contribution of changes in specific humidity to changes in the relative humidity, the relative humidity budget is studied (Ek and Mahrt, 1994):

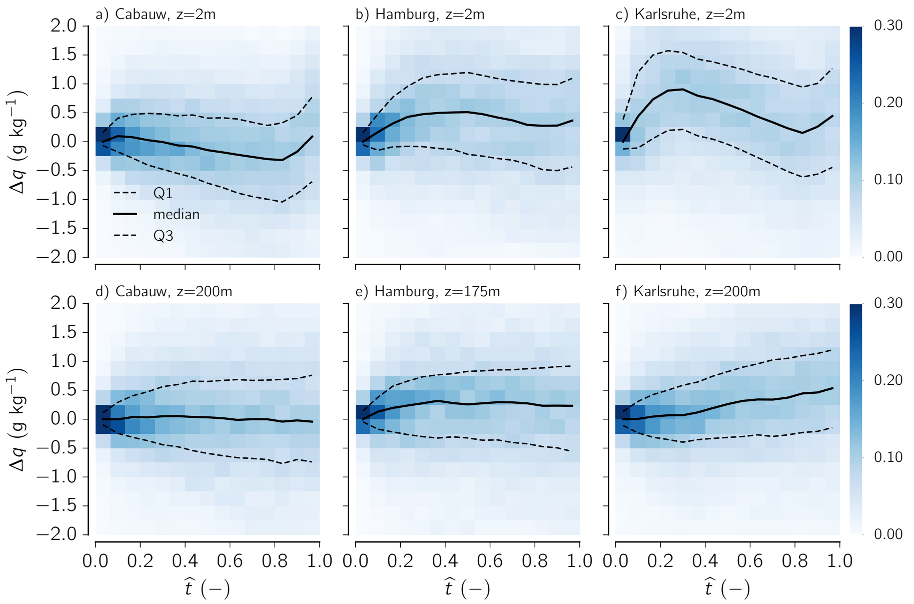

*Figure 4.4: Like Fig. 4.3, for the change in specific humidity since $t_{\mathrm{N0}}$.*

$$\frac{\partial \mathrm{RH}}{\partial t} = \frac{\partial}{\partial t}\left(\frac{q}{q_{\mathrm{s}}}\right) = \underbrace{\frac{1}{q_{\mathrm{s}}}\frac{\partial q}{\partial t}}_{\delta q} - \underbrace{\frac{\mathrm{RH}}{q_{\mathrm{s}}}\frac{\partial q_{\mathrm{s}}}{\partial T}\frac{\partial T}{\partial t}}_{\delta T}, \tag{4.1}$$

where $q_{\mathrm{s}}$ is the saturation specific humidity. The budget terms – indicating the change in relative humidity due to drying or moistening of the ABL ($\delta q$) and warming or cooling of the ABL ($\delta T$) – are calculated approximating the time derivatives as finite differences forward in time (with a 10 minute data interval). A time integration of Eq. 4.1 then provides us with the relative contribution of the two different terms over the night. To prevent an accumulation or growth of the error due to the finite difference approximation, we use the observed RH on the right hand side, instead of the numerically integrated RH. The results are shown in Fig. 4.5. For all sites the drying of the near-surface layers contributes only ~0-4% to the RH tendency, which is an order of magnitude less than the impact of NBL cooling.

One question that remains in the explanation of the RH changes during the night is the cause of the stronger NBL cooling for Karlsruhe. There are a number of potential causes for this behavior: (i) differences in net surface radiation ($Q_{\mathrm{net}}$), (ii) differences in the redistribution of NBL cooling with height (shallow and cold versus a deep and warm NBL), or (iii) larger scale processes. Process (i) is unlikely as compared to Cabauw and Hamburg, Karlsruhe has on average the highest (least negative) $Q_{\mathrm{net}}$. Process (ii) is unlikely as the stronger cooling compared to Cabauw and Ham-

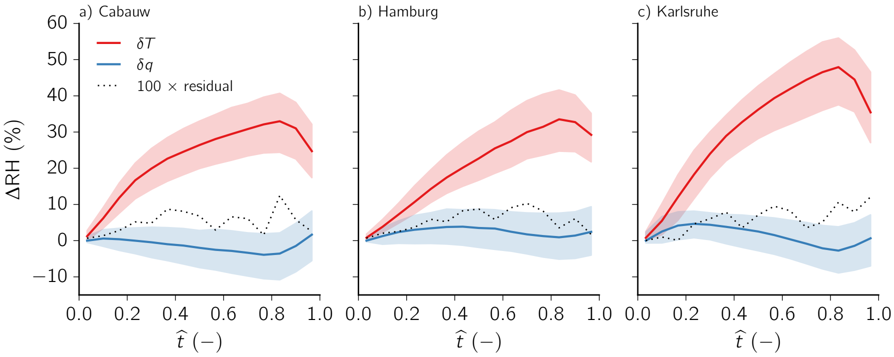

*Figure 4.5: Relative humidity budget at 2 m height, derived using Eq. 4.1. $\delta T$ is the contribution of changes in temperature, $\delta q$ the changes due to changes in specific humidity, and the grey lines indicate the residual (diagnostic tendency minus prognostic tendency). Solid lines denote median values, the shaded area the interquartile range.*

burg is present over the entire vertical extent of the tower. Process (iii) is difficult to quantify, but given the small height differences along the axis of the Rhine valley, and increases in terrain height towards the south (Schwarzwald), west (Pfälzerwald) and east (Odenwald), drainage flows and pooling of cold air in the Rhine valley is a possible explanation of the increased NBL cooling (e.g. Kondo et al., 1989).

### 4.2.3 Extremes during the nocturnal period

Although the two-dimensional histograms are useful to summarize the typical evolution of the NBL, it is difficult to obtain extremes from such figures. For example, for the relative humidity in Fig. 4.3, the interesting details – how often does the NBL saturate? – are difficult to obtain. Furthermore, since extremes like the maximum nighttime relative humidity don't necessarily occur at the same time during different nights, some details are lost.

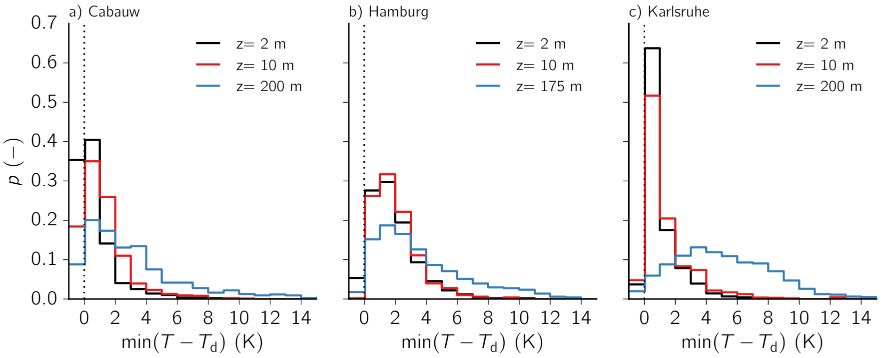

*Figure 4.6: Histogram of minimum dew point depression between $t_{N0}$ and $t_{N1}$. The first bin encloses all values from $-\infty < (T - T_d) \leq 0$ K.*

As a more strict assessment of these extremes, Fig. 4.6 shows histograms of the minimum dew point depression observed during all of the sampled nights. At 2 m height Cabauw frequently experiences conditions which are saturated, with a probability of 0.35, corresponding to a frequency of approximately once every 3 nights. These findings are in line with the direct visibility measurements (2011-2014, not shown). For Hamburg and Karlsruhe the probability is much lower: 0.05 (1/20 days) and 0.035 (1/28.6 days), respectively. For Cabauw the probability decreases with height, to 0.18 (1/5.6 days) at 10 m height and 0.08 (1/12.5 days) at 200 m height. For Karlsruhe the probability slightly increases at 10 m height to 0.045 (1/22.2 days). Considering that we have approximately 4×30 nights during the May through August period and analyze about 50% of them (Table 4.1), the frequency of finding a saturated night above 2 m height in Hamburg, or above 10 m height in Karlsruhe, is very small at about one night during this period.

Although saturated conditions at 200 m height (Hamburg: 175 m) in between convective days are only rarely observed, all sites are frequently close to saturation. For example, for the range $0 < T - T_\mathrm{d} \leq 2$ K, the probabilities are 0.37 (1/2.7 days) for Cabauw, 0.34 (1/2.9 days) for Hamburg and 0.14 (1/7.1 days) for Karlsruhe.

Summarized, even for the summer period – which is typically drier than the winter season – Northwest European nights are relatively moist. At 2 m height the late night median relative humidities are as high as 94-95% for Cabauw and Karlsruhe, and the strong increase in RH during the night is mostly governed by a decrease in temperature, where changes in specific humidity only play a minor role. Despite the high relative humidities, only Cabauw (situated in a low and moist polder) frequently experiences saturation near the surface. Although the probability of finding saturated conditions decreases with height, the atmosphere at 200 m height is often within 2 K from saturation. The implications of these findings are discussed in the next section.

## 4.3 Implications of model biases on low nocturnal clouds

The previous section showed that saturation at night most likely occurs near the surface, but only for certain locations (Cabauw). Given the positive near-surface temperature biases that arise from an overestimation of vertical mixing (Fig. 4.1), these shallow mist layers are likely absent in low resolution LES. Furthermore, even in the absence of temperature (or other model) biases, the vertical grid spacing in low resolution LES near the surface is likely insufficient to resolve mist with such a small (<

10 m) vertical extent. We postulate that the absence of such shallow mist layers in LES is unlikely to influence the NBL development, or convection during the following day. First, we studied the influence of fog/mist on the nocturnal radiation balance using an offline one-dimensional radiative transfer model (Pincus and Stevens, 2013, results not shown). By varying both the vertical extent (0 to 50 m) and liquid water content (0 to 0.5 $g\ m^{-3}$) of the fog layer, and comparing the net surface radiation with a clear sky experiment, it became obvious that the observed shallow fog/mist layers influence the longwave incoming radiation by only a few W $\mathrm{m}^{-2}$. Second, after sunrise these thin mist layers are insufficiently opaque to block the incoming shortwave radiation, and early morning surface heating typically causes a quick evaporation of such fog layers (e.g. Stull, 1988).

More interesting are the conditions where model biases have the potential to form spurious low clouds, as the NBL temperatures near or above the NBL top are underestimated (Fig. 4.1). At least in theory, this could create deeper cloud layers which have a stronger impact on the nocturnal radiation budget, and which can persist after sunrise, delaying the development of the convective boundary layer (Yin et al., 2015; Anber et al., 2015).

To address whether model biases as illustrated in Fig. 4.1 could cause spurious low clouds, we study the impact that overestimating vertical mixing has on the relative humidity in the NBL, using a conceptual model. The conceptual model allows us to perform sensitivity experiments for a wide range of conditions, using only a fraction of the computational resources that would be required for LES.

### 4.3.1 Description conceptual model

We consider a nocturnal boundary layer which develops from idealized convective conditions (Fig. 4.7a): a convectively mixed layer (CBL) of depth $z_\mathrm{c}$, with a constant potential temperature $\langle\theta\rangle$ and specific humidity $\langle q\rangle$ (e.g. Lilly, 1968). For European conditions, $z_\mathrm{c}$ is typically around 1-2 km, with a mixed-layer top relative humidity ($\mathrm{RH_c}$) often close to, but less than, 100%. The initial relative humidity in the NBL is mostly governed by $z_\mathrm{c}$ and $\mathrm{RH_c}$, with the highest relative humidities (most favorable for saturation during the night) arising from a shallow and relatively moist CBL. From $z_\mathrm{c}$, $\langle\theta\rangle$, and $\mathrm{RH_c}$, the bulk specific humidity $\langle q\rangle$ can be calculated, which based on the findings of Section 4.2.2 is assumed to be constant throughout the night.

Unlike for convective conditions, where turbulence is typically sufficiently strong to maintain well-mixed potential temperature profiles, we can't assume a similar bulk

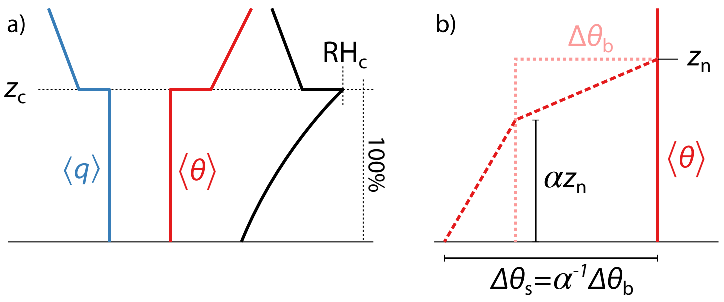

*Figure 4.7: Sketch initial convective conditions (left) and NBL parameterization (right)*

change of potential temperature in the NBL. Depending on the amount of turbulence at night, two types of NBLs tend to form: If turbulence is weak and the development of the NBL is mostly driven by radiation, concave upwards potential temperature profiles (with the strongest temperature gradient near the surface) are formed (e.g. Stull, 1983a,b, 2000). For more turbulent conditions, turbulent mixing creates slightly better well-mixed conditions, with the strongest temperature gradients near the NBL top (e.g. Vogelezang and Holtslag, 1996). We adopt a vertical structure typical for turbulent conditions, as according to the classification proposed by Vogelezang and Holtslag (1996)[1], 76.5% - 80% of the nights used in Section 4.2 are of the turbulent kind.

To determine the shape of the temperature profiles, we use the LES results from Chapter 3. These experiments were set up to cover the typical European conditions, and in addition, range from well to under-resolved LES experiments. Fig 4.8a shows the potential temperature profiles, analyzed at sunrise. The characteristics of the high-resolution experiments (darkest colors) range from boundary layer depths of 75 m to 200 m, with temperature differences between the surface and residual layer of -7 K to -13 K. With increasing grid spacing (increasingly lighter colors), the relative biases in NBL depth are as large as 100%.

If we define the total NBL cooling between $t_{\mathrm{N0}}$ and some arbitrary time $t_1$ later as:

$$\Delta Q = \int_{t_{\mathrm{N0}}}^{t_1} \left(\overline{w'\theta'_s}\right) \mathrm{d}t = \int_0^{z_{\mathrm{n}}} \left[\theta(t_1, z) - \theta(t_{\mathrm{N0}}, z)\right] \mathrm{d}z, \tag{4.2}$$

with $z_{\mathrm{n}}$ the depth of the stable boundary layer, the bulk cooling equals (Fig. 4.7b):

$$\Delta\theta_{\mathrm{b}} = \frac{\Delta Q}{z_{\mathrm{n}}}. \tag{4.3}$$

---

[1] Their criteria to distinguish between radiation or turbulence dominated nights is that for radiative cases, $\mathrm{d}^2\theta/\mathrm{d}z^2 < 0$ throughout the NBL

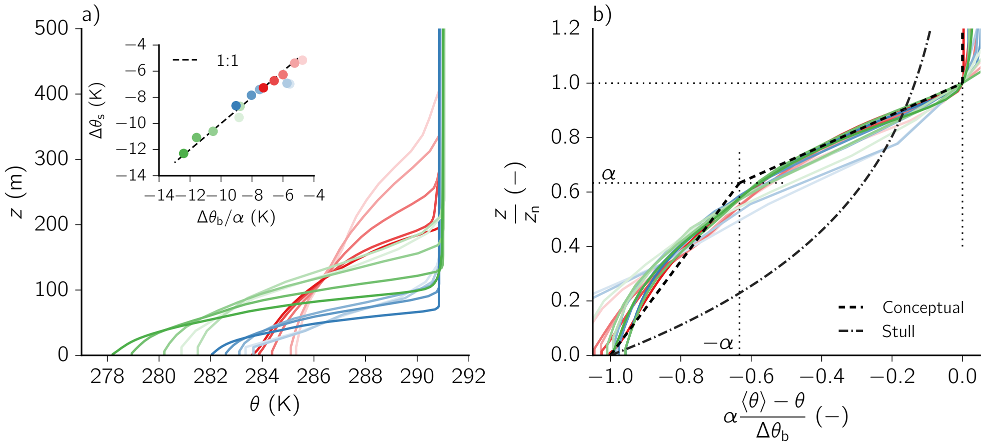

*Figure 4.8: LES experiments from Chapter 3, unscaled (left) and scaled (right). The dashed line in b) indicates the temperature structure that we assume, the dash-dotted line the temperature structure from Stull (2000).*

As shown in the inset in Fig. 4.8a, the total potential temperature difference over the NBL ($\Delta\theta_\mathrm{s}$) scales well with $\Delta\theta_\mathrm{b}$, with the inclusion of some pre-factor $\alpha = 1.9/3$. If we use this relation – together with the boundary layer depth $z_\mathrm{n}$ – to scale the temperature profiles, we find a universal shape for the vertical structure of the NBL, as shown in Fig. 4.8b. Although the scaling sets the temperature at the surface ($\theta = \langle\theta\rangle + \alpha^{-1}\,\Delta\theta_\mathrm{b}$) and NBL top ($\theta = \langle\theta\rangle$), it still requires assumptions about the distribution of the total cooling with height (Eq. 4.2). We propose a simple two layer structure, with the temperature at a height $\alpha z_\mathrm{n}$ equal to $\langle\theta\rangle - \Delta\theta_\mathrm{b}$ (Fig. 4.7). As shown in Fig. 4.8b (dashed line), this gives a reasonable agreement with the LES experiments, without introducing too much complexity in the assumptions of the vertical NBL structure. We should stress that in the results from Fig. 4.8, and the remainder of this study, $\alpha$ is fixed at $\alpha = 1.9/3$. Also included in Fig. 4.8b is the parameterization proposed by Stull (2000):

$$\theta = \langle\theta\rangle - \Delta\theta_\mathrm{s}\,\mathrm{e}^{-z/H_\mathrm{e}}, \tag{4.4}$$

where we used an e-folding height $H_\mathrm{e} = 0.5 z_\mathrm{n}$ for a best fit to the LES data. It is clear that the exponential fit is not appropriate for these more turbulent cases.

Summarized, given the total NBL cooling $\Delta Q$ and the NBL depth $z_\mathrm{n}$, the conceptual model can reproduce the vertical potential temperature structure of the NBL. Given the results from Fig. 4.8b, the model not only reproduces the vertical structure observed in high resolution (well-resolved) LES, but also the change in structure as the NBL depth is overestimated in low resolution LES.

### 4.3.2 Numerical solutions

With the conceptual model we can study how the vertical structure of the NBL changes as a function of the nocturnal boundary layer depth $z_\mathrm{n}$, where increasing $z_\mathrm{n}$ mimics the impact of overestimating vertical mixing as observed in low-resolution LES or many boundary layer parameterizations (Cuxart et al., 2006)). We perform a number of experiments, starting from a convective boundary layer with conditions typical for northwestern Europe (Table 4.1). The initial conditions are listed in Table 4.2.

*Table 4.2: Initial conditions of the numerical experiments with the conceptual model*

| Description | symbol | value |
|---|---|---|
| Convective boundary layer depth | $z_\mathrm{c}$ | 1000 m |
| Bulk potential temperature CBL | $\langle\theta\rangle$ | 293 K |
| Bulk specific humidity CBL | $\langle q\rangle$ | 8.3 g kg$^{-1}$ |
| Relative humidity at $z_\mathrm{c}$ | RH$_\mathrm{c}$ | 95% |
| Surface pressure | $p_\mathrm{s}$ | $10^5$ pa |

For the experiments we differ the total amount of NBL cooling according to Eq. 4.2 by prescribing a fixed surface sensible heat flux H (with $\overline{w'\theta'_s} = \mathrm{H}/(\rho c_\mathrm{p})$ over a time period $t_1 - t_{\mathrm{N}0} = 32400$ s. Given the total cooling over the nocturnal period, the NBL depth $z_\mathrm{n}$ is varied, the temperature profiles are reconstructed, and using $\langle q\rangle$ (fixed in time) the relative humidity at the surface (RH$_\mathrm{s}$) and at $\alpha z_\mathrm{n}$ (RH$_\mathrm{t}$) is calculated.

Figure 4.9a shows the resulting RH at the surface (solid lines) and at $\alpha z_\mathrm{n}$ (dashed lines) as a function of $z_\mathrm{n}$, for three different surface cooling rates. The results are divided in two areas: the top-left area where for a given $z_\mathrm{n}$ the RH is highest at the surface, and the bottom-right area where the RH is highest near the NBL top. A number of conclusions can be drawn from these experiments:

1. For conditions which are close to saturation, the surface RH is higher than the RH at $\alpha z_\mathrm{n}$, or saturates at a lower $z_\mathrm{n}$, thus favoring saturation near the surface (fog/mist) over low clouds, which is in line with the findings from Section 3.2.
2. For almost all conditions, increasing $z_\mathrm{n}$ — as would be the results of overestimating vertical mixing — results in a decrease in RH at both the surface and

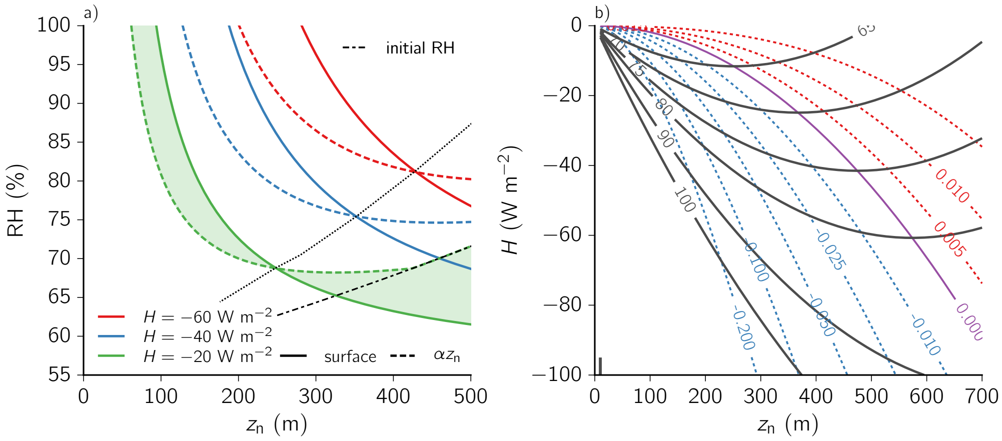

*Figure 4.9: Experiments with the conceptual model, using the initial conditions from Table 4.2. Left: relative humidity at the surface and $\alpha z_n$ for three different cases. Right: relative humidity at $\alpha z_n$ (solid lines), and the total RH tendency calculated using Eq. 4.5 (dashed lines).*

$\alpha z_n$. This makes it unlikely that overestimating vertical mixing could cause a spurious formation of low clouds.

3. The only conditions where the RH at $\alpha z_n$ increases with a deepening NBL occur for weakly cooled and deep NBLs ($H = -20$ W/m$^{-2}$, $z_n > 250$ m). Note that for the case with the weakest cooling (-20 W m$^{-2}$) the absolute temperature at $z_n$ can become lower as the temperature at $\alpha z_n$. In such a case the highest RH is located at $z_n$, which equals the initial RH profile of the convective conditions (dash-dotted line), which by definition can never be higher than RH$_c$.

These results are easier to understand if we consider how the relative humidity changes as a function of $z_n$. At the surface, increasing $z_n$ always results in a decrease in RH, so we will focus on the RH at $\alpha z_n$. The tendency at this height can be expressed as:

$$\frac{\partial \mathrm{RH_t}}{\partial z_n} \approx \underbrace{\frac{\mathrm{RH}}{q_s}\frac{\epsilon}{p}\frac{\partial e_s}{\partial T}\frac{\Delta Q}{z_n^2}}_{\delta\theta} + \underbrace{\frac{\mathrm{RH}}{q_s}\frac{\epsilon}{p}\frac{\partial e_s}{\partial T}\frac{\alpha g}{c_p}}_{\delta T} - \underbrace{\frac{\mathrm{RH}}{p}\alpha\rho g}_{\delta p}. \tag{4.5}$$

See appendix A.4 for the derivation and definition of symbols, which have their standard meaning. The tendency equation consists of three terms: the first term ($\delta\theta$) describes how the change in potential temperature – which by definition is positive as the NBL is deepened – decreases the relative humidity. As the relative humidity depends on the absolute temperature, the second term ($\delta T$) describes the influence of adiabatic cooling on the relative humidity, which by definition is a negative contribution to the RH budget. The last term ($\delta p$), which is small compared to the other two terms, describes the change in RH caused by the dependence of the saturation specific humidity on pressure.

In Fig. 4.9b the relative humidity at $\alpha z_n$ (solid black contours), and its tendency as a function of $z_n$ (colored dashed lines), are shown for a wide range of conditions. The initial conditions of the experiments are identical to the cases shown in Fig. 4.9a (Table 4.2), and the results are again analyzed after a time period $t_1 - t_{N0} = 32400$ s (9 hours).

One prerequisite for a case where spurious deepening of the NBL results in saturation, is that the relative humidity at $\alpha z_n$ increases with increasing $z_n$. It is again clear that those conditions (dashed blue lines) only occur for weakly cooled and/or deep NBLs, where the boundary layer top is far from saturation. We can study this behavior further if we consider the individual terms of Eq. 4.5, which are shown in Fig. 4.10 for a case with a surface cooling $H = -40$ W m$^{-2}$. For a shallow NBL, the absolute temperature term ($\delta T$) is much weaker than the potential temperature term ($\delta\theta$), but as the latter decreases inverse proportional to the NBL depth squared, its contribution decreases quickly as the NBL is deepened. For $z_n > 450$ m, the contribution of $\delta\theta$ is offset by that from $\delta T$, so that further deepening of the NBL results in cooling, and an increase in RH.

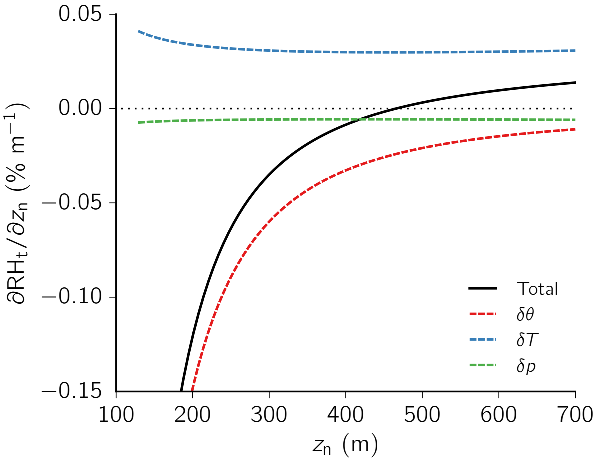

*Figure 4.10: Budget terms of Eq. 4.5, for a case with* $H = -40$ W m$^{-2}$

.

Summarized, the goal of the numerical experiments was to determine whether an overestimation of the NBL depth, as observed in low-resolution LES and many RANS models, could results in saturation of the NBL. The numerical experiments indicate that this is very unlikely: for conditions which are close to saturation, the highest relative humidities are found near the surface. In addition, for nearly all cases, deepening the NBL results in a decrease in relative humidity throughout the NBL.

## 4.4 Summary and conclusions

In this chapter we studied whether the typical model biases in the nocturnal boundary layer – an overestimation of the boundary layer depth caused by too much vertical mixing – was likely to influence the formation of fog or low clouds. Such overestimations of the boundary layer depth are typical for low-resolution LES (low-resolution with respect to the grid spacing required to resolve nocturnal turbulence), but also for many boundary layer parameterizations based on the RANS equations. The result of overestimating vertical mixing is typically an overestimation of the near surface temperature, and underestimation of the temperatures near or above the NBL top, potentially causing an absence of fog/mist occurring in reality, or a spurious formation of low clouds near/above the NBL top.

We addressed the question whether this is likely to happen using both observations, and a newly developed conceptual model. From the observations of Cabauw, Hamburg and Karlsruhe we only considered the summertime period (MJJA), and given our interest in how NBL biases might influence daytime convection, further subsampled the nights in between convective days. Even after subsampling the (convective) summertime conditions, the NBL is still surprisingly moist, with median early morning (sunrise) relative humidities at 2 m height as high as 94-95% for Cabauw and Karlsruhe. Most likely due to its close vicinity to the city, the early morning relative humidities in Hamburg are $\sim$ 10% lower. Higher up (200 m), the relative humidities are much lower, typically around 70% - 80%. By studying the extremes during the nocturnal period, it became clear that only Cabauw frequently experiences saturated conditions near the surface, occurring roughly once every three nights. Given the positive near-surface temperature biases that arise from overestimating vertical mixing, and the small vertical extent of these fog/mist layers ($<$ 10 m), these events are likely unresolved in low-resolution LES. However, given their small vertical extent, we argued that this is unlikely to influence the NBL development, or have an impact on the following day of convection.

The study of the nocturnal extremes also indicated that at 200 m height, the NBL is frequently within 2 K of saturation. With the negative temperature biases that arise from overestimating vertical mixing, this could theoretically cause a spurious formation of low clouds. We addressed this question using a newly developed conceptual model which, given the total nocturnal cooling and NBL depth, realistically reproduces the vertical structure of the NBL. By varying the boundary layer depth – to mimic typical parameterization errors – for a given amount of cooling, this allowed us to study if overestimating vertical mixing could result in low clouds, for a wide range of conditions. The results indicate that a spurious formation of low clouds is unlikely to happen. First, for conditions which are close to saturation, the maximum RH is observed near the surface. Second, conditions where deepening the NBL results in an increase in the NBL top relative humidity only occur for weakly cooled and/or deep boundary layers, where the NBL top is far from saturation.

These findings complement the conclusions from Chapter 3. For LES experiments of the diel cycle of convection, where the main focus is on daytime convection and where details of the nocturnal boundary layer are less important, the use of a resolution which is insufficient to resolve nocturnal turbulence is unlikely to influence daytime convection. This greatly relaxes the requirements on resolution, opening the possibility for LES of the diel cycle of convection on domains as large as hundreds or a thousand kilometer.

## Chapter V

# Large-eddy simulation of a transitionally stable boundary layer: a bridge too far?

The GABLS4 intercomparison case – a transitionally stable boundary layer over the Antarctic (Dome C) – is studied using large-eddy simulation (LES). Being in the transitionally stable regime, where turbulent intensities rapidly decrease with increasing stability, the case is continuously turbulent, but with turbulence kinetic energy (TKE) that is an order of magnitude less than, for example, observed in the weakly stable GABLS1 case. As a result, a very fine computational mesh is required to resolve the small turbulence production scales. With a sensitivity study on resolution, varying the grid spacing from $5 \times 5 \times 2$ m$^3$ down to $0.25 \times 0.25 \times 0.25$ m$^3$, it is demonstrated that obtaining a valid LES experiments, which is well-resolved and where the statistics (first and second order moments) converge with increasing resolution, is difficult.

## 5.1 Introduction

Large-eddy simulation (LES) of the stable boundary layer (SBL) has been – and still is – a challenging task (e.g. Mason and Derbyshire, 1990; Beare and Macvean, 2004). Compared to convective conditions where (amongst others production factors) buoyancy produces large turbulent structures, buoyancy suppresses turbulent motions in the SBL, resulting in much smaller (and often weaker) turbulent eddies.

The intensity of turbulence in the SBL depends on the stability of the atmosphere, which is often classified in three regimes, based on the ratio of height to the Obukhov length ($z/L$, Mahrt, 1998) or on the gradient Richardson number ($\mathrm{Ri_g}$). For the latter, $\mathrm{Ri_g} < \mathcal{O}(0.1)$ is called the "weakly stable" regime, $\mathcal{O}(0.1) < \mathrm{Ri_g} < \mathcal{O}(1)$ the "transition" regime, and $\mathrm{Ri_g} > \mathcal{O}(1)$ the "very stable" regime (Mauritsen and Svensson, 2007). In the weakly stable regime the heat flux increases with increasing stability, in the transition regime the opposite happens and the heat flux (and turbulent intensities) decrease rapidly with increasing stability, and in the very stable regime turbulence becomes very weak, intermittent or is completely absent (e.g. Mahrt, 1998; Ansorge and Mellado, 2014). Most LES studies to-date have focussed on weakly stable conditions, with for example gradient Richardson numbers (in the middle of the boundary layer) of ~0.1 for the first Global Energy and Water Cycle Exchanges Project (GEWEX) Atmospheric Boundary Layer Study (GABLS) LES intercomparison (Beare et al., 2006), up to ~0.3 for sensitivity studies on stability for GABLS1 (Huang and Bou-Zeid, 2013; Sullivan et al., 2016).

As an extension to more stable conditions, the GABLS community is currently conducting the fourth GABLS intercomparison study[1], with a case taking place over the Antarctic Plateau (Dome C). The intercomparison is organized for both single column models (SCM) and LES, with several experiments with varying complexity. We focus on the least complex setup (named "stage 3", GABLS4s3), which consists of a 24 hour case starting with approximately eight hours of weak convection, followed by the development of a SBL, with (mid boundary layer) gradient Richardson numbers of ~0.5-0.6. For these conditions, the buoyancy stratification starts limiting the vertical motions (the transition regime), and as a result, the turbulence intensity (turbulence kinetic energy, TKE) for this case is about an order of magnitude less than observed for GABLS1, while still being continuously turbulent. Although this case takes place over the Antarctic, summertime observations from Cabauw, Hamburg and Karlsruhe (not shown) revealed that similar conditions do – infrequently – also occur over continental Europe, and are thus interesting to study within the scope of this thesis.

In this chapter we present the results obtained for GABLS4s3. In contrast to chapter 3, the LES experiments in this chapter were performed with MicroHH, a recently developed LES and DNS (direct numerical simulation) model (van Heerwaarden et al., 2016). MicroHH is designed with the aim of creating a highly parallel and efficient code. As part of this thesis, we worked on the development of a model version capable of running on graphics processing units (GPUs, Section 2.6.1), which was used for some of the experiments in this chapter.

The goal of this study is to assess whether LES experiments for such stable conditions are feasible (within reasonable limits on the computational costs). As the results

---

[1] http://www.cnrm-game-meteo.fr/aladin/meshtml/GABLS4/GABLS4.html

from LES intercomparisons are often used to develop or validate (parameterizations for) RANS models, obtaining valid LES results is a first necessary step. Although there are no hard metrics to classify a LES experiment as "valid" or "invalid", several points can be considered to judge the validity of an experiment. Even though LES is centered around resolving turbulence, it still depends on a parameterization of the sub-grid scale (SGS) fluxes. For LES to be reliable, either the SGS fluxes have to be a faithful representation of reality, or the contribution of the SGS model has to be small, such that errors in the SGS representation do not influence the flow characteristics (e.g. Stevens and Lenschow, 2001). In practice, the second criteria – the requirement for a well-resolved LES experiment – is typically used. With increasing resolution and a decreasing contribution from the SGS model, the statistics (typically limited to first or second order moments) of the experiment are expected to converge. Such sensitivity studies have previously been done for both convective (e.g. Sullivan and Patton, 2011) and more weakly stable cases (e.g. Beare and Macvean, 2004; Beare et al., 2006; Sullivan et al., 2016). To judge the validity of the LES experiments for GABLS4s3, we perform a study similar to that of Sullivan and Patton (2011); Sullivan et al. (2016), by evaluating the convergence of the first and second order statistics with increasing resolution. In addition, spectra of the velocity components and temperature are used, to study whether details on the smallest scales (likely influenced by the conceptual SGS model) influence the lower frequency statistics.

We start in Section 5.2 with a description of the case and LES model, followed by the results in Section 5.3. The results section is split into two parts, where we first address the impact of running only (part of) the nocturnal period on a domain with a reduced size, followed by the results from the sensitivity study on resolution. Finally, the chapter is summarized in Section 5.4, and concluded with a brief outlook on future work.

## 5.2 Case and model description

The GABLS4 intercomparison is based on observations collected at Dome C (Antarctic, $75.1^{o}$ S, $123.35^{o}$ E) during the Antarctic summer (11 and 12 December 2009). Several experiments are being performed by both the SCM and LES community. We focus on the least complex setup, which is a 24 hour time integration (11 December 2009) that uses idealized atmospheric forcings, a prescribed (but time varying) surface temperature as the lower boundary condition instead of a land-surface scheme, and excludes the use of a radiative transfer model.

As we will demonstrate, the initially proposed intercomparison setup (using a grid spacing of $5{\times}5{\times}2$ $\mathrm{m}^3$) is inadequate to obtain a valid LES experiment; at this resolution (at least with our model setup) turbulence is mostly unresolved during the night. For that reason we performed a number of additional experiments: the full time period (24 hours) using an isotropic grid of $2{\times}2{\times}2$ $\mathrm{m}^3$, and a sensitivity study on resolution for the onset and first part of the nocturnal period (08:30 UTC to 14:00 UTC), with grid spacings ranging from $2{\times}2{\times}2$ $\mathrm{m}^3$ down to $0.25{\times}0.25{\times}0.25$ $\mathrm{m}^3$. In addition, we tested two methods for initializing the refined experiments starting at 08:30 UTC: by either starting the higher-resolution experiments from horizontally homogeneous conditions with random perturbations (as is typically done to initiate a LES experiment), or by using an initial temperature field which is interpolated from a lower-resolution experiment of the full 24 hour time period. As observed in the results from Beare et al. (2006), and also in experiments of the same GABLS1 case with MicroHH, stable cases in LES often have difficulties in becoming turbulent from an initial state which only has small random temperature perturbations. The application of a more realistic initial temperature field, with temperature fluctuations on larger spatial scales, might improve this behavior.

### 5.2.1 Experiments for the full time period

The experiments are initialized at 11 December 2009, 00:00 UTC. The initial atmospheric state and boundary conditions are an idealization of the observed (radiosonde and surface) conditions, shown in Fig. 5.1[2]. Both wind components are initialized at their geostrophic ($u_\mathrm{g}$, $v_\mathrm{g}$) value. In time, the case is driven by a varying surface potential temperature, shown in Fig. 5.1c. The surface pressure is fixed at 65077 Pa, resulting in absolute surface temperatures that vary between 231 K and 247.5 K. At these temperatures the absolute moisture content is very low (saturation specific humidity of ~ 0.1-0.7 g $\mathrm{kg}^{-1}$), so moisture is excluded from the experiments. Additional details of the model setup are shown in Table 5.1, with an overview of all numerical experiments in Table 5.2. In both experiments, a stretched vertical grid is used, with a constant grid spacing below ~500 m ($\Delta_{z;0}$ in Table 5.2), which is stretched to ~ 11 m at the top of the domain. To break the initial horizontal symmetry, random temperature perturbations of ±0.1 K are applied in the lowest 100 m.

---

[2] The full details of the initial and boundary conditions are available in the MicroHH Git repository at `https://github.com/microhh/microhh/tree/master/cases/gabls4s3`, or the GABLS4 website at `http://www.cnrm-game-meteo.fr/aladin/meshtml/GABLS4/GABLS4.html`

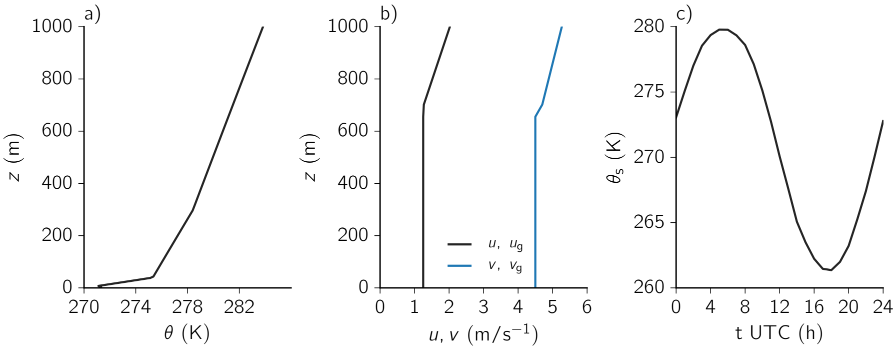

*Figure 5.1: Initial conditions of the GABLS4 case, at 11 December 2009, 00:00 UTC.*

*Table 5.1: Case specific settings for the GABLS4 experiments*

| Description | value |
|---|---|
| Smagorinsky Constant | 0.14 |
| Turbulent Prandtl number | 1/3 |
| Coriolis parameter | $-1.4 \cdot 10^{-4}$ s$^{-1}$ |
| Roughness length momentum | 0.01 m |
| Roughness length heat | 0.001 m |
| Galilean transformation | {1.5, 2.5} m s$^{-1}$ |

### 5.2.2 Experiments for the nocturnal period

The experiments for the nocturnal period are initialized at 08:30 UTC, with identical boundary conditions and forcings as used for the full time period. As listed in Table 5.2, the domain size is reduced compared to the experiments over the full time period, from 1024 m to 512 m in the horizontal, and from 955 m to approximately 600-700 m in the vertical In the horizontal this domain is roughly 10 times the nocturnal boundary layer depth, in the vertical the domain extends to beyond the convective boundary layer which was formed before 08:30 UTC. Vertical grid stretching is applied above the nocturnal boundary layer, starting at ~80 m height, with a maximum grid spacing of ~8 m at the domain top.

First, two methods are tested to initialize the experiments, using a 2×2×2 m$^3$ grid spacing. Either the experiments are initiated with horizontally homogeneous temperature and velocity fields (including temperature perturbations of ±0.1 K below 100 m), using the domain mean profiles from the $L\Delta5.00$ case (experiment $S\Delta2.00$-m), or the experiments are initiated using a sub-set of the $L\Delta5.00$ temperature field, interpolated to a new refined grid (experiment $S\Delta2.00$-t). Both runs are compared to an experiment at the same resolution, for the full time period ($L\Delta2.00$).

Second, a sensitivity study on grid spacing is performed, increasing the resolution to 0.25×0.25×0.25 m$^3$ (Table 5.2). These experiments are all started from interpolations of the $L\Delta5.00$ temperature field.

*Table 5.2: Overview of the different numerical experiments. The prefix "L" refers to the large domain and full time period, "S" to the sensitivity experiments in the small domain, and $\Delta$ to the grid spacing. $L_x$ and $N_x$ denote the x and y direction domain size and number of grid point, respectively. $\Delta_{z;0}$ is the vertical grid spacing, before grid stretching is applied above the ABL. $t_0$ and $t_1$ are the start and end times (UTC) of the experiments, and platform denotes the system used for the experiments.*

| name | $L_x$ (m) | $L_z$ (m) | $N_x$ | $N_z$ | $\Delta_{z;0}$ (m) | $t_0$ (h) | $t_1$ (h) | platform |
|---|---|---|---|---|---|---|---|---|
| $L\Delta5.00$ | 1024 | 955 | 256 | 288 | 2 | 0 | 24 | GPU |
| $L\Delta2.00$ | 1024 | 955 | 512 | 288 | 2 | 0 | 24 | GPU |
| $L\Delta2.00$-t | 1024 | 634 | 512 | 128 | 2 | 8.5 | 14 | GPU |
| $S\Delta2.00$-m | 512 | 634 | 256 | 128 | 2 | 8.5 | 14 | GPU |
| $S\Delta2.00$-t | 512 | 634 | 256 | 128 | 2 | 8.5 | 14 | GPU |
| $S\Delta1.00$-t | 512 | 590 | 512 | 192 | 1 | 8.5 | 14 | CPU |
| $S\Delta0.50$-t | 512 | 720 | 1024 | 320 | 0.5 | 8.5 | 14 | CPU |
| $S\Delta0.33$-t | 512 | 687 | 1536 | 400 | 0.33 | 8.5 | 14 | CPU |
| $S\Delta0.25$-t | 512 | 660 | 2048 | 512 | 0.25 | 8.5 | 14 | CPU |

### 5.2.3 Model description

For a general description of MicroHH we refer to Chapter 2. For the experiments of this study, the Smagorinsky-Lilly sub-grid scheme was used, with a Smagorinsky constant ($C_\mathrm{s}$) equal to 0.14, and a turbulent Prandtl number ($\mathrm{Pr}_t$) of 1/3. The choice of $C_\mathrm{s}$ and $\mathrm{Pr}_t$ is not straightforward, as both depend on e.g. stability or height in the boundary layer (e.g. Grachev et al., 2007) – a choice which is further complicated as the GABLS4s3 experiments contain both convective and stable conditions. Advection is calculated in flux form with a centered scheme, using second order accurate gradient operators, and fourth order accurate interpolations, with the time stepping (using a third order Runge-Kutta scheme) limited to maintain a maximum Courant number of 1.2.

## 5.3 Results

### 5.3.1 Full diel cycle

The temporal evolution of the experiments is largely determined by the prescribed surface temperature (Fig. 5.1c), and summarized in Fig. 5.2 for the two experiments performed over the full 24 hour time period. During the first hours of the experiments the surface sensible heat flux (Fig. 5.2b) is positive, with a maximum heat flux of ~25 W m$^{-2}$. As a result a shallow convective boundary layer is formed, with a depth of 300 m - 350 m (Fig. 5.2a). Here the boundary layer depth is estimated following Beare et al. (2006), as the height where the total momentum flux becomes less than 5% of its surface value, divided by 0.95.

After about eight hours the surface heat flux becomes negative, marking the onset of the NBL. During the night the sensible heat flux decreases to approximately -17 W/m$^{-2}$, and with the relatively light wind speeds (2.5 - 3 m s$^{-1}$ at 10 m height) and a smooth surface (Table 5.1), the surface friction velocity (Fig. 5.2c) is low, and the resulting stable boundary collapses to a vertical extent of less than 50 m.

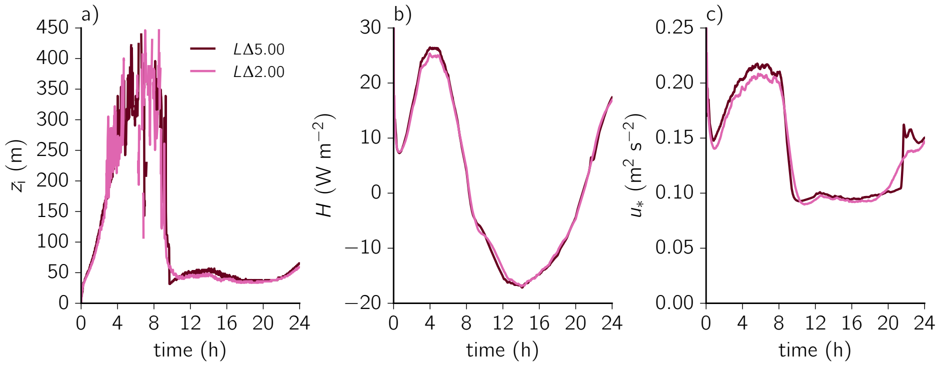

*Figure 5.2: Time series of the boundary layer depth (a), surface sensible heat flux (b), and surface friction velocity (c), for both of the full domain experiments.*

As we will show in Section 5.3.2.2, turbulence during the nocturnal period is poorly resolved in both the $L\Delta5.00$ and $L\Delta2.00$ cases. For that reason, the focus of the remainder of this chapter will be on the nocturnal period.

### 5.3.2 Nocturnal period

#### 5.3.2.1 Initialization of the nocturnal experiments

The goal of the experiments focused on the nocturnal period is to reduce the computational costs by using a smaller domain and shorter integration time, opening up the possibility to perform experiments at a higher resolution. As the first eight hours are convective, and at resolutions of $\mathcal{O}(1\ \mathrm{m})$ a further increase in resolution is expected to have little to no impact on the results (Sullivan and Patton, 2011), the convective part might be excluded from the setup. Of course, this can only be done if the development of the NBL is insensitive to details of the CBL, the size of the domain, and the procedure for starting a new experiment (including a new spin-up of the model) doesn't influence the NBL development. To address these question we compare a number of experiments:

**Large domain ($L_x = 1024$ m):**

1. $L\Delta2.00$: an experiment for the full time period (24 h);
2. $L\Delta2.00$-t: an experiment started at 08:30 UTC, with an initial temperature field that is interpolated from the $L\Delta5.00$ case.

**Small domain ($L_x = 512$ m):**

3. $S\Delta2.00$-t: an experiment started at 08:30 UTC from an initial temperature field that is interpolated from the $L\Delta5.00$ case;
4. $S\Delta2.00$-m: an experiment started from a horizontally homogeneous temperature field with random temperature perturbations, initialized at the vertical mean temperature profile of the $L\Delta5.00$.

Experiments 1. and 2. allow us to study the impact of reducing the integration time by starting an experiment at 08:30 UTC, which inevitably introduces a new model spin-up. With experiments 3. and 4. we can study the impact of the initial conditions at 08:30 UTC, being either a temperature field with realistic turbulent structures, or a horizontally homogeneous field with random perturbations. In addition, experiments 2. and 3. allow us study the impact of the reduced domain size.

Figure 5.3 shows the turbulence kinetic energy (TKE) and potential temperature variance at 9 m height. Starting with the impact of re-starting the experiments ($L\Delta2.00$ vs. $L\Delta2.00$-t), the TKE values clearly show the spin-up of the model, where it takes approximately 15 minutes before the $L\Delta2.00$-t is fully turbulent. However, after this period (at least until 12:30 UTC) both the TKE and temperature variance are nearly identical in both experiments, indicating that the spin-up has little impact on the flow characteristics. Comparing the impact of how the experiments are started ($S\Delta2.00$-t vs. *S*Δ2.00-m), the experiment started from horizontally homogeneous conditions takes twice as long to become turbulent. However, this again has little impact on the turbulence statistics.

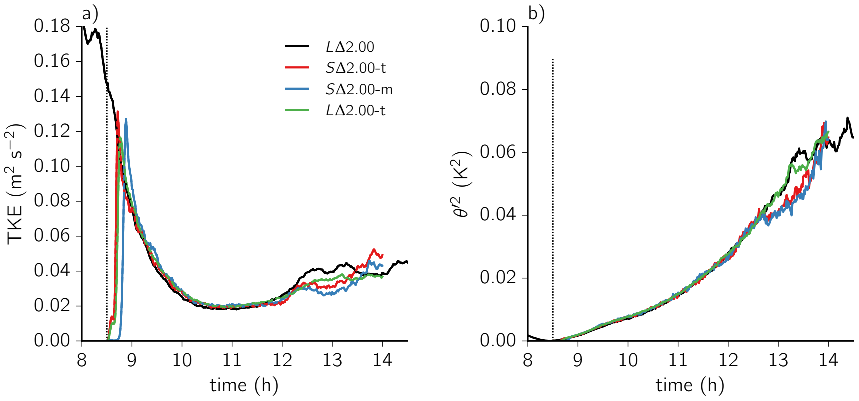

*Figure 5.3: Times series of the turbulence kinetic energy (a) and potential temperature variance (b), at 9 m above the surface.*

Around 12:30 UTC a small bifurcation is visible in the temperature variance, where the variance on both larger domains is higher than in the small domains. Although not clearly visible at 9 m height, the TKE shows a similar pattern higher up in the NBL. Fig. 5.4 shows a cross-section of the TKE, before (11:00 UTC) and after (13:00 UTC) the results start diverging. At 11:00 UTC, both in the large and small domain, turbulence is horizontally homogeneous. At 13:00 UTC long bands of increased turbulent intensity have formed, perpendicular to the wind direction. On the cause of these structures we can currently only speculate. Given the fact that the turbulent intensity increases compared to earlier times, an intermittent behavior caused by a local collapse of turbulence (Ansorge and Mellado, 2014) seems unlikely. Internal gravity waves frequently occur in stable boundary layers, and can (locally) enhance or suppress turbulence (Stull, 1988; Einaudi and Finnigan, 1993). Either way, the spatial structures that are formed seem to be marginally too large for the small domain.

Based on these results we can conclude that (1) running the experiments only for the nocturnal period is possible, as the additional model spin-up does not influence the results; (2) starting the experiments from a realistic temperature field instead of a horizontally homogeneous field with random perturbations reduces the time needed for the experiment to become turbulent; and (3) reducing the horizontal domain size from 1000 m to 500 m has a small impact on the results. Therefore, given the small differences between the large and small domain, and the four fold decrease in computational costs, a domain size of 500 m wide was chosen for the sensitivity study of

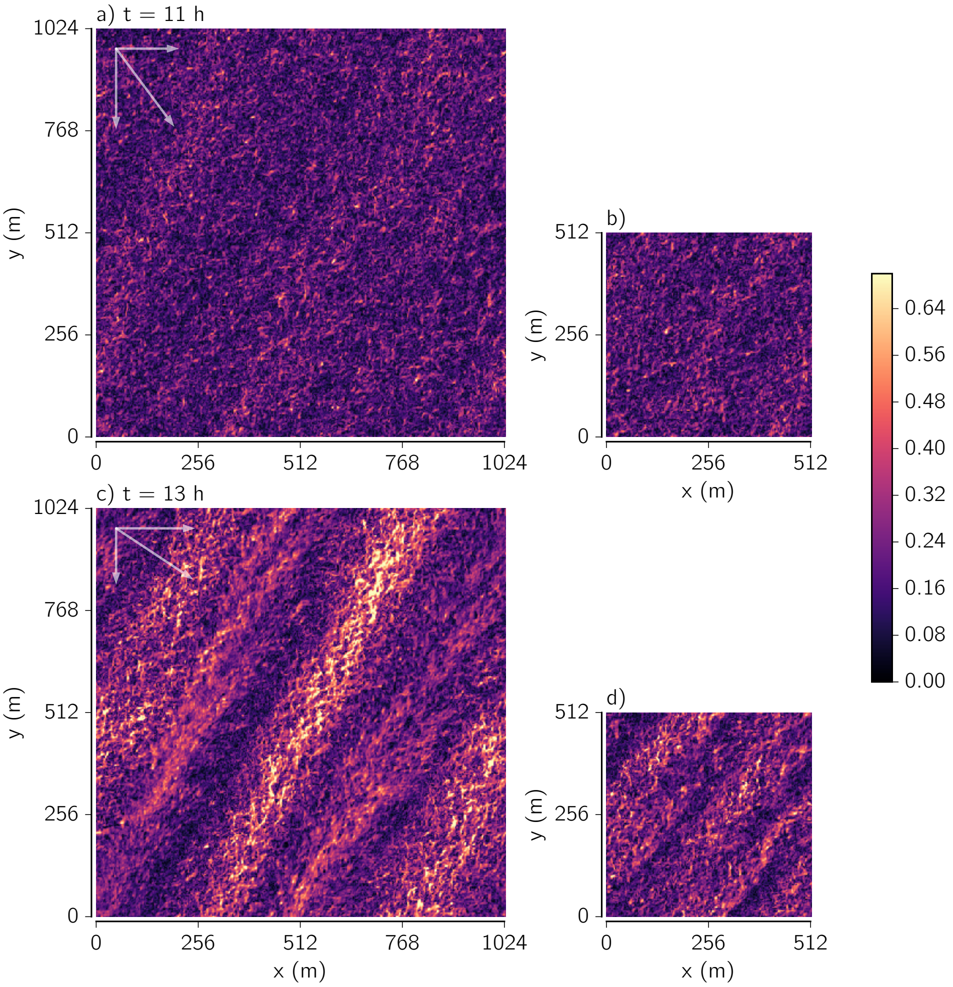

*Figure 5.4: Horizontal cross-sections of the TKE at 9 m height, at 11:00 UTC (top) and 13:00 UTC (bottom), for both the large (left) and small (right) domains.*

the next section.

#### 5.3.2.2 Sensitivity study on resolution

As will soon become evident, a resolution of 5×5×2 m$^3$ or 2×2×2 m$^3$ is insufficient to provide a well-resolved LES experiment. In this section we discuss the outcome of the sensitivity study on resolution, as outlined in Table 5.2.

Figure 5.5 shows the temporal evolution of the boundary layer depth ($z_i$), surface sensible heat flux ($H$), and surface friction velocity ($u_*$). With increasing resolution, both $H$ and $u_*$ decrease in absolute magnitude, and with less input of momentum at the surface and a decreased cooling of the SBL, the resulting SBLs are less deep. As also becomes evident from the vertical profiles shown in Fig. 5.6, the boundary layer

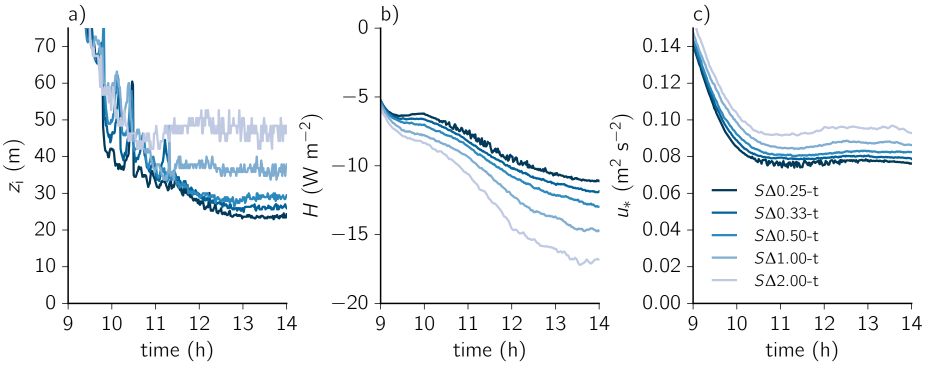

*Figure 5.5: Like Fig. 5.2, focussed on the nocturnal period.*

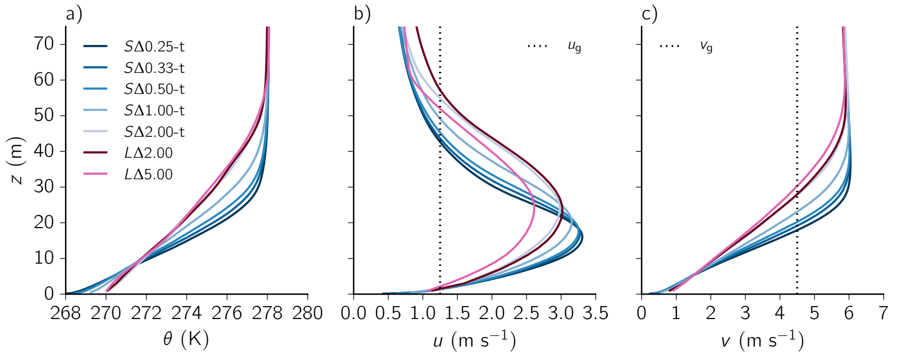

*Figure 5.6: Mean profiles of potential temperature (a), zonal (b), and meridional (c) wind, averaged between 13:00 UTC and 14:00 UTC.*

depth is overestimated by approximately 100% in the lowest resolution experiments. As a result of the additional vertical mixing, the low-level jet (LLJ, Fig. 5.6b) shifts upwards and is decreased in magnitude compared to the higher resolution runs. However, with increasing resolution the mean profiles start to converge; at the two highest resolutions the potential temperature and wind profiles are nearly identical.

An interesting feature about these results is that with increasing resolution, the buoyancy stratification (suppressing turbulence) increases, but at the same time wind shear (driving turbulent production) also increases. Fig. 5.7a-b shows the resulting total (resolved + sub-grid) fluxes of heat and the zonal wind component, with the fraction of the total flux that is resolved in Fig. 5.7c-d. At the lowest resolution ($L\Delta5.00$) turbulence is basically unresolved, and the temporal evolution of the flow is driven by the SGS model. Using an isotropic grid with the same vertical grid spacing ($L\Delta2.00$, $S\Delta2.00$) the flow becomes better resolved, although at 14:00 UTC, 60% of the heat flux and 40% of the momentum flux is still unresolved. Given the difference in resolved turbulence between the $L\Delta5.00$ and $\Delta2.00$ cases, the difference in the total heat and momentum fluxes is surprisingly small. When we further increase the resolution, turbulence becomes better resolved, up to ~80% and ~90% for the heat and momentum fluxes of the $S\Delta0.25$ case. However, the fluxes itself do not converge with increasing resolution, and the absolute change in the fluxes is about as large going from $S\Delta0.50$ to $S\Delta0.25$ as going from $S\Delta1.00$ to $S\Delta0.50$.

We continue with the analysis of two dimensional spectra of the velocity components and potential temperature. As explained in the introduction, this allows us to study if details on the smallest scales influence the lower wave number statistics. For the representation of the spectra we follow Wyngaard (2010); Sullivan and Patton (2011), and average the x-y spectra in circular bands with a constant horizontal wavenumber $\kappa_\mathrm{h} = \sqrt{\kappa_x^2 + \kappa_y^2}$, and additionally average the resulting spectra in time. As explained by Sullivan and Patton (2011), these spectra should better represent at which spatial scale eddies are acting. Two different times are compared: the period 09:00 - 09:30 UTC, when the SBL just started forming from the initially near-neutral conditions at 08:30 UTC, and the period 13:30 - 14:00 UTC, when the SBL is fully developed.

Fig. 5.8 shows the spectra for the first time period, at two heights: near the surface

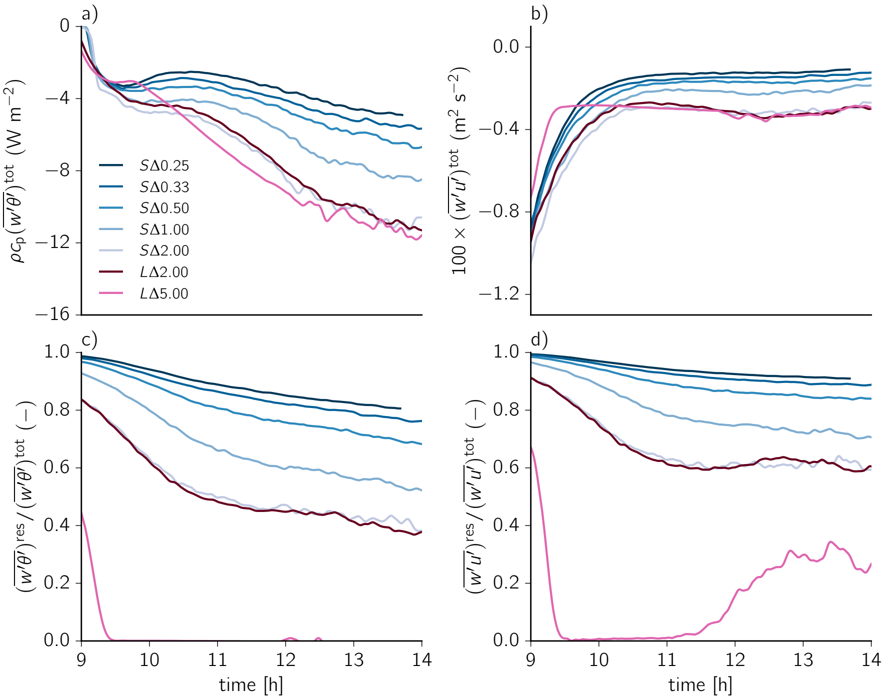

*Figure 5.7: Time series of the heat (left) and momentum (right) fluxes at 10 m height, with the fraction of the total fluxes that is resolved by the model in the bottom panels.*

(3 m) and just below the LLJ (9 m). Despite differences at the highest wave numbers (where the corresponding spatial scales approach the grid spacing, and the spectra drop off), the spectra are nearly identical at the lower range of wave numbers. Only the two lowest resolution experiments show differences, where the peak in the spectra increases and shifts to lower wave numbers. For $\kappa_\mathrm{h} \gtrsim 0.1$ (corresponding to a spatial scale of ~ 10 m), most spectra follow a $\kappa^{-5/3}$ slope (inertial subrange), only the vertical velocity spectra have a marginally smaller slope.

For the second time period, when the SBL is further developed, the behavior of the spectra changes significantly, as shown in Fig. 5.9. With increasing resolution, the peak in all the spectra decreases and shifts towards higher wave numbers, and none of the spectra converge with increasing resolution. Similar to the behavior of the fluxes (Fig. 5.7), the total variance (for the representation used here, the sum over the spectra) decreases with increasing resolution, for all three variables. These differ-

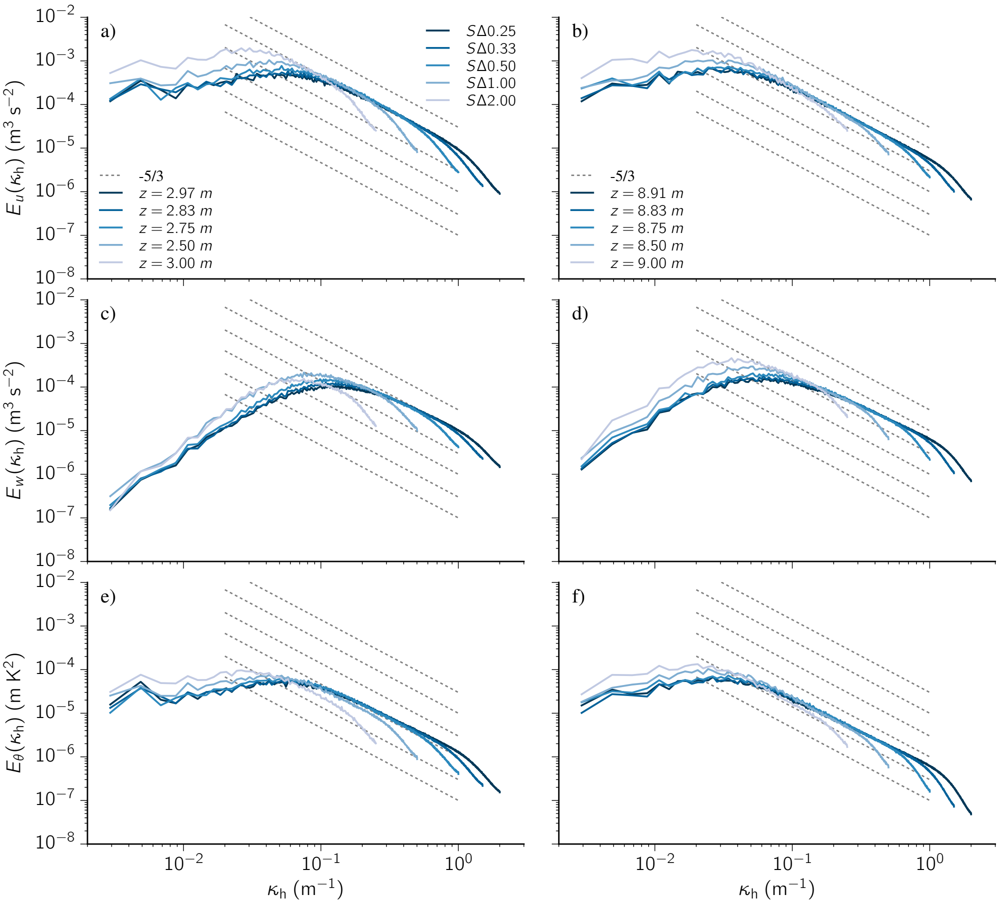

*Figure 5.8: Radially averaged horizontal spectra of the zonal wind component (top), vertical velocity (middle) and potential temperature (bottom), at approximately 3 m height (left) and 9 m height (right), averaged over the period 09:00 UTC - 09:30 UTC.*

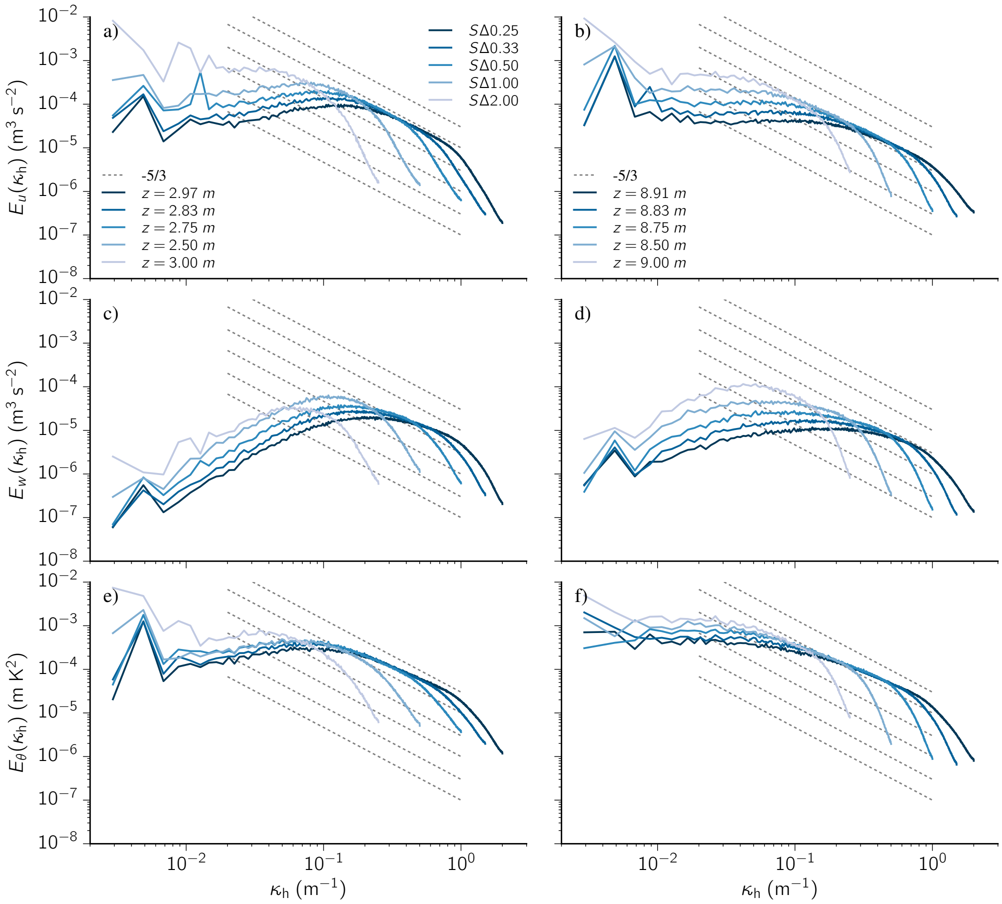

*Figure 5.9: As figure 5.8, averaged over the period 13:30 UTC - 14:00 UTC.*

ences are introduced gradually over time, and a study of the TKE and variance budgets (comparing the production, destruction and transport terms) did not provide an explanation of these differences.

Compared to the spectra obtained over the period 09:00-09:30 UTC – where the $S\Delta2.00$ case showed a -5/3 slope in the inertial subrange over more than a factor 10 difference in spatial scales – this scaling is less clear between 13:30-14:00 UTC. Some variables, like the $u$ wind component at 3 m height, still exhibit the -5/3 slope, but over a reduced range of spatial scales. Most other variables show a widened (or even absent) peak in the spectra, with slopes of less than -5/3 towards the higher wave numbers.

## 5.4 Summary, conclusions and outlook

This chapter presented some first results for the GABLS4 LES intercomparison case, a case mostly focussed on a stable boundary layer (SBL) over the Antarctic. Compared to earlier LES studies of the SBL, which mostly addressed weakly stable conditions, the GABLS4 case is in the transitionally stable regime, where turbulent intensities rapidly decrease with increasing stability. As a result the case is only weakly turbulent, with turbulence kinetic energy (TKE) values which are an order of magnitude less than observed in, for example, the weakly stable GABLS1 LES intercomparison. As the results from LES intercomparisons are often used to validate or develop e.g. models based on the Reynolds averaged Navier-Stokes equations, it is important to know if LES can produce valid results for such weakly stable conditions.

To reduce the substantial computational costs, we first studied the impact of simulating only part of the experiment instead of the full 24 hour period, and tested two methods for initializing such an experiment: either from horizontally homogeneous conditions with random perturbations, or from a temperature field interpolated from a lower resolution experiment. Using a realistic initial temperature field has proven to be beneficial in reducing the time required for the experiments to become turbulent. Next, a sensitivity study on resolution was performed, with grid spacing ranging from $2\times2\times2$ m$^3$ down to $0.25\times0.25\times0.25$ m$^3$. Although some statistics, like the horizontally averaged profiles of potential temperature and wind, converged at the highest resolutions, second order moments like the heat and momentum fluxes didn't converge. An analysis of spectra of the velocity components and potential temperature showed a similar behavior: where at the beginning of the night (when the SBL is still weakly stable) the characteristics of turbulence at the largest scales are independent of details at the smallest scales, this is no longer the case when the atmosphere becomes more strongly stratified.

These results demonstrate the difficulty in obtaining valid LES results for such a weakly turbulent case, not only at the originally proposed intercomparison resolution of $5\times5\times2$ m$^3$ or $2\times2\times2$ m$^3$, but even at grid spacings which are roughly a factor ten finer. However, we should note that this work only considered results obtained with the (non-dynamic) Smagorinsky scheme. Over the years more advanced sub-grid scale models have been developed, like a variety of dynamic Smagorinsky schemes (e.g. Porté-Agel et al., 2000; Bou-Zeid et al., 2005) or the stretched-vortex scheme (Chung and Matheou, 2014). The dynamic Smagorinsky schemes don't require an ad-hoc tuning of the Smagorinsky constant and turbulent Prandtl number, which might be beneficial for cases like GABLS4, which contain both convective and stable conditions. Several participants of the GABLS4 intercomparison are using dynamic Smagorinsky or stretched-vortex sub-grid schemes, and a future comparison with their results would be interesting.

# Chapter VI

# Summary and conclusions

Large-eddy simulation (LES) is slowly moving from highly idealized experiment to more realistic setups, including real-life experiments (hindcasts) of full diel cycles of convection on domains as large as the Netherlands (hundreds of kilometers) or Germany (thousand kilometers). In contrast to more idealized setups, such experiments encompass a wide variety of processes, ranging from large deep convective systems down to small scale shear-driven turbulence at night. Explicitly resolving all the relevant turbulent processes is currently not feasible, and will, in all likelihood, remain unattainable for the next few decades.

For studies focused on convection, in which details of the stable boundary layer (SBL) are of secondary importance, a logical solution is to use a resolution which is sufficient to accurately represent daytime convection but insufficient to resolve the SBL, potentially sacrificing the representation of the latter. Although unwanted, such sacrifices are unfortunately necessary given the impossible computational demands necessary to resolve the SBL. This methodology, in which parts of the LES experiments are – strictly speaking – no longer LES, could be justified, but only if the poorly resolved parts of the experiments (the SBL) don't influence the periods of interest (daytime convection).

In this thesis we addressed whether this is the case, i.e. the question if a poorly resolved SBL is badly represented in LES, and if so, whether this can influence the following day of convection. In addition to using LES itself, observations from three sites in northwest Europe were used to characterize the nocturnal conditions, and we developed a conceptual model to assist us in the understanding of the observations and results.

In Chapter 3 we started by addressing our main research question from the perspective of turbulent mixing. LES owes its main skill to the fact that most turbulence is explicitly resolved; a skill which is likely to degrade when the chosen grid spacing is too coarse to resolve the turbulent eddies. Using observations from Hamburg and Cabauw, we characterized the summertime SBL, and setup a number of LES experiments of diel cycles of convection, covering the typical conditions in our area of interest. Using a sensitivity study on resolution, with grid spacing ranging from $\Delta$ = 3.125 m (isotropic) – with which we can resolve turbulence in the SBL – to $\Delta = 100 \times 100 \times 25$ m$^3$ – which is clearly insufficient to resolve the SBL – we studied the impact of resolved turbulence at night on the development of the SBL, and convection the following day. At grid spacings as coarse as $100 \times 100 \times 25$ m$^3$, turbulence at night is unresolved, resulting in relative biases in the NBL depth of 100% - 120%, and absolute biases in the bulk NBL temperature of 2 K - 3 K. These biases are the results of an overestimation of vertical mixing by the Smagorinsky sub-grid model, and to a lesser extent, caused by interactions between the SBL and land surface. Despite the large nocturnal biases, the impact on the following day of convection was shown to be limited, with maximum biases in the afternoon mixed-layer depth and temperature of approximately 100 m and 0.5 K, respectively.

In Chapter 4 we extended the work from Chapter 3, by considering the role that moisture might play. The typical model biases observed in Chapter 3 consisted of an overestimation of the SBL depth, resulting in positive temperature biases near the surface, and negative temperature biases near or above the SBL top. Such biases could cause secondary biases related to moisture, like the absence of fog/mist occurring in reality, or a spurious formation of low clouds near/above the NBL top. When interacting with radiation, this could further distort the SBL development, and possibly influence the following day of convection. Using observations from Hamburg, Karlsruhe, and Cabauw, we first studied the moisture characteristics of nights in between convective days. Even though we focussed on summertime conditions, the median early morning (sunrise) relative humidities at 2 m height were still as high as 94-95% for Cabauw and Karlsruhe, although only Cabauw actually experienced saturated conditions (shallow layers of mist) approximately once every three nights. With height, the relative humidity decreases in the SBL, but nonetheless conditions at 200 m height are frequently within 2 K from saturation. Using a newly developed conceptual model, which given the total SBL cooling and depth, can reproduce the vertical structure of the SBL, we studied if overestimating vertical mixing could cause a spurious formation of clouds. The results showed convincingly that this is unlikely to happen: although there are conditions where overestimating the SBL depth increases the relative humidity, this only occurs for conditions which are far from saturation.

*Even though the SBL is poorly represented in (low-resolution) LES, the poor representation of turbulence in the SBL does not significantly influence the following day of convection. In addition, a spurious deepening of the SBL, caused by poorly representing vertical mixing, is unlikely to cause a spurious formation of low clouds. For LES studies of complete diel cycles – which focus on daytime convection, and in which a correct representation of the nocturnal conditions is less important – the use of a resolution which is appropriate for daytime convection is sufficient, opening up the possibility to perform LES experiments on domains as large as e.g. Germany.*

The studies from Chapter 3 and 4 focussed on the typical European nocturnal conditions, not the extreme. For such (mostly) weakly stable conditions, it is attainable to obtain valid LES results, as has been demonstrated before in literature. However, more strongly stable conditions, like the transitionally stable regime – where with increasing stability the buoyancy stratification rapidly starts suppressing turbulence – or even the strongly stable regime – where turbulence becomes very weak, intermittent, or absent – also occur over Europe. Perhaps because of the great computational demands, or the inability of LES to reproduce such conditions, these more strongly stable conditions have received less attention in literature. In Chapter 5 we studied a transitionally stable boundary layer with LES: the GABLS4 intercomparison case, situated over the Antarctic. Using a sensitivity study on resolution, with grid spacings varying from $5 \times 5 \times 2$ m$^3$ to $0.25 \times 0.25 \times 0.25$ m$^3$, we demonstrated the difficulties in simulating a case as weakly turbulent as GABLS4. Even at grid spacings of $\ll$1 m, the results still depend on resolution, and – somewhat counter intuitively – with increasing resolution the SBL becomes less turbulent.

*For stronger stably stratified conditions, with consequently weaker turbulence characteristics, it is still challenging to obtain valid results using a traditional (non-dynamic Smagorinsky diffusion) LES setup, and the results of such experiments should be interpreted or used with caution. As in such a setup a grid spacing of $\mathcal{O}$(0.1 m) seems to be required, more advanced LES techniques, like an improved representation of the sub-grid scale processes, might be beneficial to reduce the computational costs, and the already significant difference in the grid spacing required to represent daytime convection and the nighttime boundary layer.*

# Appendices

## A.1 Sampling criteria clear nights

In Chapter 3, we sample clear nights based on the difference in incoming longwave radiation ($LW_{\mathrm{in}}$) between measurements and a theoretical value calculated using the 2 m temperature ($T_{\mathrm{2m}}$) and Stefan-Boltzmann's law. In the presence (absence) of clouds the difference $\delta Q = \sigma T_{\mathrm{2m}}^4 - LW_{\mathrm{in}}$ (with $\sigma = 5.67\times10^8$ W m$^{-2}$ K$^{-4}$) is expected to be small (large). The threshold for this difference, and the mis-sampling that it introduces, was studied using cloud cover observations from Cabauw as shown in Fig. A.1. For samples with a large observed cloud cover, $\delta Q$ is typically less than 50 $W\ m^{-2}$, while for clear nights the majority of the samples have $\delta Q$ larger than 50 $W\ m^{-2}$. Using a threshold $\delta Q \geq 50$ $W\ m^{-2}$ to sub-sample the clear nights, and defining a cloud cover of ≥ 30% as cloudy, results in a mis-sampling of 11% (dashed area).

## A.2 Sampling criteria of nights in between convective days

In Chapter 4, we sample the nights in between convective days by considering the observed shortwave incoming radiation over a period of 5 h to 3 h before sunset, and 3 h to 9 h after sunrise, and only select nights where the mean incoming shortwave radiation over both periods is more than 40% of its theoretically maximum value (Stull, 1988, p255-258). The period after sunrise was deliberately chosen longer, as with a shorter averaging period a number of convective days which started with clouds were filtered out. In addition, based on a visual inspection of the sampling, nights with a mean surface pressure tendency of less than (i.e., more negative) -20 pa h$^{-1}$ are excluded, as those nights were typically dominated by frontal passages.

## A.3 Description simplified land-surface model

The parameterization of the land-surface model (LSM) from Chapter 3 is described here, and not in the model description in Chapter 2, as the implementation is quite specific for the cases from that chapter. The LSM is inspired by the ECMWF IFS documentation (ECMWF, 2011), and equations or section numbers prepended with "IFS"

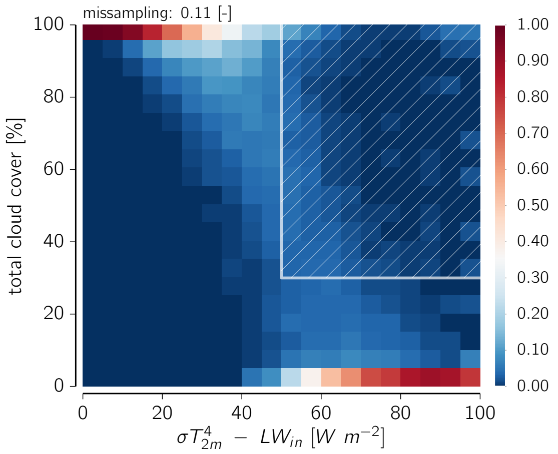

*Figure A.1: 2D histogram of the measured cloud fraction versus* $\delta Q = \sigma T_{2\text{m}}^4 - LW_{\text{in}}$*. For each vertical bin the probability is normalized, i.e. each column has a total probability of 1. The hashed square indicates the mis-sampling (see text).*

refer to the latter document. In the absence of moisture, the surface energy balance (SEB) is defined as:

$$Q_{\text{net}} = LW_{\text{in}} - LW_{\text{out}} + SW_{\text{in}} - SW_{\text{out}} = H + G, \tag{A.1}$$

with $Q_{\text{net}}$ the net surface radiation, $LW$ and $SW$ the longwave and shortwave, incoming (in) and outgoing (out) radiative fluxes, and $H$ and $G$ the surface sensible and soil heat flux. The different radiative components are prescribed or parameterized. The longwave components are defined as $LW_{\text{in}} = 300\ W\ m^{-2}$ and $LW_{\text{out}} = \sigma T_{\text{s}}^4$, with $T_{\text{s}}$ the surface (skin) temperature. Shortwave radiation is parameterized using the geographical location, time and day of year (Stull, 1988, p255-258) using $48^o$N, Julian date 196 starting at 1500 UTC), and a prescribed surface albedo. With the latent heat flux excluded from the SEB (Eq. A.1), the surface albedo was increased to 0.65 to prevent unrealistic daytime sensible heat fluxes. The resulting heat flux, as shown in Fig. 3.3, is representative for both the Cabauw and Hamburg site. With the surface fluxes defined as:

$$H = \frac{\rho c_{\text{p}}}{r_a}(\theta_{\text{s}} - \theta_{\text{a}}), \tag{A.2}$$

$$G = \Lambda_{\text{sk}}(T_{\text{s}} - T_{\text{soil}}), \tag{A.3}$$

with $\rho$ the (surface) air density, $c_\mathrm{p}$ the specific heat capacity of air at constant pressure (1005 J kg$^{-1}$ K$^{-1}$), $r_\mathrm{a}$ the aerodynamic resistance, $\theta_\mathrm{a}$ the potential temperature at the lowest model level, $T_\mathrm{s}$ ($\theta_\mathrm{s}$) the surface (potential) temperature, $\Lambda_\mathrm{sk}$ the thermal diffusivity of the skin layer, and $T_\mathrm{soil}$ the temperature of the top soil layer. The aerodynamic resistance is defined as $1/r_\mathrm{a} = C_\mathrm{H}\,|U|$, with $|U|$ the absolute wind speed at the lowest model level, and $C_\mathrm{H}$ the transfer coefficient of heat (Eq. IFS-3.15). The latter is calculated using the integrated stability functions as defined in Eq. IFS-3.20 and IFS-3.22, calculating the Obukhov length as defined in Section IFS-3.2.3.

Assuming that the heat capacity of the skin layer is zero, the surface temperature can explicitly be solved from Eq. A.1-A.3. Four soil layers are used with their midpoints at {0.035, 0.175, 0.64 and 1.5} m depth, with initial temperatures (gradient typical for the study area at hand) of {291.0, 290.7, 289.8, 287.9} degrees, respectively. Evolution of the soil temperature follows a diffusion equation (Eq. IFS-8.54):

$$(\rho C)_\mathrm{soil}\frac{\partial T_\mathrm{soil}}{\partial t} = \lambda_\mathrm{T}\frac{\partial^2 T_\mathrm{soil}}{\partial z^2} \tag{A.4}$$

with $(\rho C)_\mathrm{soil} = 2.19\times10^6$ J m$^{-3}$ K$^{-1}$ and $\lambda_\mathrm{T}$ a prescribed thermal diffusivity of 1.255 W m$^{-1}$ K$^{-1}$. The latter value is representative for a loamy soil at a volumetric soil moisture content of 0.247 m$^3$ m$^{-3}$.

## A.4 Derivation relative humidity budget equation

Assuming an air density which is constant with height and equal to the density at the surface, $\theta \approx T + (g/c_\mathrm{p})z$ (with $g$ the gravitational acceleration and $c_\mathrm{p}$ the isobaric specific heat of air), and a surface pressure which is constant in time and equals the reference pressure ($10^5$ pa), the change in absolute temperature at the surface (subscript s) and $\alpha z_\mathrm{n}$ (subscript t) changes with an increasing NBL depth $z_\mathrm{n}$ as:

$$\frac{\partial T_\mathrm{s}}{\partial z_\mathrm{n}} = -\frac{\Delta Q}{\alpha z_\mathrm{n}^2}, \tag{A.5}$$

$$\frac{\partial T_\mathrm{t}}{\partial z_\mathrm{n}} \approx -\frac{\Delta Q}{z_\mathrm{n}^2} - \frac{\alpha g}{c_\mathrm{p}}. \tag{A.6}$$

In general, the change in relative humidity (RH) with height equals:

$$\frac{\partial \mathrm{RH}}{\partial z} = \frac{\partial}{\partial z}\left(\frac{q}{q_\mathrm{s}}\right) = \frac{1}{q_\mathrm{s}}\frac{\partial q}{\partial z} - \frac{\mathrm{RH}}{q_\mathrm{s}}\frac{\partial q_\mathrm{s}}{\partial z}, \tag{A.7}$$

where under well-mixed conditions, the first term on the RHS – containing the vertical gradient of $q$ – is zero. The change in the saturation specific humidity ($q_\mathrm{s}$) with height can be approximated by:

$$q_\mathrm{s} \approx \frac{\epsilon e_\mathrm{s}}{p}, \tag{A.8}$$

$$\frac{\partial q_\mathrm{s}}{\partial z} \approx \frac{\epsilon}{p}\frac{\partial e_\mathrm{s}}{\partial T}\frac{\partial T}{\partial z} - \frac{q_\mathrm{s}}{p}\frac{\partial p}{\partial z} \tag{A.9}$$

$$\frac{\partial \mathrm{RH}}{\partial z} = -\frac{\mathrm{RH}}{q_\mathrm{s}}\frac{\epsilon}{p}\frac{\partial e_\mathrm{s}}{\partial T}\frac{\partial T}{\partial z} + \frac{\mathrm{RH}}{p}\frac{\partial p}{\partial z}, \tag{A.10}$$

where $\epsilon$ is the ratio between the gas constant for dry air ($R_\mathrm{d}$) and the gas constant for water vapor ($R_\mathrm{v}$), and $e_\mathrm{s}$ is the saturation vapor pressure. At the surface, the last term of Eq. A.10 is zero, and using Eq. A.5 the tendency can be expressed as:

$$\frac{\partial \mathrm{RH_s}}{\partial z_\mathrm{n}} = \frac{\mathrm{RH}}{q_\mathrm{s}}\frac{\epsilon}{p}\frac{\partial e_\mathrm{s}}{\partial T}\frac{\Delta Q}{\alpha z_\mathrm{n}^2}. \tag{A.11}$$

At the height $\alpha z_\mathrm{n}$, two terms contribute to the change of temperature (Eq. A.6), and assuming $\partial p/\partial z = -\rho g$, the tendency can be written as:

$$\frac{\partial \mathrm{RH_t}}{\partial z_\mathrm{n}} \approx \frac{\mathrm{RH}}{q_\mathrm{s}}\frac{\epsilon}{p}\frac{\partial e_\mathrm{s}}{\partial T}\frac{\Delta Q}{z_\mathrm{n}^2} + \frac{\mathrm{RH}}{q_\mathrm{s}}\frac{\epsilon}{p}\frac{\partial e_\mathrm{s}}{\partial T}\frac{\alpha g}{c_\mathrm{p}} - \frac{\mathrm{RH}}{p}\alpha\rho g \tag{A.12}$$

## A.5 Details observation sites

The measurement sites at Hamburg (Germany), Karlsruhe (Germany) and Cabauw (Netherlands) provide tower observations at different heights, which are summarized (for the variables used in this thesis) in Table A.1.

*Table A.1: Overview of the measurement heights at the towers of Hamburg, Karlsruhe and Cabauw.*

|  | **z (m)** | **2** | **10** | **50** | **70** | **110** | **175** | **250** | **280** |
|---|---|---|---|---|---|---|---|---|---|
| Hamburg | ***T*** | x | x | x | x | x | x | x | x |
|  | **RH / *T*d** | x | x | x |  | x | x | x | x |
|  | ***U*** |  | x | x |  | x | x | x | x |
|  | ***U*-direction** |  | x | x |  | x | x | x | x |

|  | **z (m)** | **2** | **10** | **20** | **30** | **40** | **50** | **60** | **80** | **100** | **130** | **160** | **200** |
|---|---|---|---|---|---|---|---|---|---|---|---|---|---|
| Karlsruhe | ***T*** | x | x |  | x |  |  | x |  | x | x | x | x |
|  | **RH / *T*d** | x | x |  | x |  |  |  |  | x |  |  | x |
|  | ***U*** | x |  | x | x | x | x | x | x | x | x | x | x |
|  | ***U*-direction** |  |  |  |  | x |  | x | x | x |  | x | x |

|  | **z (m)** | **2** | **10** | **20** | **40** | **80** | **140** | **200** |
|---|---|---|---|---|---|---|---|---|
| Cabauw | ***T*** | x | x | x | x | x | x | x |
|  | **RH / *T*d** | x | x | x | x | x | x | x |
|  | ***U*** | x | x | x | x | x | x | x |
|  | ***U*-direction** | x | x | x | x | x | x | x |

# References

Ackerman, A. S., Vanzanten, M. C., Stevens, B., Savic-Jovcic, V., Bretherton, C. S., Chlond, A., Golaz, J.-C., Jiang, H., Khairoutdinov, M., Krueger, S. K., et al. (2009). Large-eddy simulations of a drizzling, stratocumulus-topped marine boundary layer. *Mon. Wea. Rev.*, 137(3):1083–1110.

Anber, U., Gentine, P., Wang, S., and Sobel, A. H. (2015). Fog and rain in the amazon. *Proceedings of the National Academy of Sciences*, 112(37):11473–11477.

Angevine, W. M., Baltink, H. K., and Bosveld, F. C. (2001). Observations of the morning transition of the convective boundary layer. *Bound.-Layer Meteor.*, 101(2):209–227.

Ansorge, C. and Mellado, J. P. (2014). Global intermittency and collapsing turbulence in the stratified planetary boundary layer. *Bound.-Layer Meteor.*, 153(1):89–116.

Baldauf, M., Seifert, A., FÃűrstner, J., Majewski, D., Raschendorfer, M., and Reinhardt, T. (2011). Operational convective-scale numerical weather prediction with the cosmo model: Description and sensitivities. *Mon. Wea. Rev.*, 139(12):3887–3905.

Bannon, P. R. (1996). On the anelastic approximation for a compressible atmosphere. *J. Atmos. Sci.*, 53(23):3618–3628.

Basu, S., Holtslag, A. A., Wiel, B. J. H., Moene, A. F., and Steeneveld, G.-J. (2008a). An inconvenient "truth" about using sensible heat flux as a surface boundary condition in models under stably stratified regimes. *Acta Geop.*, 56(1):88–99.

Basu, S., Vinuesa, J.-F., and Swift, A. (2008b). Dynamic LES modeling of a diurnal cycle. *J. Appl. Meteor.*, 47(4):1156–1174.

Beare, R. J. and Macvean, M. K. (2004). Resolution sensitivity and scaling of large-eddy simulations of the stable boundary layer. *Bound.-Layer Meteor.*, 112(2):257–281.

Beare, R. J., Macvean, M. K., Holtslag, A. A. M., Cuxart, J., Esau, I., Golaz, J. ., Jimenez, M. A., Khairoutdinov, M., Kosovic, B., Lewellen, D., Lund, T. S., Lundquist, J. K., McCabe, A., Moene, A. F., Noh, Y., Raasch, S., and Sullivan, P. (2006). An intercomparison of large-eddy simulations of the stable boundary layer. *Bound.-Layer Meteor.*, 118(2):247–272.

Bechtold, P., Krueger, S. K., Lewellen, W., Van Meijgaard, E., Moeng, C., Randall, D., Van Ulden, A., and Wang, S. (1996). Modeling a stratocumulus-topped pbl: Intercomparison among different one-dimensional codes and with large eddy simulation. *Bull. Amer. Meteor. Soc.*, 77(9):2033–2042.

Bou-Zeid, E., Meneveau, C., and Parlange, M. (2005). A scale-dependent lagrangian dynamic model for large eddy simulation of complex turbulent flows. *Physics of Fluids*, 17(2):1–18.

Brown, A. R., Cederwall, R. T., Chlond, A., Duynkerke, P. G., Golaz, J. ., Khairoutdinov, M., Lewellen, D. C., Lock, A. P., Macvean, M. K., Moeng, C. ., Neggers, R. A. J., Siebesma, A. P., and Stevens, B. (2002). Large-eddy simulation of the diurnal cycle of shallow cumulus convection over land. *Quart. J. R. Meteorol. Soc.*, 128:1075–1093.

Brown, A. R., Derbyshire, S., and Mason, P. J. (1994). Large-eddy simulation of stable atmospheric boundary layers with a revised stochastic subgrid model. *Quart. J. R. Meteorol. Soc.*, 120(520):1485–1512.

Brümmer, B., Lange, I., and Konow, H. (2012). Atmospheric boundary layer measurements at the 280 m high Hamburg weather mast 1995-2011: mean annual and diurnal cycles. *Meteorol. Zeitschrift*, 21(4):319–335.

Bryan, G. H., Wyngaard, J. C., and Fritsch, J. M. (2003). Resolution Requirements for the Simulation of Deep Moist Convection. *Mon. Wea. Rev.*, 131:2394–2416.

Businger, J. (1988). A note on the businger-dyer profiles. In *Topics in Micrometeorology. A Festschrift for Arch Dyer*, pages 145–151.

Carpenter, M. H. and Kennedy, C. A. (1994). Fourth-order 2N-storage Runge-Kutta schemes. *Tech. Rep. TM-109112, NASA Langley Research Center.*

Chung, D. and Matheou, G. (2014). Large-Eddy Simulation of Stratified Turbulence. Part I: A Vortex-Based Subgrid-Scale Model. *J. Atmos. Sci.*

Cuxart, J., Holtslag, A. A., Beare, R. J., Bazile, E., Beljaars, A., Cheng, A., Conangla, L., Ek, M., Freedman, F., Hamdi, R., et al. (2006). Single-column model intercomparison for a stably stratified atmospheric boundary layer. *Bound.-Layer Meteor.*, 118(2):273–303.

de Roode, S. R., Bosveld, F. C., and Kroon, P. S. (2010). Dew formation, eddy-correlation latent heat fluxes, and the surface energy imbalance at Cabauw during stable conditions. *Bound.-Layer Meteor.*, 135(3):369–383.

Deardorff, J. W. (1970). A numerical study of three-dimensional turbulent channel flow at large reynolds numbers. *J. Fluid Mech.*, 41(02):453–480.

Deardorff, J. W. (1972). Numerical investigation of neutral and unstable planetary boundary layers. *J. Atmos. Sci.*, 29(1):91–115.

Deardorff, J. W. (1980). Stratocumulus-capped mixed layers derived from a three dimensional model. *Bound.-Layer Meteor.*, (18):495–527.

Del Alamo, J. C., Jiménez, J., Zandonade, P., and Moser, R. D. (2004). Scaling of the energy spectra of turbulent channels. *J. Fluid Mech.*, 500:135–144.

Dipankar, A., Stevens, B., Heinze, R., Moseley, C., Zängl, G., Giorgetta, M., and Brdar, S. (2015). Large eddy simulation using the general circulation model icon. *Adv. Model. Earth Syst.*, 7(3):963–986.

Duynkerke, P. G. (1999). Turbulence, radiation and fog in Dutch stable boundary layers. *Bound.-Layer Meteor.*, 90(3):447–477.

ECMWF (2011). IFS documentation Cy37r2 - part IV: Physical processes. Technical Report Cy37r2, European Center for Medium range Weather Forecasting.

Edwards, J. (2009). Radiative processes in the stable boundary layer: Part I. radiative aspects.

*Bound.-Layer Meteor.*, 131(2):105–126.

Einaudi, F. and Finnigan, J. (1993). Wave-turbulence dynamics in the stably stratified boundary layer. *J. Atmos. Sci.*, 50(13):1841–1864.

Ek, M. and Mahrt, L. (1994). Daytime evolution of relative humidity at the boundary layer top. *Mon. Wea. Rev.*, 122:2709–2721.

Fernando, H. J. S. and Weil, J. C. (2010). Whither the stable boundary layer? *Bull. Amer. Meteor. Soc.*, 91(11):1475–1484.

Garcia, J. R. and Mellado, J. P. (2014). The two-layer structure of the entrainment zone in the convective boundary layer. *J. Atmos. Sci.*, 71(6):1935–1955.

Garratt, J. R. and Brost, R. A. (1981). Radiative cooling effects within and above the nocturnal boundary layer. *J. Atmos. Sci.*, 38(12):2730–2746.

Grachev, A. A., Andreas, E. L., Fairall, C. W., Guest, P. S., and Persson, P. O. G. (2007). On the turbulent prandtl number in the stable atmospheric boundary layer. *Bound.-Layer Meteor.*, 125(2):329–341.

Högström, U. (1988). Non-dimensional wind and temperature profiles in the atmospheric surface layer: A re-evaluation. In *Topics in Micrometeorology. A Festschrift for Arch Dyer*, pages 55–78. Springer.

Hohenegger, C. and Stevens, B. (2013). Preconditioning deep convection with cumulus congestus. *J. Atmos. Sci.*, 70(2):448–464.

Holloway, C. E., Woolnough, S. J., and Lister, G. M. S. (2012). Precipitation distributions for explicit versus parametrized convection in a largeâĂŘdomain highâĂŘresolution tropical case study. *Quart. J. R. Meteorol. Soc.*, 138(668):1692–1708.

Holtslag, A. and De Bruin, H. (1988). Applied modeling of the nighttime surface energy balance over land. *J. Appl. Meteor.*, 27(6):689–704.

Holtslag, A. A. M., Steeneveld, G. J., and Wiel, B. J. H. (2007). Role of land-surface temperature feedback on model performance for the stable boundary layer. In Baklanov, A. and Grisogono, B., editors, *Atmospheric Boundary Layers*, pages 205–220. Springer New York.

Holtslag, A. A. M., Svensson, G., Baas, P., Basu, S., Beare, B., Beljaars, A. C. M., Bosveld, F. C., Cuxart, J., Lindvall, J., Steeneveld, G. J., TjernstrÃűm, M., and Van De Wiel, B. J. H. (2013). Stable atmospheric boundary layers and diurnal cycles: Challenges for weather and climate models. *Bull. Amer. Meteor. Soc.*, 94(11):1691–1706.

Honnert, R., Masson, V., and Couvreux, F. (2011). A diagnostic for evaluating the representation of turbulence in atmospheric models at the kilometric scale. *J. Atmos. Sci.*, 68:3112–3131.

Huang, H.-Y., Stevens, B., and Margulis, S. (2008). Application of dynamic subgrid-scale models for large-eddy simulation of the daytime convective boundary layer over heterogeneous surfaces. *Bound.-Layer Meteor.*, 126(3):327–348.

Huang, J. and Bou-Zeid, E. (2013). Turbulence and vertical fluxes in the stable atmospheric boundary layer. part i: a large-eddy simulation study. *J. Atmos. Sci.*, 70(6):1513–1527.

Jakob, C. (2010). Accelerating progress in global atmospheric model development through improved parameterizations: Challenges, opportunities, and strategies. *Bull. Amer. Meteor. Soc.*, 91(7):869–875.

Kalthoff, N. and Vogel, B. (1992). Counter-current and channelling effect under stable stratification in the area of karlsruhe. *Theor. and Appl. Climatol.*, 45(2):113–126.

Kleissl, J., Kumar, V., Meneveau, C., and Parlange, M. B. (2006). Numerical study of dynamic smagorinsky models in large-eddy simulation of the atmospheric boundary layer: Validation in stable and unstable conditions. *Water Resour. Res.*, 42(SUPPL.).

Kondo, J., Kuwagata, T., and Haginoya, S. (1989). Heat budget analysis of nocturnal cooling and daytime heating in a basin. *J. Atmos. Sci.*, 46(19):2917–2933.

Kosovic, B. and Curry, J. A. (2000). A large eddy simulation study of a quasi-steady, stably stratified atmospheric boundary layer. *J. Atmos. Sci.*, 57(8):1052–1068.

Kumar, V., Kleissl, J., Meneveau, C., and Parlange, M. (2006). Large-eddy simulation of a diurnal cycle of the atmospheric boundary layer: Atmospheric stability and scaling issues. *Water Resour. Res.*, 42(SUPPL.).

Kumar, V., Svensson, G., Holtslag, A. A. M., Meneveau, C., and Parlange, M. B. (2010). Impact of surface flux formulations and geostrophic forcing on large-eddy simulations of diurnal atmospheric boundary layer flow. *J. Appl. Meteor.*, 49(7):1496–1516.

Lévêque, E., Toschi, F., Shao, L., and Bertoglio, J.-P. (2007). Shear-improved smagorinsky model for large-eddy simulation of wall-bounded turbulent flows. *J. Fluid Mech.*, 570:491–502.

Lilly, D. K. (1962). On the numerical simulation of buoyant convection. *Tellus*, 14(2):148–172.

Lilly, D. K. (1966). The representation of small-scale turbulence in numerical simulation experiments. Technical Report NCAR manuscript No. 281, National Center for Atmospheric Research.

Lilly, D. K. (1968). Models of cloud-topped mixed layers under a strong inversion. *Quart. J. R. Meteorol. Soc.*, 94(401):292–309.

Luebke, D. (2008). Cuda: Scalable parallel programming for high-performance scientific computing. In *Biomedical Imaging: From Nano to Macro, 2008. ISBI 2008. 5th IEEE International Symposium on*, pages 836–838. IEEE.

Mahrt, L. (1998). Nocturnal boundary-layer regimes. *Bound.-Layer Meteor.*, 88(2):255–278.

Mason, P. J. and Derbyshire, S. H. (1990). Large-eddy simulation of the stably-stratified atmospheric boundary layer. *Bound.-Layer Meteor.*, 53(1-2):117–162.

Mason, P. J. and Thomson, D. J. (1992). Stochastic backscatter in large-eddy simulations of boundary layers. *J. Fluid Mech.*, 242:51–78.

Mauritsen, T. and Svensson, G. (2007). Observations of stably stratified shear-driven atmospheric turbulence at low and high richardson numbers. *J. Atmos. Sci.*, 64(2):645–655.

Mauritsen, T., Svensson, G., Zilitinkevich, S. S., Esau, I., Enger, L., and Grisogono, B. (2007). A total turbulent energy closure model for neutrally and stably stratified atmospheric boundary layers. *J. Atmos. Sci.*, 64(11):4113–4126.

Michalakes, J. and Vachharajani, M. (2008). Gpu acceleration of numerical weather prediction. *Parallel Processing Letters*, 18(04):531–548.

Mielikainen, J., Huang, B., Huang, H.-L. A., and Goldberg, M. D. (2012). Gpu acceleration of the updated goddard shortwave radiation scheme in the weather research and forecasting (wrf) model. *Selected Topics in Applied Earth Observations and Remote Sensing*, 5(2):555–562.

Miyamoto, Y., Kajikawa, Y., Yoshida, R., Yamaura, T., Yashiro, H., and Tomita, H. (2013). Deep moist atmospheric convection in a subkilometer global simulation. *Geophys. Res. Lett.*, 40(18):4922–4926.

Moeng, C.-H. (1984). A large-eddy-simulation model for the study of planetary boundary-layer turbulence. *J. Atmos. Sci.*, 41(13):2052–2062.

Moeng, C.-H. and Wyngaard, J. C. (1988). Spectral analysis of large-eddy simulations of the convective boundary layer. *J. Atmos. Sci.*, 45(23):3573–3587.

Monin, A. and Obukhov, A. (1954). Basic laws of turbulent mixing in the surface layer of the atmosphere. *Contrib. Geophys. Inst. Acad. Sci. USSR*, 151:163–187.

Moser, R. D., Kim, J., and Mansour, N. N. (1999). Direct numerical simulation of turbulent channel flow up to re= 590. *Phys. Fluids*, 11(4):943–945.

Naumann, A. K. and Seifert, A. (2015). A lagrangian drop model to study warm rain microphysical processes in shallow cumulus. *Adv. Model. Earth Syst.*, 7(3):1136–1154.

Neggers, R. A. J., Siebesma, A. P., and Heus, T. (2012). Continuous single-column model evaluation at a permanent meteorological supersite. *Bull. Amer. Meteor. Soc.*, 93(xx):1389–1400.

Ogura, Y. and Phillips, N. A. (1962). Scale Analysis of Deep and Shallow Convection in the Atmosphere. *J. Atmos. Sci.*, 19(2):173–179.

Paulson, C. A. (1970). The mathematical representation of wind speed and temperature profiles in the unstable atmospheric surface layer. *J. Appl. Meteor.*, 9(6):857–861.

Pincus, R. and Stevens, B. (2009). Monte Carlo Spectral Integration: a Consistent Approximation for Radiative Transfer in Large Eddy Simulations. *Adv. Model. Earth Syst.*, 1(1).

Pincus, R. and Stevens, B. (2013). Paths to accuracy for radiation parameterizations in atmospheric models. *Adv. Model. Earth Syst.*, 5(2):225–233.

Pino, D., Vilà-Guerau de Arellano, J., and Duynkerke, P. G. (2003). The contribution of shear to the evolution of a convective boundary layer. *J. Atmos. Sci.*, 60(16):1913–1926.

Porté-Agel, F., Meneveau, C., and Parlange, M. B. (2000). A scale-dependent dynamic model for large-eddy simulation: application to a neutral atmospheric boundary layer. *Journal of Fluid Mechanics*, 415:261–284.

Reynolds, O. (1895). On the dynamical theory of incompressible viscous fluids and the determination of the criterion. *Royal Society of London Philosophical Transactions Series A*, 186:123–164.

Richardson, H., Basu, S., and Holtslag, A. (2013). Improving stable boundary-layer height estimation using a stability-dependent critical bulk Richardson number. *Bound.-Layer Meteor.*, 148(1):93–109.

Rieck, M., Hohenegger, C., and van Heerwaarden, C. C. (2014). The influence of land surface heterogeneities on cloud size development. *Mon. Wea. Rev.*, 142(10):3830–3846.

Schalkwijk, J., Griffith, E. J., Post, F. H., and Jonker, H. J. (2012). High-performance simulations of turbulent clouds on a desktop pc. *Bull. Amer. Meteor. Soc.*, 93(3):307.

Schalkwijk, J., Jonker, H. J., Siebesma, A. P., and Bosveld, F. C. (2015a). A year-long large-eddy simulation of the weather over cabauw: An overview. *Mon. Wea. Rev.*, 143(3):828–844.

Schalkwijk, J., Jonker, H. J., Siebesma, A. P., and Van Meijgaard, E. (2015b). Weather forecasting using gpu-based large-eddy simulations. *Bull. Amer. Meteor. Soc.*, 96(5):715–723.

Schlemmer, L. and Hohenegger, C. (2015). Modifications of the atmospheric moisture field as a result of cold-pool dynamics. *Quart. J. R. Meteorol. Soc.*

Seifert, A. and Beheng, K. (2006). A two-moment cloud microphysics parameterization for mixed-phase clouds. part 1: Model description. *Meteorol. Atmos. Phys.*, 92(1-2):45–66.

Siebesma, A. P., Bretherton, C. S., Brown, A., Chlond, A., Cuxart, J., Duynkerke, P. G., Jiang, H., Khairoutdinov, M., Lewellen, D., Moeng, C.-H., et al. (2003). A large eddy simulation intercomparison study of shallow cumulus convection. *J. Atmos. Sci.*, 60(10):1201–1219.

Smagorinsky, J. (1963). General circulation experiments with the primitive equations. *Mon. Wea. Rev.*, 91(3):99–164.

Sommeria, G. (1976). Three-dimensional simulation of turbulent processes in an undisturbed trade wind boundary layer. *J. Atmos. Sci.*, 33(2):216–241.

Stevens, B. (2006). Bulk boundary-layer concepts for simplified models of tropical dynamics. *Theor. Comp. Fluid. Dyn.*, 20(5-6):279–304.

Stevens, B., Ackerman, A. S., Albrecht, B. A., Brown, A. R., Chlond, A., Cuxart, J., Duynkerke, P. G., Lewellen, D. C., Macvean, M. K., Neggers, R. A., et al. (2001). Simulations of trade wind cumuli under a strong inversion. *J. Atmos. Sci.*, 58(14):1870–1891.

Stevens, B. and Bony, S. (2013). What are climate models missing? *Science*, 340(6136):1053–1054.

Stevens, B. and Lenschow, D. H. (2001). Observations, experiments, and large eddy simulation. *Bull. Amer. Meteor. Soc.*, 82(2):283.

Stevens, B., Moeng, C.-H., Ackerman, A. S., Bretherton, C. S., Chlond, A., de Roode, S., Edwards, J., Golaz, J.-C., Jiang, H., Khairoutdinov, M., Kirkpatrick, M. P., Lewellen, D. C., Lock, A., MÃijller, F., Stevens, D. E., Whelan, E., and Zhu, P. (2005). Evaluation of large-eddy simulations via observations of nocturnal marine stratocumulus. *Mon. Wea. Rev.*, 133(6):1443–1462.

Stull, R. B. (1983a). A heat-flux history length scale for the nocturnal boundary layer. *Tellus A*, 35(3):219–230.

Stull, R. B. (1983b). Integral scales for the nocturnal boundary layer. part 1: Empirical depth relationships. *Journal of climate and applied meteorology*, 22(4):673–686.

Stull, R. B. (1988). *An introduction to boundary layer meteorology*. Kluwer Academic Publishers.

Stull, R. B. (2000). *Meteorology for scientists and engineers*. Brooks/Cole.

Sullivan, P. P. and Patton, E. G. (2011). The effect of mesh resolution on convective boundary layer statistics and structures generated by large-eddy simulation. *J. Atmos. Sci.*, 68(10):2395–2415.

Sullivan, P. P., Weil, J. C., Patton, E. G., Jonker, H. J., and Mironov, D. V. (2016). Turbulent winds and temperature fronts in large eddy simulations of the stable atmospheric boundary layer. *J. Atmos. Sci.*

van Heerwaarden, C. C. and Mellado, J. P. (early online release, 2016). Growth and decay of a convective boundary layer over a surface with a constant temperature. *J. Atmos. Sci.*

van Heerwaarden, C. C., Mellado, J. P., and De Lozar, A. (2014). Scaling laws for the heterogeneously heated free convective boundary layer. *J. Atmos. Sci.*, 71(11):3975–4000.

van Heerwaarden, C. C., van Stratum, B. J. H., Heus, T., Gibbs, J. A., and Fedorovich, E. (In preparation for Geosci. Model Dev., 2016). Microhh 1.0: a computational fluid dynamics code for direct and large-eddy simulation of atmospheric boundary layer flows.

van Stratum, B. J. H. and Stevens, B. (2015). The influence of misrepresenting the nocturnal boundary layer on idealized daytime convection in large-eddy simulation. *Adv. Model. Earth Syst.*, 7(2):423–436.

van Stratum, B. J. H., Vilà-Guerau de Arellano, J., van Heerwaarden, C. C., and Ouwersloot, H. G. (2014). Subcloud-layer feedbacks driven by the mass flux of shallow cumulus convection over land. *J. Atmos. Sci.*, 71(3):881–895.

Van Ulden, A. P. and Wieringa, J. (1996). Atmospheric boundary layer research at Cabauw. *Bound.-Layer Meteor.*, 78(1-2):39–69.

Vanzanten, M. C., Stevens, B., Nuijens, L., Siebesma, A. P., Ackerman, A., Burnet, F., Cheng, A., Couvreux, F., Jiang, H., Khairoutdinov, M., et al. (2011). Controls on precipitation and cloudiness in simulations of trade-wind cumulus as observed during rico. *Journal of Advances in Modeling Earth Systems*, 3(2).

Vilà-Guerau de Arellano, J. (2007). Role of nocturnal turbulence and advection in the formation of shallow cumulus over land. *Quart. J. R. Meteorol. Soc.*, 133(628):1615–1627.

Vogelezang, D. and Holtslag, A. (1996). Evaluation and model impacts of alternative boundary-layer height formulations. *Bound.-Layer Meteor.*, 81(3-4):245–269.

Wallace, J. M. and Hobbs, P. V. (2006). *Atmospheric science: an introductory survey*, volume 92. Academic press.

Wetzel, P. J., Argentini, S., and Boone, A. (1996). Role of land surface in controlling daytime cloud amount: Two case studies in the gcip-sw area. *J. Geophys. Res.*, 101(D3):7359–7370.

Wicker, L. J. and Skamarock, W. C. (2002). Time-splitting methods for elastic models using forward time schemes. *Mon. Wea. Rev.*, 130(8):2088–2097.

Williamson, J. H. (1980). Low-storage Runge-Kutta schemes. *J. Comput. Phys.*, 35:48–56.

Wilson, D. K. (2001). An alternative function for the wind and temperature gradients in unstable surface layers. *Bound.-Layer Meteor.*, 99(1):151–158.

Wyngaard, J. C. (2004). Toward Numerical Modeling in the ”Terra Incognita”. *J. Atmos. Sci.*, 3(2):1816–1826.

Wyngaard, J. C. (2010). *Turbulence in the atmosphere.* Cambridge University Press, New York.

Yin, J., Albertson, J. D., Rigby, J. R., and Porporato, A. (2015). Land and atmospheric controls on initiation and intensity of moist convection: Cape dynamics and lcl crossings. *Mon. Wea. Rev.*, 51(10):8476–8493.

Zhou, B., Simon, J. S., and Chow, F. K. (2014). The convective boundary layer in the Terra Incognita. *J. Atmos. Sci.*, 71(7):2545–2563.

Zilitinkevich, S. and Mironov, D. V. (1996). A multi-limit formulation for the equilibrium depth of a stably stratified boundary layer. *Bound.-Layer Meteor.*, 81(3-4):325–351.

# List of reviewed publications

+ = Part of this thesis, - = not part of this thesis

+ **B.J.H. van Stratum**, B. Stevens (2015): The influence of misrepresenting the nocturnal boundary layer on idealized daytime convection in large-eddy simulation. J. Adv. Model. Earth Syst., 07 (10.1002/2014MS000370)

- J. Vila-Guerau de Arellano, C.C. van Heerwaarden, **B.J.H. van Stratum**, K. van den Dries (2015): Atmospheric Boundary Layer: Integrating Chemistry and Land Interactions. Cambridge Univ. Press, ISBN 9781107090941
- **B.J.H. van Stratum**, J. Vila-Guerau de Arellano, C.C. van Heerwaarden, H.G. Ouwersloot (2014): Sub-cloud layer feedbacks driven by the mass-flux of shallow cumulus convection over land. J. Atmos. Sci. 71, 881-895 (10.1175/JAS-D-13-0192.1)
- H.G. Ouwersloot, J. Vila-Guerau de Arellano, **B.J.H. van Stratum**, M.C. Krol and J. Lelieveld (2013): Quantifying the transport of sub-cloud layer reactants by shallow cumulus clouds over amazonia. J. Geophys. Res-Atmos. 118, 13,041-13,059 (10.1002/2013JD020431)
- **B.J.H. van Stratum**, J. Vila-Guerau de Arellano et al. (2012): Case study of the diurnal variability of chemically active species with respect to boundary layer dynamics during DOMINO. Atmos. Chem. Phys., 12 (12), 5329-5341 (10.5194/acp-12-5329-2012)

# List of Figures

# List of Tables

# Acknowledgements

First I would like to thank Bjorn, both for creating the possibility to do my PhD in Hamburg, and for supervising my research. It is inspiring to see that you manage to run our institute (and so many other initiatives), and still find the time and inspiration to supervise a group of PhD students! In addition, I would like to thank Stephan and Marco for serving in my PhD panel. Your comments (*"write, write, write"*) were often much needed. And equally important, I would like to thank Antje, Cornelia and Wiebke for all the support from IMPRS.

Outside my PhD I would like to thank a number of people, related to two projects that I greatly enjoyed working on over the past few years. Jordi, Chiel and Kees; it has been a long journey with CLASS, but I'm really happy that the book and software became such a success! And Chiel; thanks for all the fun times working on MicroHH. Although it started (at least for me) as a hobby project, I feel that I have learned a lot about coding (in a modern programming language ;-)) and numerical modeling from you.

On a personal note: Antonija, Mirjana, Jessica, Josianne, Vladimir, Chiel, and so many other people: thanks for all the fun times in Hamburg!

Above all, I would like to thank my parents, Jac. and Anne-Marie, for all the support during my study. It's been a long road from high school to finishing this dissertation, and without the support and freedom that you have always given me, and your trust in my (sometimes slightly wild) study choices, this thesis surely wouldn't have been here.

This PhD was funded by the Federal Ministry of Education and Research in Germany (BMBF) through the research program *High Definition Clouds and Precipitation for Climate Prediction* - HD(CP)2 (FKZ: 01LK1202E). Computing resources were provided by the German Climate Computing Center (DKRZ), Hamburg. I thank the University of Hamburg, the Institute for Meteorology and Climate research – Karlsruhe Institute of Technology (KIT), and the Cabauw Experimental Site for Atmospheric Research (CESAR) for providing the measurement data used in this thesis, Rieke Heinze and Chiel van Heerwaarden for feedback on Chapters 3 and 5, respectively, and Ann Kristin Naumann for help with the translation of the abstract of this thesis.